THEORETICAL-EXPERIMENTAL MOLECULAR ENGINEERING TO DEVELOP NANODEVICES FOR SENSING SCIENCE

A Dissertation

by

NORMA LUCIA RANGEL

Submitted to the Office of Graduate Studies of
Texas A&M University
in partial fulfillment of the requirements for the degree of

DOCTOR OF PHILOSOPHY

May 2011

Major Subject: Materials Science and Engineering

Theoretical-Experimental Molecular Engineering to Develop Nanodevices for Sensing Science

THEORETICAL-EXPERIMENTAL MOLECULAR ENGINEERING TO DEVELOP NANODEVICES FOR SENSING SCIENCE

A Dissertation

by

NORMA LUCIA RANGEL

Submitted to the Office of Graduate Studies of
Texas A&M University
in partial fulfillment of the requirements for the degree of

DOCTOR OF PHILOSOPHY

Approved by:

Chair of Committee,	Jorge M. Seminario
Committee Members,	Zhengdong Cheng
	Yue Kuo
	Hong Liang
	Victor Ugaz
Interdisciplinary Faculty Chair,	Ibrahim Karaman

May 2011

Major Subject: Materials Science and Engineering

ABSTRACT

Theoretical-Experimental Molecular Engineering to Develop Nanodevices
for Sensing Science. (May 2011)
Norma Lucia Rangel, B.Sc., Universidad Industrial de Santander
Chair of Advisory Committee: Dr. Jorge M. Seminario

Molecular electrostatic potentials (MEPs) and vibrational electronics ("vibronics") have developed into novel scenarios proposed by our group to process information at the molecular level. They along with the traditional current-voltage scenario can be used to design and develop molecular devices for the next generation electronics. Control and communication features of these scenarios strongly help in the production of "smart" devices able to take decisions and act autonomously in aggressive environments. In sensor science, the ultimate detector of an agent molecule is another molecule that can respond quickly and selectively among several agents. The purpose of this project is the design and development of molecular sensors based on the MEPs and vibronics scenarios to feature two different and distinguishable states of conductance, including a nano-micro interface to address and interconnect the output from the molecular world to standard micro-technologies.

In this dissertation, theoretical calculations of the electrical properties such as the electron transport on molecular junctions are performed for the components of the sensor system. Proofs of concept experiments complement our analysis, which includes an electrical characterization of the devices and measurement of conductance states that may be useful for the sensing mechanism. In order to focus this work within the very broad array between nanoelectronic and molecular electronics, we define the new field of Molecular Engineering, which will have the mission to design molecular and atomistic devices and set them into useful systems. Our molecular engineering approach begins with a search for an optimum fit material to achieve the proposed goals; our published results suggest graphene as the best material to read signals from molecules,

amplify the communication between molecular scenarios, and develop sensors of molecular agents with high sensitivity and selectivity. Specifically, this is possible in the case of sensors, thanks to the graphene atomic cross section (morphology), plasmonic surface (delocalized charge) and exceptional mechanical and electrical properties.

Deliverables from this work are molecular devices and amplifiers able to read information encoded and processed at the molecular level and to amplify those signals to levels compatible with standard microelectronics. This design of molecular devices is a primordial step in the development of devices at the nanometer scale, which promises the next generation of sensors of chemical and biological agents molecularly sensitive, selective and intelligent.

DEDICATION

A Carlos, mi esposo, este logro lo comparto contigo, y dedicártelo es poco para agradecerte por todo tu amor y comprensión, por haberme dado mi mejor y más hermoso regalo, nuestra hija Olivia, que le ha dado significado y valor a todo, cuya sonrisa me enseñó que nada es imposible si lo hago por ella, a ti Olivia dedico no solo este trabajo sino mi vida entera, gracias por darme este privilegio de ser tu mamá, por hacerme sentir este tipo de amor, ternura y fortaleza para darlo todo por hacerte feliz…

Mis babies, mi familia, mis amores… los amo con todo mi corazón.

Translation

To my husband, Carlos, I share this achievement with you, and dedicating it to you is not enough to thank you for all your love and understanding, for giving me my best and most beautiful gift, our daughter Olivia, who has given meaning and value to all of this, whose smile taught me that nothing is impossible if I do it for her. To you, Olivia, I dedicate not only this work but my entire life, thank you for giving me this privilege of being your mom, for making me feel this kind of love, tenderness and strength to give everything to make you happy…

My babies, my family, my loved ones… I love you with all my heart.

ACKNOWLEDGEMENTS

I would like to thank my committee members, Dr. Balbuena, Dr. Cheng, Dr. Kuo, Dr. Liang and Dr. Ugaz, for their guidance and support throughout the course of this research, and for their time and effort in being members of my committee.

I thank Dr. Seminario, who has been a great support for me during all these years. I would like him to know that the time that I have been under his direction has been very special. I admire him; his devotedness and dedication to his work have been a great example and have served as motivation for me. Thank you for nourishing my creativity, for patiently teaching me how to be a researcher, to seek excellence, to be productive and systematic. I hope to apply your teachings throughout my career and life.

Thanks also go to my friends and colleagues of the Molecular Engineering group, smart, great and valuable people. I also want to extend my gratitude to the agencies supporting this research, the U.S. Army Research Office and the U.S. Defense Threat Reduction Agency (DTRA).

Thanks to the Materials Science and Engineering Program Coordinator, Jan Gerston, for all the help and support during these years, to faculty and to the Chemical Engineering Department faculty and staff for making my time at Texas A&M University a great experience.

Thank you to my husband, Carlos, who has been with me these past years. With tolerance and love he has accompanied me through moments of happiness and sadness. He has given me a wonderful family and has filled all my empty spaces. Thank you for being my other half, my support, my partner, my hand-break and my problem to each solution.

To my family that I miss so much, and that does not forget me despite the distance, sensible and lovely fathers and mothers; from each one of you I carry something special in me, that has made me the person I am and for which I am grateful every day. I thank my mom for all her love and advices, for listening, tolerating, and

taking care of me and for so long. I thank my mommy, for being my best friend, my confident and an unconditional love, an excellent role model of a serene, intelligent woman, capable of achieving everything she tries. Thank you to the dynamic duo, my uncle and my dad, unconditional brothers that have been my favorites despite all the tumbles along the way.

I thank my acquired family, which I choose so well, I want you to know that not only blood creates bonds. I will give it all to be a good daughter-in-law, wife and Olivia's mother. You have my heart even though sometimes you want to give it back. I particularly want to thank Mrs. Doris, you are an excellent woman and mother, I admire your devotion and dedication to your sons and granddaughters, there is no recognition that could match all the work you have done; without your help this dissertation would not have been written, and without your company this time in Texas would have been difficult. Thank you for everything you have done for us.

Thank you Roberto, the brother I never wanted, my gordis that has helped me so much, and who I have always been able to rely on. Thank you to my College Station friends who have been a great support and a company of nerds during all these years, turning into a great big family.

Thank you my guardian angel, who watches over me throughout the night and the day.

NOMENCLATURE

AFM	Atomic Force Microscopy
AuNPs	Gold NanoParticles
CNT	Carbon Nanotubes
DFT	Density Functional Theory
DFT-GF	Combined DFT and GF
DOS	Density of States
GF	Green Function Theory
GNR	Graphene Nano-Ribbon
HLG	HOMO-LUMO Gap
HOMO	Highest Occupied Molecular Orbital
I-V	Current-Voltage
LUMO	Lowest Unoccupied Molecular Orbital
MEP	Molecular Electrostatic Potential
MO	Molecular Orbital
OPE	Oligo Phenylene-Ethynylene
OPE-AZA	pyridazine, 3,6-bis(phenylethynyl)
SEM	Scanning Electron Microscopy
STM	Scanning Tunneling Microscope
TEM	Transmission Electron Microscopy
Vibronics	Vibrational Electronics

TABLE OF CONTENTS

Page

Page

Page

LIST OF FIGURES

Page

Page

Page

Page

Page

Page

Page

Page

Page

Page

LIST OF TABLES

Page

Page

CHAPTER I
INTRODUCTION

1.1 Importance and Goals of This Research

Molecular electrostatic potentials (MEPs) and vibrational electronics ("vibronics") are novel scenarios to process information at the molecular level that along with the traditional current-voltage scenario can be used to design and develop molecular devices and systems.

Successful control and communication features between scenarios would yield to "smart" devices able to take decisions and act under certain difficult conditions. However, molecular potentials are still unreadable and non-approachable by any present technology. It is known that the proper assembly of molecules can result in a numerical processing system based on digital or even analogical computation. Thus, the outputs of molecular processing units need to be read and amplified in order to be interfaced through standard electronics and useful for nanotechnology.

On the other hand, the size of the device is of important consideration, for example, in sensor science, the ultimate detector of a molecule is another molecule that can respond quickly and selectively to several agents; therefore, a nano-micro interface is needed to interconnect the output from a molecular device to standard technologies.

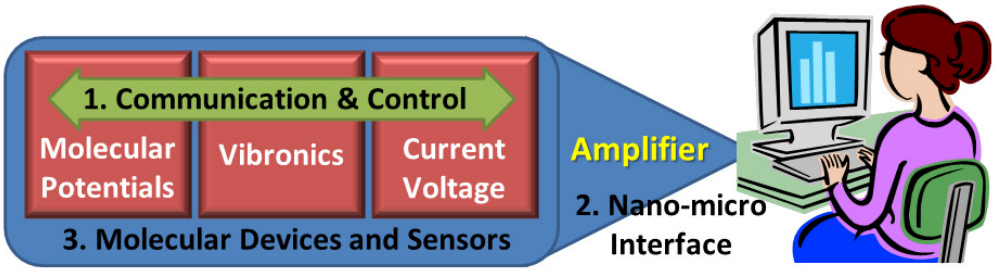

Fig. 1. Three major goals of this research.

This dissertation follows the style of *Science*.

In summary, this research is a molecular engineering project that comprises three major goals (Fig. 1): first, an understanding of how the three molecular scenarios for processing information, MEPs, vibronics and current-voltage can be implemented to operate, control and communicate in the device, in such a way that allows the development of smart devices; the second goal is to design and develop a nano-micro interface able to read and amplify information and signals encoded and processed at the molecular level to current technologies. Thus, this interface amplifies signals from nanoscale devices to levels compatible with standard microelectronics. Finally, as a direct result of this project, an outcome of devices and sensors is expected with high selectivity and sensitivity that will contribute to the scaling down and performance in nanotechnology and improvements in conventional engineering applications.

1.2 Background and Significance

1.2.1 Vibronics

When a signal is injected into a molecule, the vibrational mode of the atoms around the injection point changes affecting the atoms in the molecule that are bonded to each other; frequency changes in vibrational states of the molecule trigger different movement of atoms, whose frequencies are transferred to their neighbor atoms by means of bond bendings, bond stretchings, Van der Waals and coulombic interactions between charges, etc. (*1*). Thus, using vibronics, the signals are transferred through molecules (*2, 3*). When an atom in a molecule is displaced, a displacement signal is transmitted through the molecule by the vibrational modes. This is similar to the case of a mass-and-spring system, where a displacement from equilibrium experiences a proportional restoring force. This effect also occurs when an external stimulus is applied by another molecular vibration or potential in the neighborhood. Furthermore, an atom displacement introduces a change in the distribution of the molecular electrostatic potential.

1.2.2 Molecular Electrostatic Potentials

Molecular potentials offer the opportunity to use the art and science of chemistry to build molecules as electronic devices. As it stands, until a new technique to fabricate molecular circuits and transmit information between molecules is discovered, perhaps there is no other alternative than using the molecular potentials for the encoding and processing of information in of molecular electronic systems. Currently, we must rely on molecular potentials to develop systems that can continue the tremendous scaling down of photolithography in the massive fabrication and wiring of silicon based circuits.

It has been demonstrated using reliable *ab initio* techniques that information can be encoded using molecular electrostatic potentials (MEP) (*4-12*). This represents a new alternative to the standard charge-current approach used in standard electronics. Few molecules were found to function as molecular OR- (*13*) and AND logical gates (*3*). Present computers perform calculations reducing the information to binary notation whereby the only two binary digits (bits) are 1 and 0, which can be also assigned to pairs of logical variables or states such as TRUE or FALSE, ON or OFF, HIGH or LOW, POSITIVE or NEGATIVE, respectively. In binary notation the number nine is written as 1001, requiring at least four binary digits (bits). Operations between binary variables are performed using logical gates such as the NOT, AND, OR, etc. For instance the simplest one is the NOT which outputs a 0 if the input is 1 and yields 1 if the input is 0. The AND gate has two or more inputs and the output is 1 if all inputs are 1 and 0 is any input is 0. The OR gate yield a 0 when all inputs are zero and 1 when any input is 1. Interestingly, these gates can be combined to make adders, multipliers, integrators, etc. In principle we can do numerically any operation that we can imagine. Recently, it has also been demonstrated that the output of two molecular OR-gates can be used as the input of a third molecular OR-gate, thus opening the possibility to implement complex molecular electrostatic potential circuits using simpler molecular logic gates. All these earlier calculations were performed with the molecular gate at vacuum and triggered by the electrostatic potential of small molecules as inputs to the gate. We showed how the substrate affects the molecular electrostatic potential device. We tested substrates on a

molecule, which had been demonstrated to be an OR-gate in vacuum (*3*). The effect of the substrate on the molecular devices is of paramount importance for the theoretical proof-of-concept of this new scenario for molecular computing.

1.2.3 Molecular Orbital Theory

Short highest occupied molecular orbital (HOMO)-lowest unoccupied molecular orbital (LUMO) gaps (HLG) (i.e., low hardness, high softness) are indicative of poor stability of the wavefunction, which worsens in stability as an external field is applied to the molecule. The localization of molecular orbitals (MOs) and the enlargement of HOMO-LUMO gaps suggest poor conduction in determined transport paths (*14, 15*).

1.3 Sensor Devices

A sensor device is a transducer of a physical or chemical quantity into an electrical or optical signal. Sensors of physical parameters such as temperature, pressure, magnetic fields, forces, etc. can be encapsulated to avoid the effects of the environment; however, parameters of chemical sensors are concentration of substances which can be several in a single sample (e.g. air, blood), thus the sensitivity of the sensor is a challenge along with the durability due to interfering substances and environmental effects of factors such as light, corrosion and reactivity. Therefore, sensing science is a multidisciplinary field that pursuits the development of new devices with high selectivity and sensitivity, enabling rapid analysis, durability and reduced costs.

There are several types of chemical sensors: conductive type sensors are based on measurements of material resistivity. They are used usually employed to sense gases but with poor selectivity due to the reactivity of the materials with the environment. Electrochemical sensors are used for pH measurements and gas detection, but there are limitations in fabrication, costs and usability time of the device due to the consumption of the electrodes; they can be fabricated in batches and allows the scaling down of sensor devices; however, for the conductivity sensors, electrochemical sensors are not suitable

for aggressive environments. High sensitivity sensors has been developed using mass sensitive devices such as nano-electromechanical and resonator devices. For harsh environments absorption and emission of electromagnetic radiation has been used in optical sensors, among them, fiber optic, photo-acoustic sensors, luminescence, etc. Also, calorimetric sensors have been used to detect exothermic biochemical reactions based on the thermal energy released.

Graphene has been demonstrated to act as a resonator, transducer, signal mixer and high sensitivity and selectivity sensors, thanks to the exceptional intrinsic electrical, mechanical and thermal properties for applications in sensing science as an optimum material for each different type of sensor; the convenient fabrication of the devices, and atomic cross section allow graphene to be the perfect material for measurement of chemical and physical parameters.

1.4 Summary and Outline of This Research

This research project is a combination of proof of concept experiments and molecular analysis and simulations to design and develop molecular sensors of chemical and biological agents. The aim is to design sensors of chemical agents with high sensitivity and selectivity, based on novel molecular scenarios such as vibronics and molecular electrostatic potentials. Detected signals from the agent molecule are amplified using the conventional current-voltage characteristics of the sensor material, whereby different states of conductance, theoretically calculated or experimentally measured, are used as sensing mechanism.

In Chapter II we begin defining the molecular engineering approach, with a brief description of the overall theory and experiments carried out in this dissertation. A summary of the molecular orbital theory, quantum-mechanical methods and formalisms for the calculation of single molecule conductance are shown. Proof of concept experiments in this research project consist of chip fabrication, assembly of the sensor material on the chip, morphological characterization of the device and testing of the

sensing performance through current-voltage characteristics; each step, along with the tools and methodologies are shown in the second section.

In Chapter III, the search for an optimum fit material to achieve our goals begins with the attempt to use long biomolecules such as DNA chains and DNA origami as sensors. Our published work on the electronic characterization is shown. However, the high impedance and reactivity of the DNA samples found, along with the challenging reproductively fabrication of the devices moved our interest to graphene, whose properties, fabrication methods and applications are deeply discussed in Chapter IV and whereby its implementation as sensor material and focus of our study is shown through the dissertation.

Chapter V starts with and study of the substrate effect on a MEP-based molecular OR-gate as a design variable, then the amplification of the output signals is shown using an aza-OPE molecule and graphene ribbons through changes in its current-voltage characteristics, which is one of the proposed goals of this research along with the communication between scenarios that is covered on Chapter VI using graphene ribbons. The effect of the molecular vibrations on the electrostatic potential spatial distribution is amplified through current voltage characteristics transversally calculated using graphene electrodes.

Application examples of the theory-experiment molecular engineering approach are shown in Chapter VII where the molecular engineering approach is applied to study molecular devices theoretically and experimentally. Based on our published work, switches as application examples are shown, first, a light activated molecular switch device based on vitamin D_3 and second, the chapter closes with the switchability of a gold nanoparticle film activated by an external mechanical force and conformational changes of the linker citrate molecules.

In Chapter VIII, developed graphene sensors using vibronics and plasmonic scenarios are described. The changes in conductance of the graphene ribbons are explored when chemical agents are adsorbed on the plasmonic surface of graphene; we

base our analysis and results based on molecular orbitals and calculations of the junction conductance.

In Chapter IX a nonlinear behavior of the conductivity transversally calculated for few graphene layers is found and allows the detection of variable frequency signals and applications for novel highly sensitive sensor devices of terahertz fingerprints of molecular agents.

Finally, in Chapter X, we state our conclusions and provide suggestions for future work.

CHAPTER II

MOLECULAR ENGINEERING - A THEORY/EXPERIMENT APPROACH

The proposed research methodology is a combination of proof of concept experiments and molecular modeling to perform "molecular engineering" as is shown in Fig. 2; the novel molecular potentials and vibronics as well as the common current-voltage scenarios are used to design and develop nanodevices able to sense chemical and biological agents and perform logic operations.

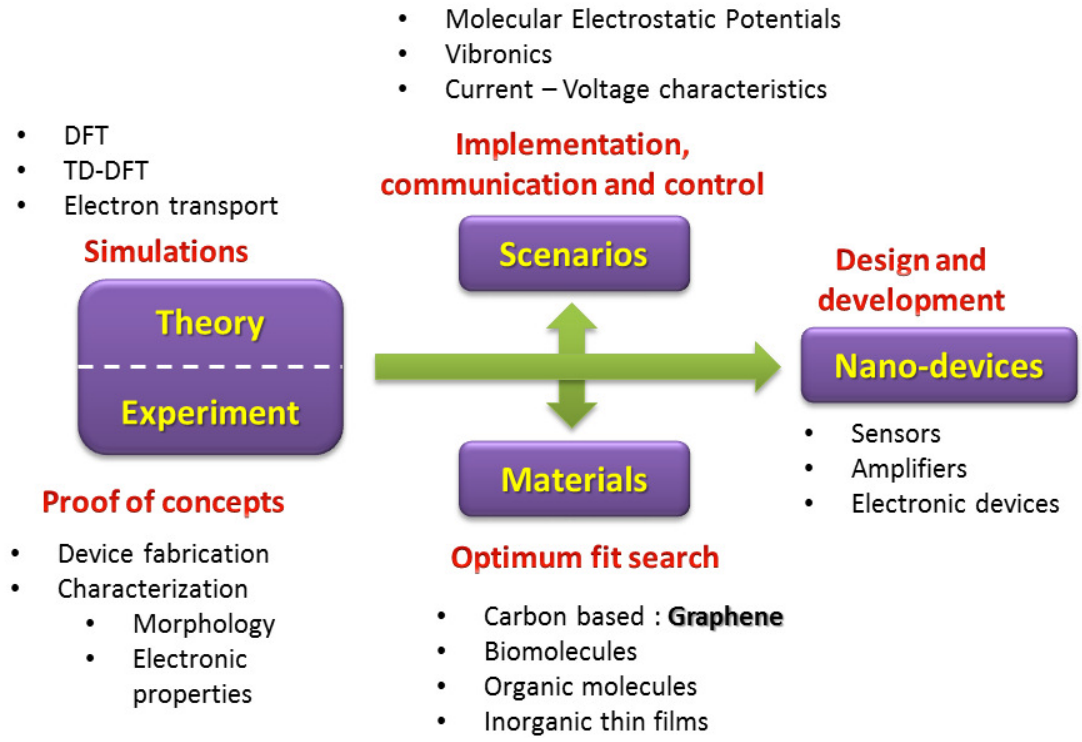

Fig. 2. Molecular engineering approach and research plan to design and develop nanodevices for sensing science. Using molecular modeling and proof of concept experiments the design and development of devices operated by molecular scenarios and engineered materials that allow interfaces from nano to macro technologies at the molecular level. Developed devices are used and implemented to improve nanotechnology and conventional engineering applications.

One of the project requirements is to study materials and molecules constituting a sensor system and to find and suggest the best fitted material for convenience,

sensitivity, selectivity and efficiency to be used as detectors or base material in the device.

Integration of novel and traditional scenarios to develop nano-devices allows an upgrade of conventional engineering applications with modern nanotechnologies such as molecular-electronics, which can be applied to develop devices for the post CMOS era, solar cells, catalysis, sensing, chemical and biological defense and security, biotechnology, medicine and photo-electronics. A scheme of the research plan and design to achieve the proposed goals is shown in Fig. 2.

In this chapter, a description of the theory and experimental approach used this dissertation is described. First, quantum mechanics methods and the formalism of the theoretical calculation of electrical properties for finite and infinite systems; level of theory implemented such as methods and basis sets; and single molecule conductance of molecular junctions is described; followed by the overall experimental approach, which includes a description of the techniques to fabricate electrodes of the sensor, the assembly of the sensor material on the device, morphology of the devices by microscopy techniques and finally a description of the electrical characterization of the fabricated devices.

2.1 Theoretical Calculations

Two types of molecular systems are used in this dissertation: single molecules with a finite number of atoms and junctions combining finite systems (molecules) absorbed on metallic contact tip (bulk).

Electronic properties of finite systems are obtained using quantum chemistry by solving the Schrödinger equation, applying appropriate correlation and approximations factors as is done for example using density functional theory (DFT). Combined Green function theory (GF) and DFT are used to calculate the conductance of electrode-molecule-electrode junctions.

2.1.1 *Ab initio* Molecular Orbital Theory

The energy and electrical properties of a molecule can be predicted by solving the Schrodinger equation

$$\mathrm{H}\,\Psi = E\,\Psi \tag{1}$$

which describes the wavefunction Ψ of the particles in the system, and where E is the energy of the molecule and H is the Hamiltonian operator.

The full Hamiltonian is made up of kinetic (T) and potential (V) energy terms and can be written as:

$$\mathbf{H} = \boldsymbol{T} + \boldsymbol{V} = \boldsymbol{T^e}(\vec{\boldsymbol{r}}) + \boldsymbol{T^n}\left(\vec{\boldsymbol{R}}\right) + \boldsymbol{V^{n-e}}\left(\vec{\boldsymbol{R}}, \vec{\boldsymbol{r}}\right) + \boldsymbol{V^e}(\vec{\boldsymbol{r}}) + \boldsymbol{V^n}\left(\vec{\boldsymbol{R}}\right) \tag{2}$$

The nuclear kinetic energy term in Eq. 2 can be neglected using the Born-Oppenheimer approximation which considers that the mass of the nuclei is greater than the electron mass and thus moves very slowly with respect to the electrons.

Using proper boundary conditions and approximations; each possible solution of the time-independent Schrodinger equation correspond to a different stationary state of the system, the one with the lowest energy is considered the ground state.

The spatial wavefunction is independent of time and function of the positions of the electrons ($\vec{\boldsymbol{r}}_i$) and the nuclei ($\overrightarrow{\boldsymbol{R_I}}$), should be normalized and anti-symmetric. To calculate the electronic properties of a system the wavefunction is a determinant of molecular orbitals (MOs) and spin functions "spin orbital". MOs can be expressed as linear combinations of the atomic orbitals that are one-electron functions known as basis functions χ.

2.1.2 Basis Sets

In this work, Gaussian functions are used to form a complete set of functions, and have the general Cartesian form as:

$$g(\alpha, \vec{\boldsymbol{r}}) = cx^n y^m z^l e^{-\alpha r^2} \quad (3)$$

where n, m and l are nonnegative integers, α is a positive orbital exponent, c is a normalization constant, r is the radial coordinate and x, y and z are the cartessian coordinates which origin is at the nucleus. Linear combinations of these primitive gaussians are used for the calculations and are called contracted Gaussian functions with the form:

$$\chi_\mu = \sum_p d_{\mu p} g_p \quad (4)$$

where $d_{\mu p}$ are fixed constants within a given basis set.

The Gaussian basis functions usually include additional primitives to include polarization and diffusion functions.

In this dissertation basis sets such as the 3-21G (*16*), 6-31G(d) (*17*) (*18*), 6-31G(d,p) (*17, 18*) and cc-pVTZ (*19*) are used for first and second (and some third) row atoms, when heavier atoms are part of the calculation, Los Alamos National Laboratory (LANL2DZ) basis set (*20, 21*) is used.

2.1.3 Hartree Fock

Hartree Fock theory searches for a local minimum, by finding the set of coefficients that minimize the energy of the wavefunction.

The Fock matrix represents the average effects of the field of all the electrons in each orbital and as the orbitals depend on the molecular orbital expansion coefficients, thus the self-consistent method (SCF) is used. At convergence the energy is at a minimum and the orbitals generate a field which produces the same orbitals.

However, Hartree Fock method does an inadequate treatment of the correlation effects due to motion of electrons; causing large errors.

In this work, geometry optimizations are systematically carried out from the less expensive *ab initio* methods such as Hartree-Fock (HF), to density functional theory

(DFT) (*22*) methods, which include electron correlation in a very efficient way. Second derivatives of the energy yielding the Hessian are also needed to obtain molecular vibrations.

2.1.4 Density Functional Theory

Calculations of the wavefunction are computationally expensive and only feasible for small systems. Density functional theory allows the introduction of the electron correlation and the study of larger systems. DFT is based on the first Hohenberg-Kohn (1964), which establishes that properties in the ground state are functionals of the electron density.

In 1965 Kohn-Sham demonstrated that the electron density of a molecular system of interacting electrons can be represented with the electron density of an equivalent system of non-interactive electrons subjected to an effective potential.

2.1.5 Hybrid Methods

The DFT B3PW91 hybrid functional includes a combination of the Perdew-Wang-91 (*23, 24*) and has shown good energetics predictions (*25, 26*) but the M05-2X meta functional has a larger range electron correlation that improves the performance for nonbonded interactions and π-π stacking (*27*), showing good binding energies and geometry optimizations of molecules non-covalently bonded and stacking order, therefore, M05-2X is used for non-bonded interactions and B3PW91 for bonded systems and total energies.

2.1.6 Molecular Electrostatic Potentials Calculations

Molecular potentials are calculated from the nuclei and electron density contributions. The electron density ρ(r) is obtained by adding the density of each occupied molecular orbital and is defined as:

$$\rho(\vec{r}_1) = N\int \psi^*(\vec{r}_1,\vec{r}_2,\cdots\vec{r}_N)\psi(\vec{r}_1,\vec{r}_2,\cdots\vec{r}_N)d\tau_2\cdots d\tau_N \tag{5}$$

where $\psi(\vec{r}_1,\vec{r}_2,\cdots\vec{r}_N)$ and $\psi^*(\vec{r}_1,\vec{r}_2,\cdots\vec{r}_N)$ are the wavefunction and its complex conjugate and *N* is the total number of electrons.

Equation 5 reduces to:

$$\rho(\vec{r}) = \sum_1^N \left|\phi_i(r)\right|^2 \tag{6}$$

The MEP, $V(\vec{r})$, is calculated from the nuclei and electron density contributions (*28*),

$$V(\vec{r}) = \sum_i \frac{Z_i e}{|\vec{R}_i - \vec{r}|} - \int \frac{\rho(\vec{r}')}{|\vec{r} - \vec{r}'|} d\tau' \tag{7}$$

where Z_i is atomic number of atom *i* located at $\vec{R}_i$.

In this work, all finite system calculations are performed using the program GAUSSIAN-09 and earlier versions.

2.1.7 Single Molecule Conductance

Extensive theoretical and experimental effort has been invested in the understanding of electron transfer mechanisms in single organic molecules due to their potential applications in nano-scale electronic systems (*15*). It has been found that the current running through the molecule is the sum of the contributions from all molecular orbitals each presenting a barrier to electron transport equal to their energy difference from the Fermi level of the contacts. Since a molecule is the fundamental component of a programmable molecular array, the electrical characteristics of the molecule, especially the current-voltage characteristic, are the major design parameters for the programmable molecular array (*29*).

The continuous electronic states of macroscopic contacts affect the discrete electronic states of isolated molecules calculated by solving the Schrödinger equation, thus, a combination of Density Functional Theory and Green function theory (DFT-GF) is used to obtain the electrical properties of the metal-molecule-metal junction.

After a geometry optimization of the extended molecule using quantum chemistry techniques to determine the electronic properties of the extended molecule, a bias voltage is applied to the molecule. During the field calculation, the geometry of the molecule is kept the same as the one without field.

The partial density of state (DOS) is calculated using Crystal 06 for the electrodes, and the sets for each bias voltage of the Hamiltonian and overlap matrices obtained using Gaussian 09 are entered in our in situ developed program, GENIP which executes the combined DFT-GF formalism to obtain the current-voltage characteristics of the junction by considering the local nature of the molecule as well as the non-local features of the contacts.

2.2 Experimental Set Up

The development of nano-devices proposed in this project includes several fabrication techniques depending on the necessity, dimensions, and purpose of the

device. Once the chip is fabricated with an appropriate morphology, the sensor material is assembled and the sensor performance is studied by an electrical characterization, as is described in the following sections:

2.2.1 Device Fabrication

A general description of the fabrication techniques and characterization is summarized in this section, however further details are provided as corresponds or needed in each chapter.

2.2.1.1 Chip fabrication

Nanolithography techniques including photolithography and electron beam lithography have been used to fabricate the chips. Basically, the chips structure consists of pairs of metal electrodes on insulator substrates and small gaps between them where the sensor material is assembled allowing isolation to perform the electrical measurements of the studied material.

2.2.1.2 Assembly of sensor material

Similarly, depending on the material used or studied between the electrodes, a different technique in each case is used and optimized upon success. Thus far, cleavage of graphene layers using the "scotch tape" technique, dielectrophoresis of DNA molecules and self-assembled monolayers of organic molecules are some of the procedures carried out in the fabricated devices. More details about assembly procedures will be described in each section as corresponds.

2.2.2 Device Characterization

2.2.2.1 Morphology

The fabricated devices are characterized morphologically before and after the assembly of the sensor material. Tool for morphology characterization include optical microscopes, scanning electron microscopy (SEM, JSM-6400, JEOL) and a Nanoscope IIIa-Multimode atomic force microscope (*30*) from Digital Instruments. AFM

topographic images are obtained using a close contact mode with standard silicon nitride cantilevers (Nano World).

2.2.2.2 Electrical characterization

An electronic characterization of the devices is usually performed using a probe station (Lakeshore Cryogenic probe station) (*31*) shown in Fig. 3. In order to exclude environmental influence, the sample is placed inside a high vacuum (about 10^{-7} torr) chamber during measurements. Temperature is kept constant and may be controllably varied using liquid nitrogen and a sensor attached to the sample holder.

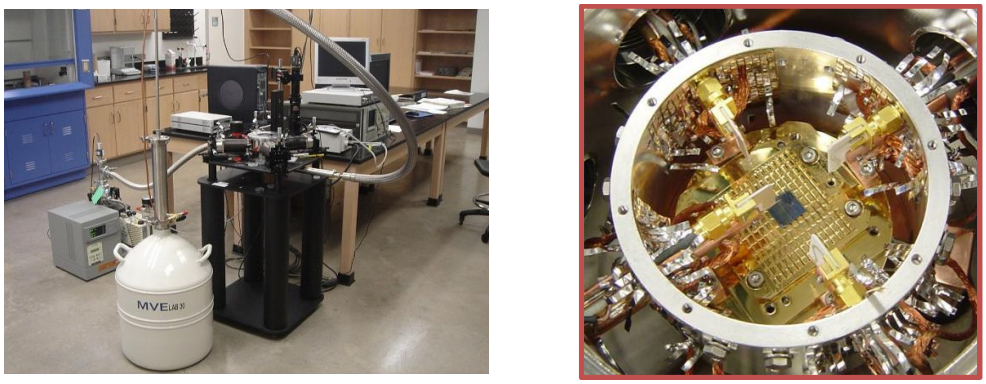

(A) (B)

Fig. 3. (A) Molecular engineering lab. Probe station, pump, semiconductor analyzer and liquid nitrogen Dewar flask. (B) Four probes, 3 µm diameters.

In order to measure the electrical characteristics, a HP4145A semiconductor parameter analyzer (*32*) to control the applied voltage for I-Vs. The oscilloscope (TDS 5104) (*33*) and function generator (AFG 3252) (*34*) are used to measure the impedance of molecules, and to introduce AC signals of frequencies up to 5 MHz to the fabricated devices.

CHAPTER III
OPTIMUM FIT MATERIAL FOR NANO-MICRO INTERFACE – DNA*

A materials study is required in this project to find the best fit material to achieve our main goal of amplification of signals from molecules, and the development of sensors. High sensitivity and selectivity of the chosen material is needed and appropriate lengths (nano-micro sizes) to achieve molecular sensitivity and facilitate the assembly on micro-sized chip gaps. Therefore, a screen of materials has been performed in this dissertation and is described through each chapter. Materials considered include large chain molecules such as DNA (*35*), DNA origami (*36, 37*) and alpha glycine (*38*); carbon based materials such as carbon nanotubes (*39*) and graphene (*40-42*); organic molecules such as the 4,4'-(diethynylphenyl)-2'-nitro-1-benzenethiolate (*43*), octyltrichlorosilane , and the 7-dehydrocholesterol (precursor of vitamin D_3) (*44*); and thin films of metal nanoparticles (*45*). Special emphasis is made on graphene in this dissertation due to its exceptional performance and capabilities to achieve the proposed goals, consequently is the focus and main material for the developed sensors of this research. This chapter covers the study and electrical characterization of DNA chains and origami DNA.

3.1 DNA

There has been considerable interest in developing electrical circuits with DNA (*46, 47*). DNA electronics take advantage of the tunneling and quantized capacitance in

---

* Parts of this chapter are reprinted with permission from:
- Impedance measurements on a DNA junction, by S. Hong, L. A. Jauregui, N. L. Rangel, H. Cao, S. Day, M. L. Norton, A. S. Sinitskii, and J. M. Seminario, 2008. *J. Chem. Phys*., **128**, 201103. Copyright 2008 by the American Institute of Physics.
- DNA origami impedance measurement at room temperature; by A. D Bobadilla, E. P Bellido, N. L Rangel, H. Zhong, M. Norton, A. Sinitskii, and J. M. Seminario; 2009. *J. Chem. Phys*., **130**, 171101. Copyright 2009 by the American Institute of Physics.
- Current-voltage-temperature characteristics of DNA origami; by E. P Bellido, A. D Bobadilla, N. L Rangel, H. Zhong, M. Norton, A. Sinitskii, and J. M. Seminario, 2009. *Nanotechnology,* **20**, 175102. Copyright 2009 by the IOP Publishing.

the phosphorus bridges and base pair hydrogen bonds (*48*). Thus, DNA electric circuits will be able to provide benefits in terms of miniaturization, low power consumption, high efficiency, and low heat generation (*49*). A significant amount of research has been performed in the past decade on DNA-based field effect transistors (*50*) and DNA electronic sensors (*51*). Singh et al. reported low frequency DNA devices such as a transistors (*52*) that reached a maximum channel current of 1.8 μA for a gate voltage of 10 V at 120 KHz. Subramanyam et al. reported low dielectric loss values ranging from 0.11 dB at 10 GHz to 0.5 dB at 30 GHz in DNA thin films (*53*). Furthermore, DNA has been used to fabricate organic light-emitting diodes (OLED) using thin film techniques (*54*) and electro-optic (EO) waveguide modulators using DNA biopolymers (*55*).

3.1.1 Impedance Measurements on a DNA Junction

Electron transfer through DNA molecules has been studied intensely in recent years. There have been many attempts to reveal the electrical nature of DNA using various methods such as radiochemical (*56*), electrochemical (*57*), colorimetric (*58*), and chemiluminescent methods (*59*). DNA electrical properties have also been obtained from conductance measurements of DNA using an 18 base-pair double-stranded DNA (*60*), from the resistance measurement of DNA trapped by electrophoresis methods (*61*), and from temperature dependent conduction measurements (*62*). Furthermore, research on DNA conductance reported metallic (*63*), insulating (*64*), semiconducting (*65*) and even induced superconducting (*66*) behaviors. This does suggest that electron transfer through DNA is very sensitive to the experimental environment thus making experimental results a controversial issue.

The electrical behavior of DNA shows different results depending on DNA sequence (*67*) due to the ionic conduction of any residual buffer used in sample preparation (*68*). Salt trapped between DNA molecules was reported as a possibility to increase conductance (*64*). While several experiments (*69-71*) have been performed to characterize the steady-state direct current (DC) current-voltage (I-V) properties of

DNA, only a small number of experiments (*72, 73*) have focused on alternating current (AC) characteristics of DNA.

Here we focus our study in the AC characteristics of DNA because any useful behavior of molecules as devices would need to deal with AC signals. We use one micrometer long DNA attached to multi-thiol terminated G3 polyamidoamine dendrimers to interconnect to the two metal electrodes.

3.1.1.1 Experimental set up

The chip consists of 20 pairs of gold electrodes, each pair with 400 nm gaps fabricated by standard electron-beam lithography and lift off process (Fig. 4). Layers of 20 nm gold and 1 nm titanium are deposited on SiO_2/Si substrates.

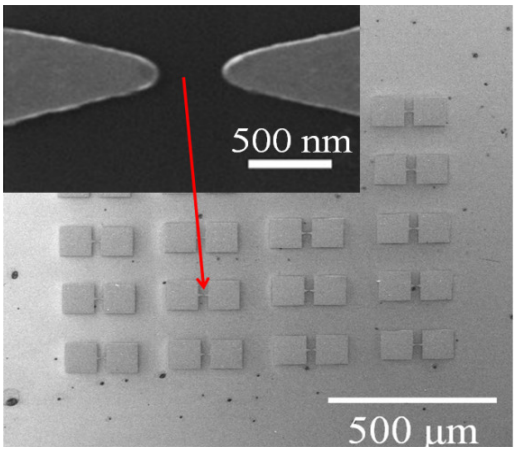

Fig. 4. Scanning electron micrograph image of the gold electrodes with finger-shaped gap of ~400 nm shown in the inset.

Randomly sequenced double stranded DNA (ds-DNA) ~1 µm long (3,167-base pairs) is modified with multi-thiol dendrimer at both ends to increase connectivity to the gold electrodes. The DNA solution is diluted to 1:4 ratio with 25 mM EDTA buffer solution (pH =7.4). The final concentration is ~17 ng/µL. An additional 1 µL of 0.5 M N-hydroxylamine is added for deacetylation of multi-thiolated groups. Then, the DNA solution is incubated for 30 minutes at room temperature. Before DNA exposure, the electrodes are carefully cleaned using ultrasonic bath with acetone for 2 minutes, and then washed with de-ionized (DI) water several times.

During DNA immobilization, the dielectrophoresis (DEP) method (*74*) is used to stretch DNA molecules. A DEP field of AC voltage of 2 V_{p-p} is applied, which plays an important role to strengthen the DNA samples and increase the possibilities of having DNA samples connected to the electrodes. Then, 2 μL of DNA solution are poured onto the chip. The frequency of the field is set to 1 MHz for 1 hour. Once each chip has been treated accordingly, the electrodes are rinsed thoroughly with deionized water. This process is repeated three times. Upon completion, the electrode is incubated at room temperature overnight at a clean room facility.

The DNA sample attachment to the electrodes is confirmed using AFM characterization; DC bias voltage yield the current response of the DNA material and the impedance of DNA is measured using AC bias as is described in Chapter II.

Electrode AFM images before (Fig. 5A) and after (Fig. 5B) DNA deposition, show the gaps filled with DNA chemically attached to the gold electrodes through dendrimers.

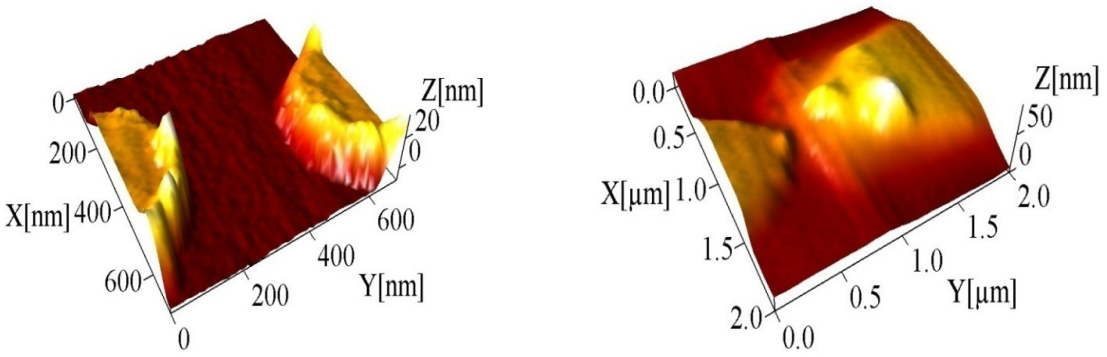

Fig. 5. Atomic force microscope images of a pair of gold electrodes before (A) and after (B) DNA deposition.

The I-V characteristics are measured to evaluate the electrical behavior of the junction before and after DNA deposition to the electrodes. Measurements are performed at room temperature. The resistance is in the 50 TΩ range before and after DNA deposition.

3.1.1.2 Results

Fig. 6 shows the noisy behavior of the chip impedance in the absence of DNA. The addition of DNA to the gold chip makes the components, and thus the module of the impedance smoother and more stable. The imaginary component of the impedance (reactance) oscillates from inductive to capacitive behavior when there is no DNA on the chip, but it is smooth and practically keeps capacitive behavior when the DNA is placed on the chip.

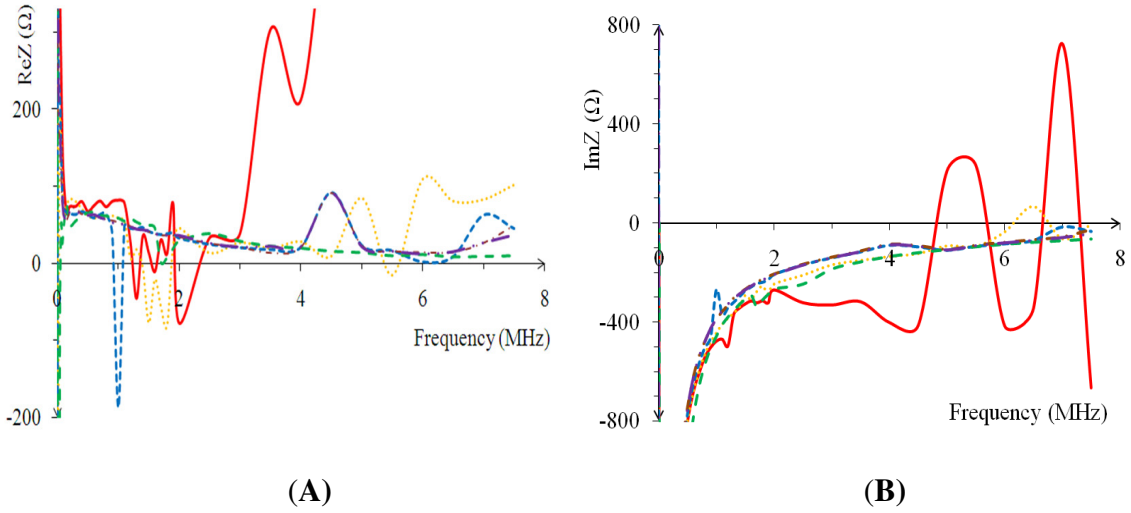

Fig. 6. Impedance in Ω, plots for the gold electrodes (A) real and (B) imaginary parts. Before deposition (solid line) and after deposition (discontinuous lines).

Due to the extremely high impedance for DC bias, the results of the experiment suggest that the current voltage characteristics of the DNA system are similar to that of a good insulator. However, the impedance shows strong frequency dependence, it increases from 281 Ω at 2 MHz to 1302 Ω at 7.5 MHz for the gold junction. Thus, we can conclude that DNA can be detected using the impedance spectrum response characteristic.

Furthermore, taking advantage of the lower resistances of DNA film at MHz, DNA based materials could be used for circuits at frequencies in the order of tens of MHz.

3.1.1.3 Summary and conclusions

One micrometer double stranded DNA molecules are immobilized between pairs of gold with gaps of 0.4 μm, and their electrical characteristics are determined under the application of constant and sinusoidal bias voltages.

Due to their extremely high impedance for constant voltage bias, the samples of DNA are excellent insulators; however, their impedance show strong frequency dependence in the range of 10 Hz to 7.5 MHz.

3.2 DNA Origami

DNA has the capability to assemble spontaneously in supramolecular aggregates, "DNA origami" and has been exploited to design well defined nanostructures, 3D shapes like a cube (*75*), an octahedron (*76*) and 2D shapes ranging from simple structures such as squares, rectangles, triangles to more complex ones (*77*); the specific base pairing of nucleic acids allows the design and fabrication of DNA-based devices for electronics, computing and medicine applications (*78-80*). In this case, a single strand of M13mp18 virus as scaffold is used; the triangular DNA origami is produced following the Rothemund's method (*81*) by Dr. Norton at Marshal University, the structure has approximately 90 nm per side.

The electrical characterization and potential application as sensor material for the proposed nanodevices is performed, the alternating current impedance at room temperature (*37*) and the temperature dependence (*36*) of the current through the triangular DNA origami in buffer solution is studied.

3.2.1 Experiment Methodology

Using a silicon wafer with 200 nm layer of silicon dioxide as substrate, 20 nm of platinum are deposited via electron beam evaporation using a conventional electron beam lithography process to fabricate the electrodes. Each chip consists of four platinum electrodes as shown in Fig. 7A; the left and right electrodes are separated by a

100 nm gap and the bottom and top electrodes are positioned at 2 µm from the narrow gap as shown in Fig. 7.

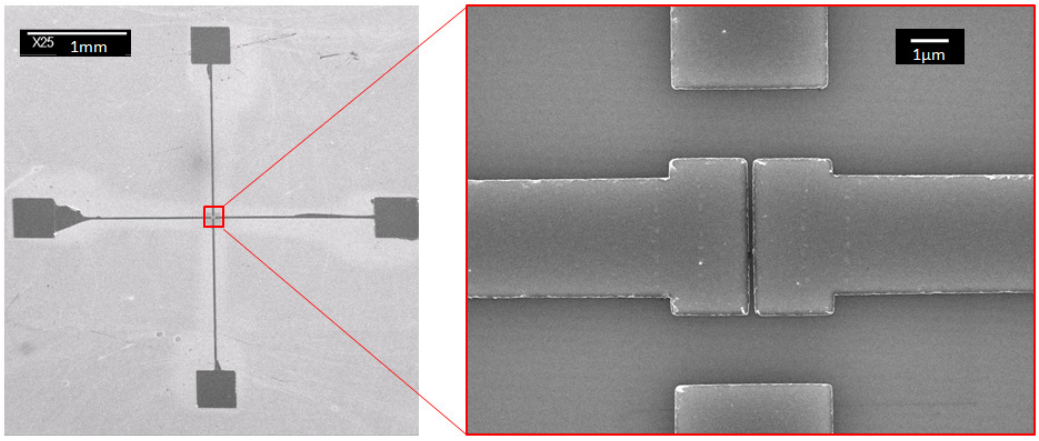

Fig. 7. Four-electrodes chip images using scanning electron microscope (SEM). Top and bottom electrodes are used for electrophoresis and left and right electrodes to apply the AC and DC bias.

The area shown in Fig. 7B is covered with 0.1 µL of 1 n-mole per liter of triangular DNA origami (Fig. 8) in 1x tris-acetate-EDTA (TAE) buffer using a micropipette. The deposited layer covers completely the 100 nm gap and the thickness is the gap depth 20 nm.

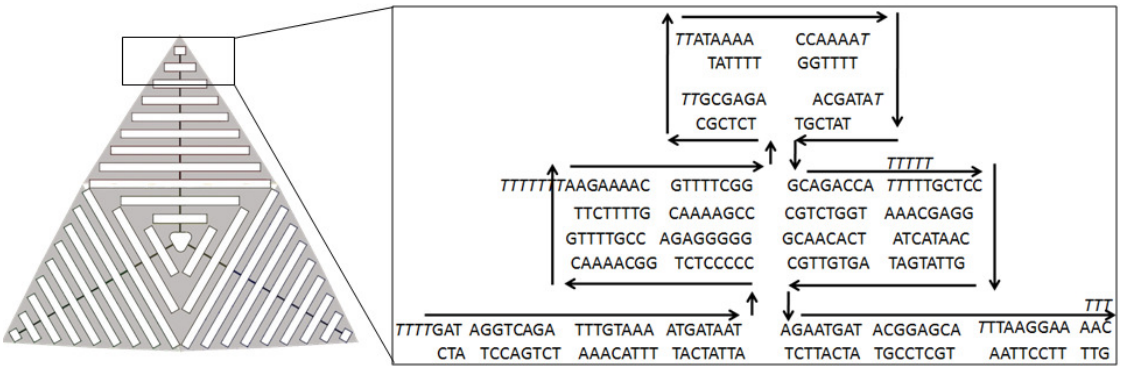

Fig. 8. Single strand chain of DNA used to create the triangle structure of the origami DNA and an example of the sequence used in one of the corners of the origami DNA (*81*).

3.2.2 Results: DNA Origami Impedance Measurement at Room Temperature

After the solution is deposited, an electric field produced by AC voltage of 2 V_{p-p} is applied for dielectrophoresis purposes between the top and bottom electrodes to help the orientation of the triangular origami on the 100 nm gap. The experiments are carried out as described in Chapter II.

The DC electrical characterization is performed applying a voltage across the left and right electrodes, a HP4145A semiconductor parameter analyzer (*32*) is used to apply a linear sweep voltages from -10 to 10 V and with sweep time of 1 s. As a control experiment we perform a DC and AC electrical characterization to the buffer solution deposited on a similar chip.

Fig. 9 shows the current-voltage characteristics of the chip before and after deposition of the DNA sample. A behavior similar to hysteresis, typical at the nanoscale, is observed due to the sweep frequency of 1 Hz.

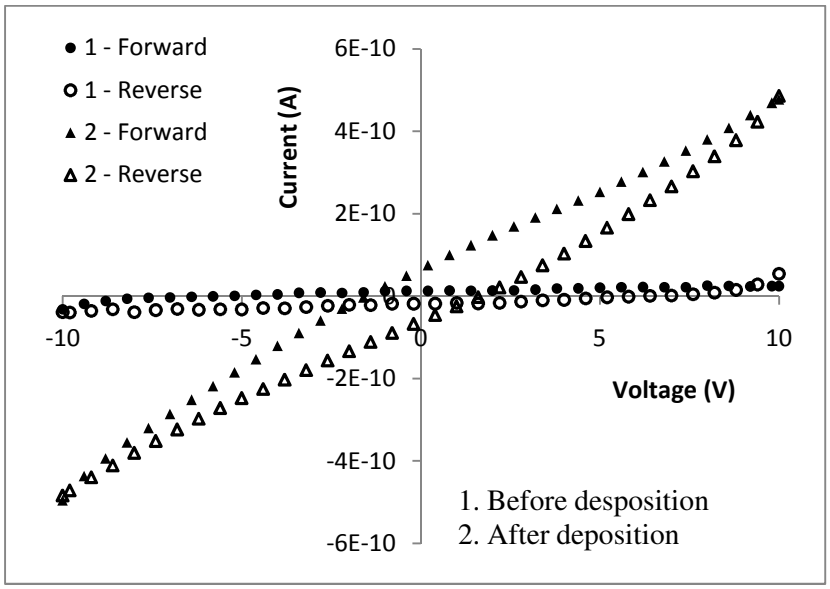

Fig. 9. Current-voltage characteristics of the chip before and after the deposition of the triangular origami DNA sample. Resistance before (1) deposition is ~400 GΩ and after (2) deposition is ~ 20 GΩ.

As a zero-order approximation we consider the impedance of the DNA sample is parallel to the substrate impedance due to geometrical considerations, one on top of the other with a field applied transversally to both. Table 1 shows the results of the impedance of the DNA sample when AC voltages are applied to the junction. The real and the imaginary parts of the impedance, resistance and reactance respectively, show a conducting behavior for frequencies higher than 100 kHz. Notice that in all cases the reactance is capacitive.

Table 1. Impedance values for the chip before and after deposition. Z_{chip} and $Z_{chip+DNA}$ are directly measured from the experiment and Z_{DNA} is obtained assuming a parallel configuration between the DNA and the chip.

Frequency	$Z_{chip}(M\Omega)$		$Z_{chip+DNA}(M\Omega)$		$Z_{DNA}(M\Omega)$	
	Resistance	Reactance	Resistance	Reactance	Resistance	Reactance
10^2	7.551	-251.552	17.165	-116.608	53.667	-212.587
10^3	24.101	-28.164	15.864	-13.678	40.419	-23.180
10^4	9.477	-14.650	6.944	-9.029	23.268	-22.309
10^5	0.031	-2.060	0.124	-1.497	1.404	-5.231
10^6	-0.011	-0.187	-0.006	-0.146	0.029	-0.657
10^7	-0.003	-0.012	-0.002	-0.010	-0.003	-0.050

The silicon dioxide substrate is a dielectric material with a low capacitive value and therefore with high impedance behavior at low frequencies, which have an effect in the nano and molecular response.

Fig. 10 shows the amplitude and phase of the impedance; the DNA impedance decreases and the capacitive effect at low frequencies tend to a resistive behavior at high frequencies. However, all data is consistent with an entangled behavior of the DNA origami and its substrate. Thus the determination of an intrinsic behavior of the molecular part of the junction is not possible as the DNA cannot be fully disentangled from the characteristics of the environment, the actual junction substrate in this case. It is expected that molecules are used to change the characteristics of substrates but we

cannot know its intrinsic characteristics. This makes the design of molecular circuits more complex than the design of present circuits based on lumped devices.

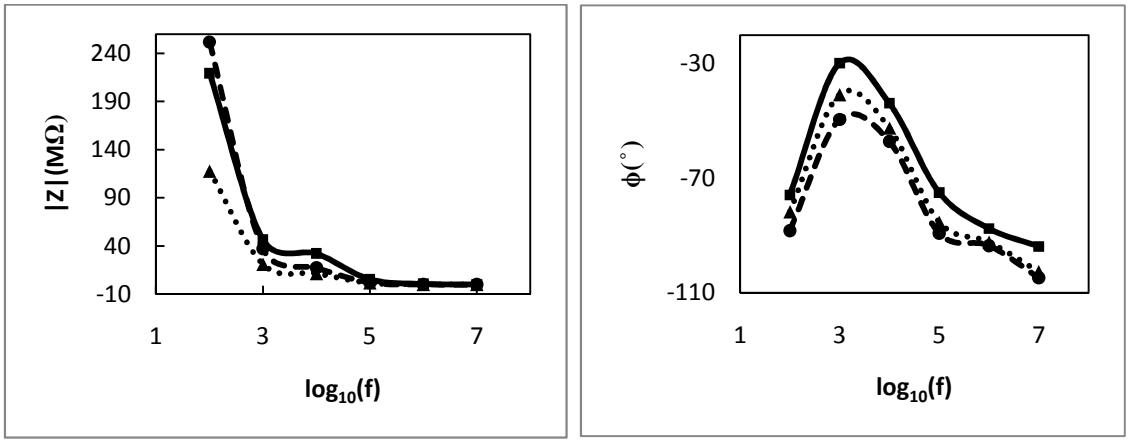

(A) **(B)**

Fig. 10. (A) Amplitude and (B) phase of the chip (dashed line), DNA and chip (dotted line) and the origami DNA (solid line) impedance.

Using a designed DNA origami we are able to transmit AC signals and determine the impedance of the deposited origami, which give us an idea of the behavior of DNA under the effect of AC signals. The frequency response indicates that the DNA shows full equivalent impedance decay at 100 kHz. Certainly, behavior of chip, buffer solution, and others cannot be perfectly disentangle from DNA and we believe that the molecule makes an entangled effect on the materials on which they are deposited; this entanglement will actually be an additional feature that have to be considered when dealing with properties at the nanoscale.

3.2.3 Results: Current-Voltage-Temperature Characteristics of DNA Origami

Below 240 K, the sample shows high impedance similar to the one of the substrate. At proximities of room temperature the current shows exponential behavior with respect to the inverse of temperature. Sweep times of 1 s do not yield a steady state, however sweep times of 450 s for the bias voltage secure a steady state. The thermionic emission and hopping conduction models yield similar barriers of ~0.7 eV at

low voltages. For high voltages, the hopping conduction mechanism yields a barrier of 0.9 eV and the thermionic emission yields 1.1 eV. The experimental data suggest that the electrical conduction mechanism is hopping. The results are consistent with theoretical and experimental estimates of the barrier for related molecules.

Due to the relatively short sweep time of 1 s the value of the current is not zero for zero bias voltage, showing a transient state that might be confused with hysteresis. Therefore, we increase the sweep time to 450 s to make sure we have a steady state response. Electrical current measurements at low temperatures show that the conductivity of the DNA sample decreases considerably, making it difficult to distinguish the electrical behavior of DNA from the one of substrate. In the range of 280-360 K, the substrate and the buffer solution show currents values approximately three times smaller than those when the DNA origami is present. In addition, a well-behaved temperature dependence of the DNA conductivity with an exponential behavior with respect to 1/T is observed. The conductivity increases by factor of 10 each 40 K. Observing the temperature dependence of the junction conductance, the charge transport process could be explained empirically by two possible mechanisms: thermionic emission and hopping conduction. All these mechanisms are summarized in Table 2.

Table 2. Temperature dependent conduction mechanisms.

Conduction mechanism	Characteristic behavior	Temperature dependence
Thermionic emission	$J \sim T^2 \exp\left(-q\frac{\emptyset - \sqrt{\frac{qV}{4\pi\varepsilon d}}}{kT}\right)$	$\ln\left(\frac{J}{T^2}\right) \sim \frac{1}{T}$
Hopping conduction	$J \sim V \exp\left(-\frac{\Delta E}{kT}\right)$	$\ln\left(\frac{J}{V}\right) \sim \frac{1}{T}$

Adapted from Ref. (*82*)

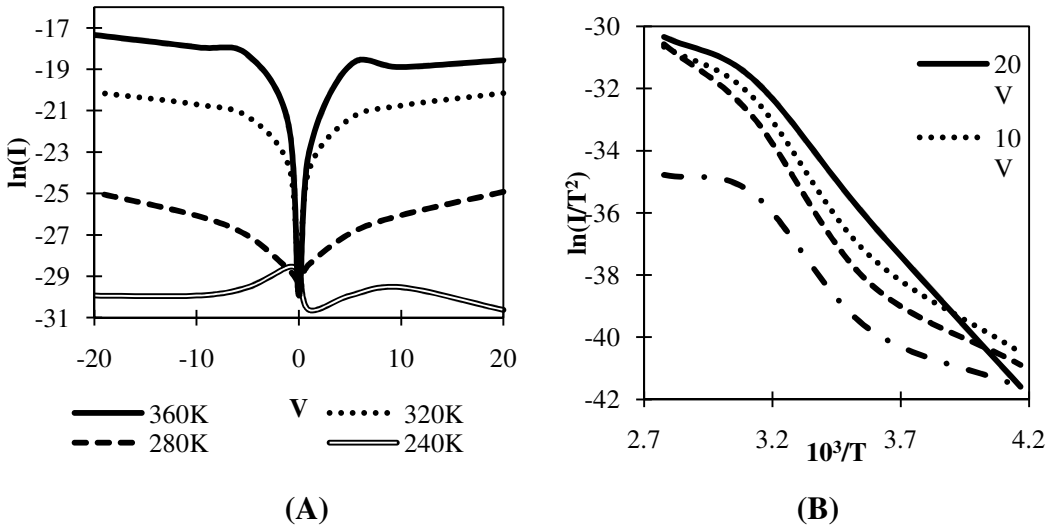

Fig. 11. (A) Plot of ln(I) versus voltage at selected temperatures of the DNA origami and (B) Plot of ln(I/T2) versus (1/T) at selected voltages. Current values are in ampere, temperature in kelvin and voltage in volt.

Fig. 11A shows the current through the DNA origami with the sweep time of 450 s; the current goes to zero for zero bias voltage confirming a steady state, each point is measured during 50 s. A linear behavior between 280 and 320 K is observed in Fig. 11B, yielding a barrier of ~0.7 eV for low applied bias voltage and ~1 eV (Table 3) for higher bias according to the thermionic emission model. For both conduction models at 20 V the linear behavior extends from 240 to 320 K. Both conduction mechanisms yield low barrier at low voltages (~1 V) and high barriers at high voltages.

The temperature-dependent current-voltage characteristic of a DNA origami solution trapped between electrodes with 100 nm gap has been examined. The electrical current through DNA origami obeys the hopping conduction mechanism for temperatures between 280 and 320 K and for high bias voltages (~20V) this range is extended between 240 and 320 K. Beyond this range, no conduction mechanisms could be assigned.

Table 3. Barriers obtained with thermionic emission and hopping conduction models.

Conduction mechanism	Applied bias (V)	Barrier (eV)
Thermionic emission	1	0.69
	5	0.97
	10	1.07
	20	1.19
Hopping conduction	1	0.72
	5	0.88
	10	0.87
	20	0.89

Despite the great findings, DNA based materials are not feasible to achieve our goals due to their environment reactivity, difficulties in the assembly, poor addressability and manipulation of single structures, and difficulties removing the structures from solutions. Thus, graphene sheets are now considered as the main fabrication material.

CHAPTER IV
GRAPHENE*

Graphene is a "novel" material recently proposed as one of the main alternatives to overcome the performance limitations of materials such as silicon and carbon nanotubes.

Graphene has been chosen as the most suitable material to achieve the goals of this research, in this chapter a literature review of graphene properties, applications and fabrication methods, along with our work on each of these topics is shown, including our published work on the fabrication mechanism using the unzipping of carbon nanotubes.

4.1 Literature review: Morphology and Structure

Graphene has been studied for more than 60 years (*83, 84*), but was only recently synthesized in 2004 by Novoselov *et al.* (*85*). They synthesized up to 10 μm length of single, double, and triple layer graphene structures by micromechanical cleavage of bulk graphite, attracting the interest of researchers to its properties and creating a potential usage for several applications. So far, several graphene properties are still unknown such as its toxicity, porosity, phase diagram, Curie point among others. Understanding graphene and its properties are important steps necessary to determine possible applications.

Vaporizing graphite by laser irradiation caused the quasi-0D carbon allotrope, fullerene, discovered in 1985 by Kroto *et al.* (*86*), although some calculations were reported in 1970 (*87*). Using a similar method, the quasi-1D allotrope carbon nanotube (CNT) was officially discovered by Iijima, in 1991 (*88*), however some authors had

---

* Parts of this chapter are reprinted with permission from:
- Graphene terahertz generators for molecular circuits and sensors; by N. L. Rangel and J. M. Seminario, 2008. *J. Phys. Chem. A*, **112** (51), 13699. Copyright 2008 by the American Chemical Society.
- Mechanism of carbon nanotubes unzipping into graphene ribbons, by N. L. Rangel, J. C. Sotelo, and J. M. Seminario, 2009. *J. Chem. Phys.* **131**, 031105. Copyright 2009 by the American Institute of Physics.
- Vibronics and plasmonics based graphene sensors, by N. L. Rangel and J. M. Seminario, 2010. *J. Chem. Phys.*, **132**, 125102. Copyright 2010 by the American Institute of Physics.

reported this structure since 1952 (*89*). The starting material of the CNT structures is the two-dimensional single graphite sheet, graphene.

Graphene is a two-dimensional honeycomb network one atomic layer thick of sp^2 carbon atoms. Its unit cell contains only two atoms; however, when layers are coupled, the unit cell increases in two atoms per layer. The coupling of layers is due to the weak Van der Waals forces between them. The stacking order of these layers could potentially be the Bernal or hexagonal stacking (ABABAB…) or the rhombohedral stacking (ABCABC…), which can be considered as a planar defect of the Bernal stacking or simply no stacking order also known as turbostratic graphite (*90*).

Structures with up to 10 graphene layers are known as few-layer graphene (FLGs), while structures with more than 10 and less than 100 layers are considered as thin films of graphite (*91*). The number of layers in a sample is very important and needs to be controlled because it may determine the properties and performance of the graphitic material. Initially, the number of layers of graphene was determined using an optical microscope, placing the graphene over a SiO_2 substrate, and showing a tone color for different numbers of layers. The number of layers has been determined based on the height differences of images taken by an scanning tunneling microscopy (STM), using different substrates such as Si (100) (*92*).

The atomic lattice structure of a single graphene layer on a SiO_2 surface was characterized by Ishigami *et al.* (*93*) using a combination of STM for atomic scale resolution, atomic force microscope (AFM) to compare morphologies between the graphene and SiO_2, and scanning electron microscope (SEM) for rapid reproducible placement of the scanning probe. Some perturbations, meandering, and both triangular and hexagonal lattices were noticeable. These observations showed that graphene followed the SiO_2 morphology, and that any other substrate will also take priority over its intrinsic corrugation morphology, determined by Meyer *at al*. (*94, 95*) using transmission electron microscopy (TEM) and freely suspending a graphene layer on top of micrometallic scaffolds.

4.1.1 Defects

The number of layers, types of edges such as zigzag or arm-chair, and topological defects such as vacancies, impurities, ripples, non-hexagonal polygons, etc., affect the properties and behavior of the graphene crystals (*96, 97*).

We have calculated the electronic properties of graphene ribbons with non-hexagonal polygons defect types (Fig. 12) and graphane, a two-dimensional graphitic material based on sp^3 carbon atoms instead of sp^2.

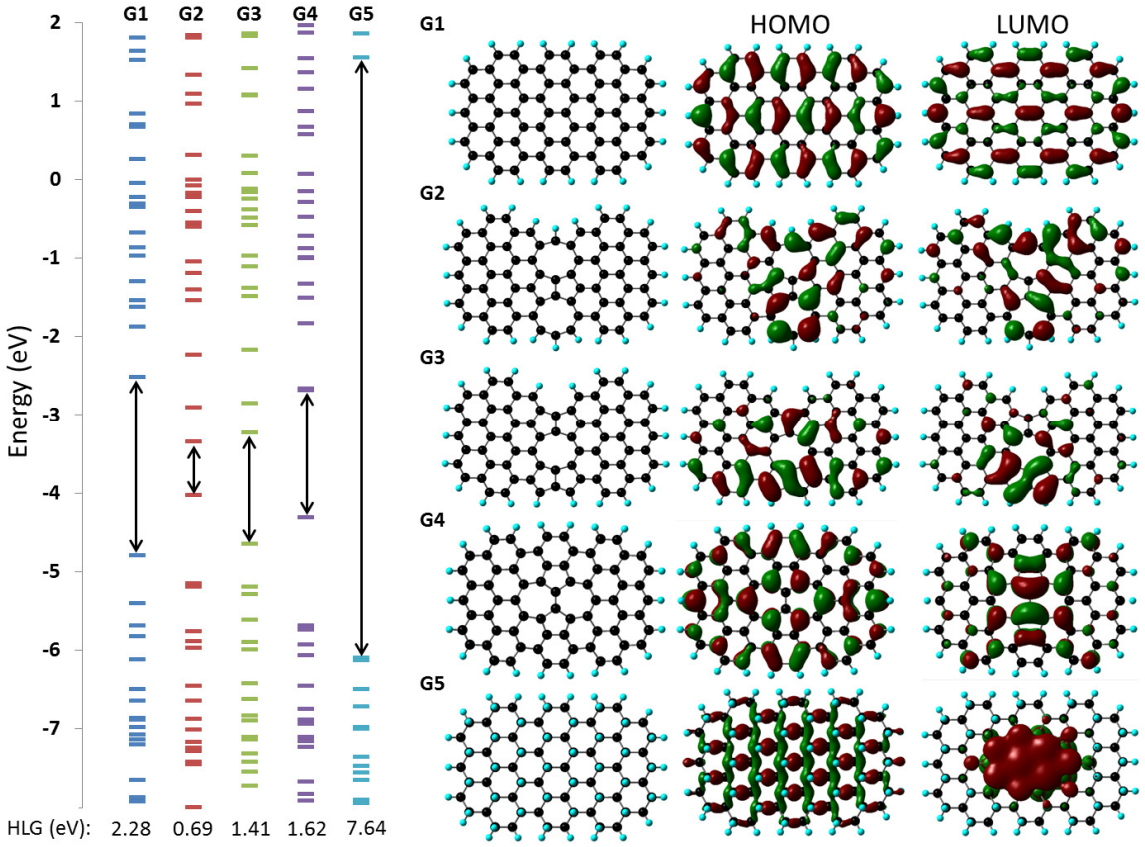

Fig. 12. Molecular orbital energies and shapes of the HOMO and LUMO for graphene without defects (G1), pentagon-octagon defects (G2 and G3), pentagon-heptagon defect (G4) and graphane (G5)

The conductivity of graphene can significantly be affected by the presence of defects on the surface. The HLG of a pristine graphene ribbon with no defects is 2.28 eV and can be decreased down to 0.69 eV by introducing combinations of pentagons,

heptagons and octagons on the surface (Fig. 12). More interestedly, is the electronic properties of graphene; the HLG is more than 3 times larger than the graphene, with delocalized molecular orbitals but with very large barrier (7.64 eV) make graphene a graphitic insulator material.

Using GENIP (formalism described on Chapter II), we calculate the current-voltage characteristics of the graphene ribbons with defects, as expected from the HLG gap values and the shape of the molecular orbitals, when non-hexagon defects are introduced on graphene the conductivity increases (Fig. 13). Also, it is observed that the sheet of sp^3 carbon atoms is an insulator material.

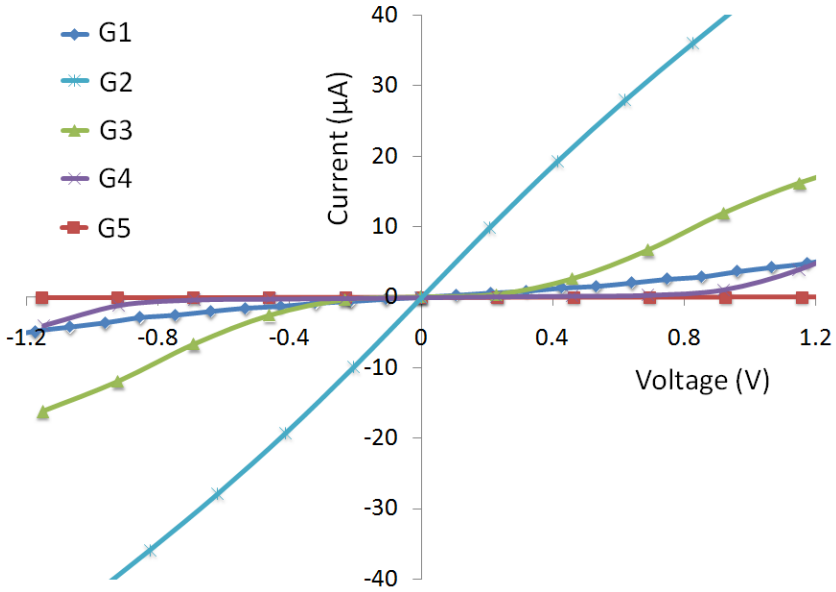

Fig. 13. Current-voltage characteristics of the graphene with and without defects and graphane. The conductivity of graphene (G1) is improved by adding defects (G2, G3 and G4) to the structure and significantly decreased in graphene (G5).

Graphene defects can be used to modify the electronic properties of a ribbon, and the versatile characteristics of graphene allow the development of graphitic materials with different properties and are promising successor material of the well-integrated silicon technologies.

4.2 Literature Review: Properties

The effective spring constants of a FLG (less than 5 layers) (*98*) and graphene membranes (8 to 100 layers) (*99*) have been experimentally measured using an AFM under ambient conditions. The AFM tip is calibrated and pressed over the suspended stacks of graphene sheets. Spring constants vary from 1 to 5 N/m for samples with thickness between 2 and 8 nm. From this data the Young's modulus is estimated to be 0.5 TPa for both FLG and graphene membranes, which is half of the reported value for graphite along the basal plane (*100*). After determining the FLG's Young modulus, a resonator was fabricated with a single layer graphene, producing modulus values between 53 and 170 GPa (*101*), similar to those of single-wall carbon nanotubes (*102*) and diamond. In 2008, Lee *et al*. (*103*) by Nano indentation measured the elastic properties and intrinsic strength obtaining values corresponding to a Young's modulus of 1TPa, positioning the monolayer graphene as one of the strongest material ever measured. Despite the fact that a lot of work has been done to determine the mechanical properties of the carbon nanotubes (*102*), the mechanical properties of the unrolled structure, graphene, is still in its infant stage, and so far most of the experiments on graphene have focused only on their electronic properties (*104*).

Using the tight binding model, the band structure of graphene was calculated first by Wallace in 1946 (*83*), and again by others in recent reports (*104*). It has been shown that graphene is a zero gap semimetal and graphite is a semimetal with a band overlap of 41 meV (*105*). After the discovery of graphene, several experiments have been performed to determine its electrical properties. Novoselov *et al.* (*85*) applied an external gate bias on samples with single and double layers by placing gold electrodes on top of the graphene. The single graphene and its bi-layer showed a tunable semiconductor behavior (*104, 106-108*). The band gap can be modulated upward until a minimum conductivity value is reached for all FLG; bandgaps cannot be modulated enough to force the FLG to act as an insulator. It is noted that the band gap depends on the impurity concentrations and the presence of a substrate (*109*). The behavior of graphene can be regarded as ballistic with mobilities in excess of 200,000 $cm^2V^{-1}s^{-1}$ for

electron concentrations of approximately $2x10^{11}$ cm^{-2} (*110*) and scattering distance around 0.3 μm (*91*). These high mobility values are found to be independent of chemical and electrical doping.

In contrast to quantum chemistry theory, where all interactions are treated by real (actual) Hamiltonians derived from first principles (*ab initio*) following a bottom-up approach, most condensed matter treatments are top-down approaches, which necessarily requires experimental information and therefore the creation of phenomenological or empirical Hamiltonians. Thus for the particular case of graphene, some authors have found that electric transport is better described by pseudo particles responding to a phenomenological relativistic equation (*111, 112*). This is because graphene low energy excitations are like massless Dirac-Fermions (*91, 113, 114*) that can explain the particular fractional quantum Hall effect, observed at room temperatures (*115*).

Experiments have revealed the effect of a magnetic field in single graphene and FLGs, producing a peculiar room temperature quantum Hall effect. Theoretically, graphite's diamagnetism (*116, 117*) and shortly later graphene's diamagnetism (*118*) were studied, and found to increase at low temperatures (*117*). Calculations of graphene nanoislands show that the shape of the edges (zigzag or arm-chair) (*119*) influence the magnetic properties, resulting in the zigzag system behaving as diamagnetic at high temperatures but as paramagnetic at low temperatures (*97*).

Such properties can be presented in carbon nanotubes by using materials like Fe filling the tube. The presence of under-coordinated carbon atoms similar to the carbons in the zigzag edges in graphene, present this ferromagnetic behavior in carbon-based structures (*120, 121*) but this is not enough to define the magnetic properties of the material, for the carbon nanotubes case, the magnetic properties are chirality, diameter and length dependent (*122*), and the presence of vacancies (*123*) or ad atoms (*124*) also affect the magnetic properties of carbon nanotubes.

As a result of these modifiable magnetic properties, an opportunity to obtain engineered magnetic materials has been proposed, which consists of graphene super

lattices patterned with nanoholes of different shapes, sizes and producing a material with combined semiconductor-magnetic behavior.

An experiment was recently (2008) performed by Nair *et al*. (*125*) where wave lengths between 250 and 1200 nm were focused on a sample consisting of a suspended single and double layer graphene, showing that the difference in opacity increases by 2.3% for each layer of graphene added. Variations in the wavelength did not show any effect in the opacity measurements, which implies that even white light, can be used to perform the experiment.

4.2.1 Electrical Properties

Different stacking order, geometries, edge type and passivation are considered in the study of the graphene sensors. The results show that graphene ribbons (actually molecules) resemble semiconductors but their HOMO-LUMO gaps are edge and passivation dependent.

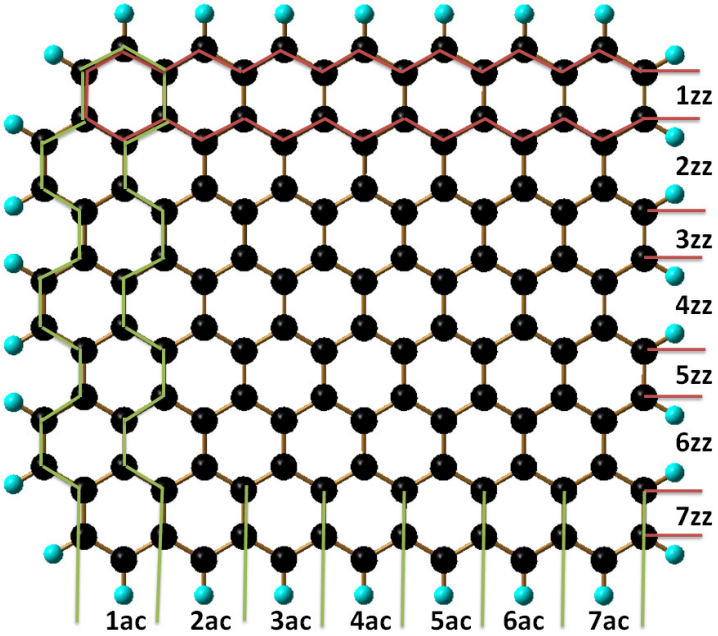

Fig. 14. Square graphene ribbon, the number of rings along each edge is used to label and characterize the size of the graphene ribbons used in this work. Shown with red is a unit with zigzag (zz) edge "1zz" and with green a unit of armchair (ac) edge "1ac". The size of the ribbon shown is 7ac×7zz.

Therefore, we add the hydrogen atoms to the ribbons obtained from Fig. 14 to warrant delocalized orbitals independently of the dominant edge. Despite of passivation effects, the HOMO-LUMO gaps of graphene ribbons affect the conductivity. Thus, we investigate few graphene molecules of different sizes starting from biggest one, the ribbon shown in Fig. 14; we calculate their HOMO-LUMO gaps as shown in Fig. 15.

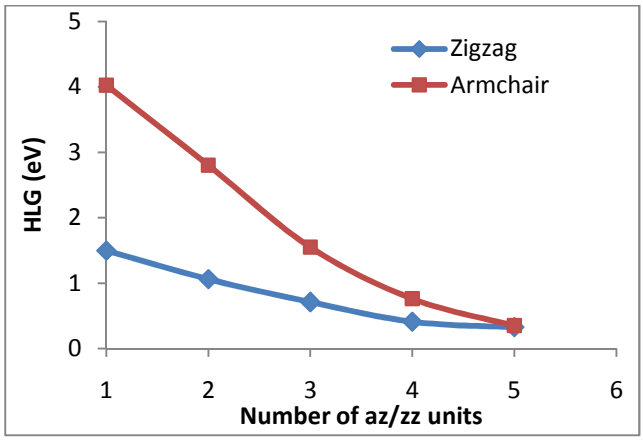

Fig. 15. HOMO-LUMO gap (HLG) with respect to the number of edged size of the graphene ribbon shown in Figure 14.

The dominant edge can influence the conductivity of the ribbons as can be seen in Fig. 15. The shape of the molecular orbitals affects the transport properties but the calculations show that both, armchair and zigzag ribbons feature delocalized molecular orbitals when they are passivated, if the ribbon is not passivated; localized molecular orbitals are found especially along the zigzag edges.

Current-voltage characteristics of armchair (Fig. 16A) and zigzag (Fig. 16B) edged graphene ribbons with and without hydrogen passivation are calculated to observe the effect of passivation on graphene. The results obtained with GENIP show that zigzag edged ribbons are more conductive than armchair edged ribbons, as is expected from the HLGs shown in Fig. 15. The effect on both zigzag and armchair ribbons is the same, when the ribbons are not passivated with hydrogen, the electronic density is localized at the edges, making the carbon at the edges more reactive and decreasing the conductivity of the ribbons (Fig. 16). When the ribbons are passivated the electronic

density is fully delocalized on the surface as plasmons and the conductivity is larger than the non-passivated.

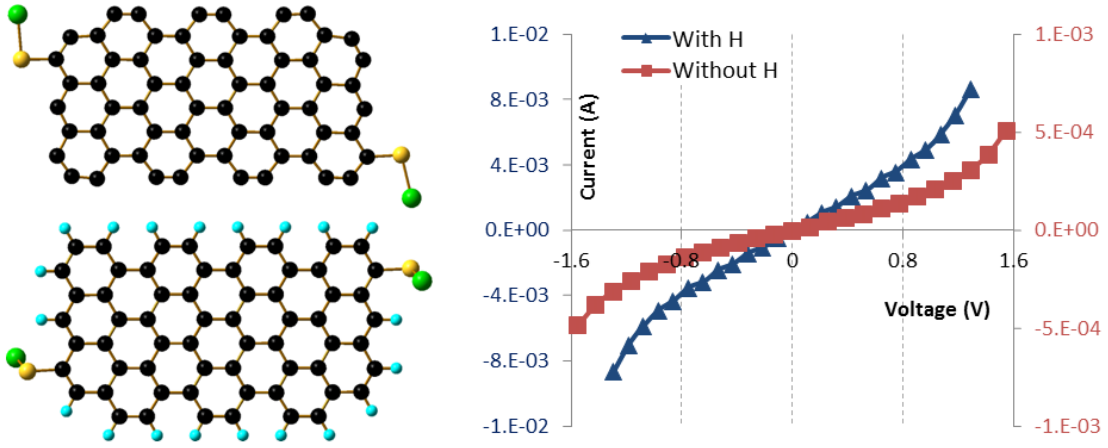

(A)

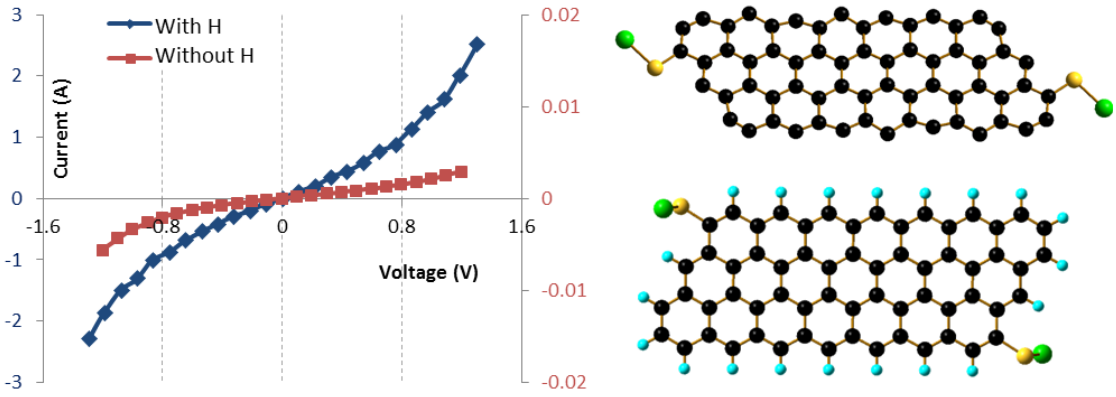

(B)

Fig. 16. Current-voltage characteristics of armchair (A) and zigzag (B) edged graphene ribbons and the effect of the hydrogen passivation on the conductivity.

Although for infinite and pristine graphene the theoretical band gap is zero, Fig. 14 suggests a finite HOMO-LUMO gap (HLG) for our small graphene molecules. It has been reported that armchair ribbons are metallic or semiconductors depending of their width and zigzag nanoribbons are mostly metallic (*126*). Experiment has been reported

that by decreasing the width of the ribbon the gaps increase (*127*), but there are not reported values for small graphene molecules with specific edge types.

4.3 Literature Review: Applications

The exceptional properties found for graphene suggest that the one atom thick crystal is an excellent candidate for a wide range of applications (*91*). It is sufficient to take a look at the large amount of already proposed applications for carbon nanotubes for example in photonics (*128*), as composite materials (*129*) among others, and study the possibility of replace them with the two-dimensional structure, graphene, which has already shown similar and better properties resulting in an improved performance in most of those applications (*110, 130*).

Graphene offers several advantages over current electronic devices. Starting with the electrical properties, graphene is projected to be the material of choice to replace silicon, which is now reaching its physical limits, opening a potential carbon-based electronics era. With mobilities that are five times larger in suspended graphene (*110*) than in silicon, graphene offers faster devices with lower energy dissipation due to its ballistic behavior (*131*), and with less noise than most semiconductors by using the bilayer graphene (*132*). Field effect transistors (*133*), single electron transistors (*134*), pn junctions (*135*), pnp junctions (*136*), and binary memory devices (*137*) have been fabricated. A graphene spin valve (*138*) showing giant magneto-resistance has also been fabricated, offering the possibility of using graphene for spintronics applications.

Applications in nanoelectromechanical systems (NEMS) such as resonators and high pressure sensors have been proposed, based on its mechanical properties (*101*). Graphene based composite materials have been suggested (*139*), and have recently shown exceptional results (*130*), where the glass transition temperature for poly(acrylonitrile) and poly(methyl methacrylate) have been improved by approximately 40°C and 30°C, using only 1 wt% and 0,05 wt% of functionalized graphene sheets, respectively.

The possibility of using graphene as a molecular sensor has been experimentally proven by Scheding *et al.*(*140*) resulting in a change in conductivity when gas molecules such as NO_2, NH_3, H_2O and CO with different concentrations are adsorbed on a graphene surface. This was later theoretically demonstrated by Hwang et al. for NO_2 and NH_3 (*141*) finding a high sensitivity, low noise, and a room-temperature operated sensor.

Fabrication of large graphene membranes, currently up to 100 μm (*142*), has opened the door to the possibility of measuring more properties experimentally, and their use on other applications. Large size membranes facilitate the study of the mechanical properties in graphene. Graphene impermeability to the second smallest atomic gas helium suggested that graphene membranes can be used as interfaces separating even two different phases of matter (*143*). On the other hand, their potential as a molecular filter can be reached by patterning with an electron beam different diameter holes in the graphene membrane acting like a sieve or mesh that separate wanted from the unwanted molecules but this is an approach that has not been fully explored.

Applications of graphene for hydrogen storage (*144*), spin filters (*145*), electrodes in solar cells (*146*), batteries, emitters, and even in quantum computing have been suggested and/or reported in the last year (*91*). Still, several potential applications of graphene synthesized just four year ago are by large unknown, and questions regarding its behavior, performance, and properties in the already proposed applications are still unanswered.

4.3.1 Electronic Circuits

We propose a molecular circuit on a two dimensional sheet, based on graphitic materials and defects. Suggested molecular circuit and components are shown in Fig. 17, showing materials with different conductivities (Fig. 17A) and performances as molecular devices such as logical gates (Fig. 17B). This novel circuit is expected to have superior electronic properties, high thermal conductivity, mechanical strength, elasticity and flexibility thanks to the intrinsic characteristics and properties of graphene.

High selectivity and sensitivity is expected, allowing the application of this molecular circuit as sensors.

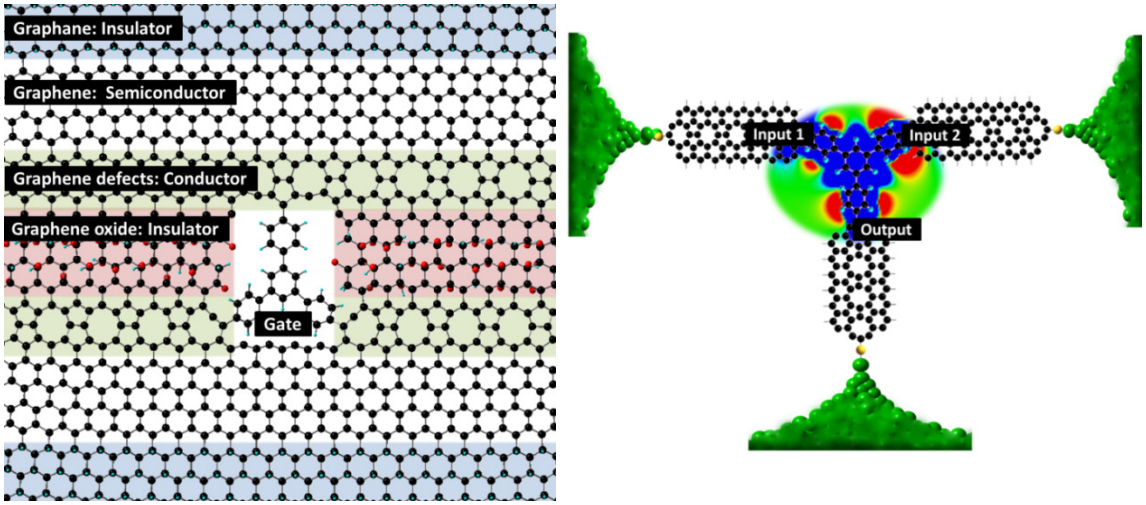

(A) (B)

Fig. 17. (A) Molecular circuit on a sheet based on graphitic materials. From top to bottom different graphitic materials are shown and used to design the molecular circuit: graphane, an insulator material based on sp^3 carbon atoms; graphene, a tunable semiconductor; graphene sheet with defects including impurities and combination of different polyhedrons improving the electrical properties and acting as conductors; and graphene oxide which is also an insulator. (B) Molecular gates made of graphene pieces and operating using molecular electrostatic potentials. Graphene ribbons with defects such as heptagons and pentagons are used as metallic wires to amplify and transport inputs and outputs of a molecular gate.

Challenges of this research are the scalability of the calculations. For small systems, the static conditions are calculated very precisely and can be taken to the highest level of precision simply by increasing the level of theory and increasing the size of the basis set until a satisfactory solution to the time-independent Schrödinger equation is found, or as in most cases, until the computational resources allow it.

A high sensitivity and selectivity network can be build using graphene ribbons, which couple molecular vibrations and molecular electrostatic potentials, acting as amplifiers able to even reach superconductivities and also can be used as a transducer converting signals into the usual current-voltage characteristics. Also, mechanical and

electrical properties of graphene yield to devices with exceptional performance, flexibility and scalability.

4.4 Literature Review: Fabrication Methods

Starting with Brodie in 1859 (*147*), many different attempts have been made to produce FLGs. After the success of the "scotch tape" pealing technique used for its discovery (*85*), the mechanical exfoliation technique (*148*) has been applied for this purpose. The mechanical exfoliation technique is a simple method in which the film thickness is determined based on the color of the SiO_2 substrate, but it is not appropriate for large scale fabrication and the films produced are usually uneven. The SiO_2 thickness (300 nm), the initial graphite material (largest possible grains), and the graphite and SiO_2 surfaces quality (freshly cleaved and cleaned) (*91*) are critical aspects in the success of this method.

By applying an arc-discharge to silicon carbide (SiC) crystals, nanographite ribbons were fabricated in 2001 (*149*) using a hydrogen atmosphere to avoid the formation of pentagons and therefore the non-planar structures. This procedure eventually inspired the currently known epitaxial graphite fabrication technique (*150*), where the SiC crystal is heated to about 1300°C in an ultrahigh vacuum, leading to the growth of FLGs with at least 5 layers and up to 100 layers. Since this is a thermal product, it is hard to functionalize these films for industrial applications. The high temperature is an inconvenience that is also present in the attempt to obtain FLG by heating diamond nanoparticles in an inert argon atmosphere (*151*). In this treatment, the required temperature is about 1650°C (*152*).

Chemical vapor deposition (CVD) is another strategy proposed to fabricate FLGs. One case of CVD is using camphor, which is heated between 700 and 850°C, pyrolyzed, and collected in nickel substrates (*153*). The CVD method is more practical for industrial applications but still not effective for the functionalization of films, and it is currently viable only on metal surfaces (*152, 154*).

The exfoliation (i.e. peeling away the layers) of graphite oxide however, seems to be a very promising technique for large scale fabrication of functionalized single graphite layers (*155*). This method consists of treating graphite with concentrated acids to obtain a sufficient oxidation of the graphite, and then thermally exfoliated at about 1050°C (*152*). Some of the difficulties of this method are to obtain the optimal oxidation and an adequate pressure during the heat treatment to reduce the possibility of having partially oxidized layers.

So far the best method to get the single layer graphene is the mechanical exfoliation technique or mechanical cleavage, particularly for research. It is cheap, simple, and does not require any extreme pressure or temperature conditions. However, this technique is not good for large scale fabrication and sometimes the sample obtained may be uneven. For large scale production the exfoliation of graphite oxide technique can be used. It can produce films in large scale but some stabilization treatment needs to be done, because the graphene obtained tends to agglomerate and becomes hard to functionalize.

Here we report a mechanism of the unzipping technique mechanism to fabricate graphene ribbons from carbon nanotubes, technique that addresses the problem of ribbon size controllability.

4.4.1 Mechanism of Carbon-Nanotubes Unzipping into Graphene Ribbons

Graphene nanoribbons (GNR) are promising materials for a wide range of applications, but their practical implementation requires edge and width controllability, low fabrication costs, and large scale production. Kosynkin *et al.*(*156*) reported a solution to fabricate these graphene nanoribbons by unzipping carbon nanotubes (CNT) treated with potassium permanganate in a concentrated sulfuric acid solution (H_2SO_4–$KMnO_4$). Their procedure, referred to from now as the “experiment”, allows the fabrication of uniform, narrow, 100–500 nm wide, semiconducting and metallic, straight edges (presumed zigzag), single and multi-layers GNR from multiwalled carbon

nanotubes of approximately 15 to 20 concentric single wall carbon nanotubes with diameters of 40–80 nm. These nanoribbons are soluble in polar solvents.

Other fabrication methods for GNR based on longitudinally cutting CNTs have also been reported recently. Jiao *et al.*(*157*) obtained narrower semiconductor ribbons by embedding multiwall carbon nanotubes in a polymer matrix and then attacking the surface with argon plasma etching. Cano *et al*. (*158*), on the other hand, obtained GNR by treating multiwall carbon nanotubes with lithium and ammonia. Oxidative-cutting was used by Liu *et al.*(*159*) to transversally cut long nanotubes into smaller tubes and Li *et al*. (*160*) provided insight into the atomic-level mechanisms of oxidation in carbon materials.

Graphitic material such as carbon nanotubes and nanoribbons can be used in a wide range of applications from lubrication to electronics to novel mechano-chemical devices;(*42, 91*) therefore, controlled chemical cutting of such materials to create novel structures could be a powerful technique in the nanotechnology toolbox. However, the mechanisms of how this is achieved are still far from clear.(*161*)

We aim to explain the controlled oxidation mechanisms of the experiment of unzipping CNT(*156*) using *ab initio* density functional theory molecular orbital calculations.

4.4.1.1 Methodology

To study the fabrication of graphene nanoribbons from carbon nanotubes, we use the armchair (5,5) CNT and (3,3) CNT as model systems. Their corresponding optimized structures are illustrated in Fig. 18A top and bottom. In the experiment, the attack occurs by a reaction of the CNTs with potassium permanganate (Fig. 18B) in a concentrated sulfuric acid solution, yielding the unzipping of CNTs and producing oxidized graphene nanoribbons, such as the optimized structure shown in Fig. 18C for the unrolled and oxidized ribbon obtained from Fig. 18A top. In addition, by reducing the oxidized graphene nanoribbons, the oxygen can be removed from their edges (Fig. 18D) thereby improving their conductivity.

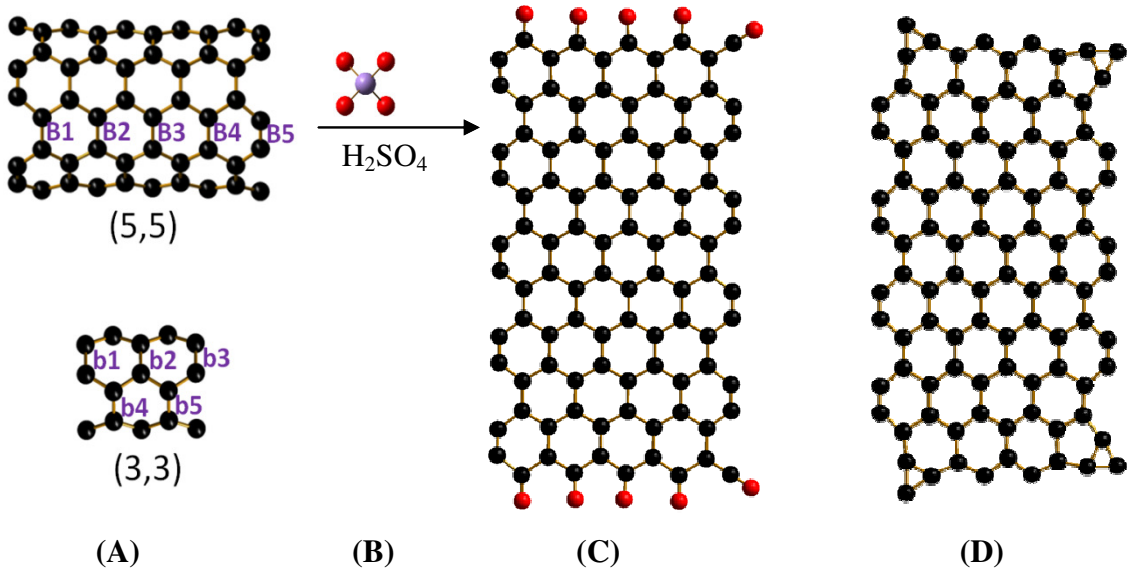

Fig. 18. (A) Structures of the (5,5) and (3,3) armchair carbon CNT (text in purple shows the carbon-carbon bonds used in the unzipping mechanism) (B) permanganate anion (C) oxidized graphene nanoribbon obtained from the unzipping of (5,5) CNT. (D) Structure of the ribbon after relaxation of (C) when the oxygen atoms are removed.

Calculations for the (5,5) and (3,3) CNT systems are performed at the B3PW91/6-31G(*d*) (*23, 24, 162*) and PBE/6-31G(*d,p*) (*163, 164*), levels of theory respectively.

Formation of manganate ester: The first step is the formation of manganate ester, therefore, we calculate the optimized structures of the permanganate bonded to the (5,5) CNT from B1 to B5 respectively as shown in Fig. 19(A-E).

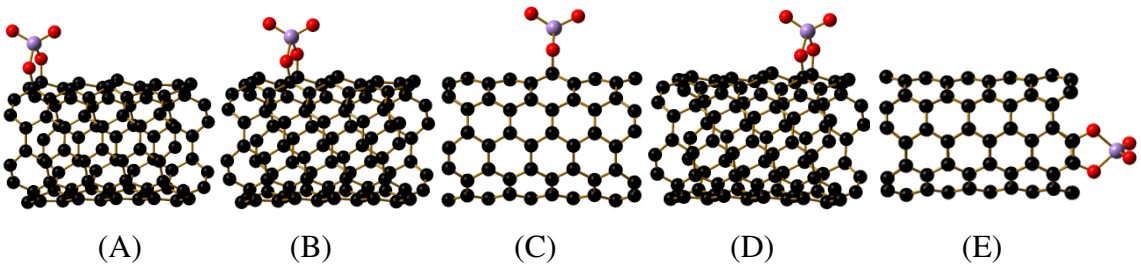

Fig. 19. Optimized geometries (A-E) of the structures obtained when approaching the opener anion MnO_4^{-1} to the CNT connecting initially two of the oxygen atoms from the permanganate to the B1-B5 bonds, respectively.

The total and binding energies, are shown in Table 4 for the (5,5) CNT, the permanganate anion (MnO_4^{-1}), and the anion bonded to the B1-B5 bonds along with the unbonded MnO_4^{-1} interacting in the neighborhood of the (5,5) CNT. Also shown in Table 4 is the distance of the carbon atoms participating in the ester formation.

Table 4. Energies and binding energies for the CNT, the permanganate, and the optimized structures of CNT when MnO_4^{-1} is bonded, unbounded, on B1 to B5, as shown in Fig. 18A. The C-C distance corresponds to the carbons bonded to the oxygen atoms.

(5,5)CNT, MnO_4^{-1} structures	Energy (Ha)	Binding energy (kcal/mol)	C-C distance (Å)
CNT	-3808.16569		
MnO_4^{-1}	-1451.66916		
MnO_4^{-1} on B1	-5259.87561	-25.6	1.62
MnO_4^{-1} on B2	-5259.87013	-22.1	1.62
MnO_4^{-1} on B3	-5259.85924	-15.3	1.62
MnO_4^{-1} on B4	-5259.86786	-20.7	1.71
MnO_4^{-1} on B5	-5260.08458	-156.7	1.42
Non bonded	-5259.85624	-13.4	

The energies shown in Table 4 suggest that the MnO_4^{-1}, the anion, attacks the CNTs bonds because the energy of the overall system when the permanganate anion is bonded (onto B1-B5) is lower than the energy when it is not bonded. The binding energy of the nonbonded, -13.4 kcal/mol, is about 2 kcal/mol higher that the energy of the weakest bonding of anion to the CNT (onto B3), -15.3 kcal/mol. Even though the lowest total energy (singlet multiplicity) corresponds to the permanganate anion bonded to the edge bond B5. The attack of the anion leaves the bond unbroken: the C-C distance in B5 goes from 1.24 to 1.42 Å, whereas in B1-B4, when the permanganate anion bonds to the CNT, the C-C distance increases 0.2-0.3 Å, leading to the breaking of these bonds and thus to the unrolling of the nanotube.

Opening of the CNT: The sequential addition of oxygen pairs to the CNT weakens the adjacent bonds and facilitates the adsorption of the next oxygen pair; here we use the (5,5) CNT which has an internal edge bond B1 and an external edge bond B5. Because of the large ratio of internal to edge bonds in the CNT, the small spread in binding energies for the B2-B4 bonds (Table 4), and the breaking of any of B2-B4 bonds under attack by an oxygen pair, we choose the middle bond B3 (as an on average representative of bonds in the mid-section of a long CNT) to start the unzipping process sequentially adding oxygen-pairs as shown in Fig. 20.

The first oxygen-pair attack starts on B3, the carbon-carbon bond stretches from 1.43 to 1.65 Å, as shown in Table 5. The oxygen pair also elongates 0.03 Å the neighbor bonds B2 and B4, making them weaker and vulnerable for the next two attacks as shown in Fig. 20C and Fig. 20D. As illustrated in Fig. 20E and Fig. 20F, the attack continues on the internal and external edge bonds B1 and B5, respectively, but the stretching is not enough to break the bonds and the carbon atoms stay bonded, avoiding the unzipping.

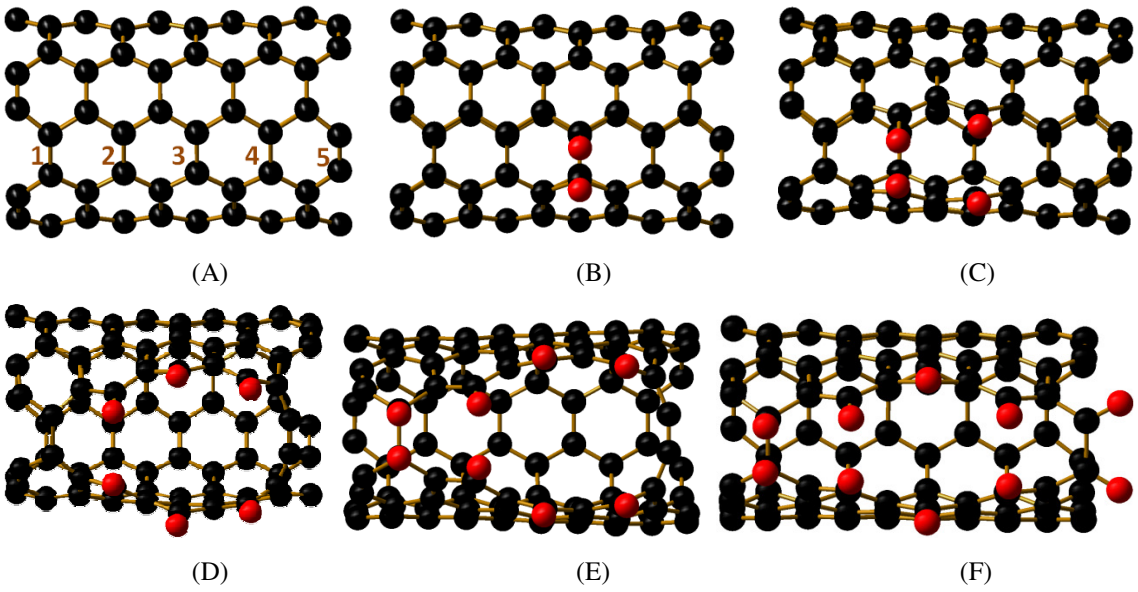

Fig. 20. (A-F) Optimized structures obtained through the gradual unzipping of a (5,5) CNT. Pairs of oxygen atoms are added sequentially. A new geometry optimization is performed after each pair addition of oxygen atoms.

Table 5. Total energies of each step in the studied unzipping process shown in Fig. 20 and Fig. 21 along with the lengths of the carbon-carbon distance in each oxidized bond.

Unzipping of CNT	Energy (Ha)	B1 (Å)	B2 (Å)	B3 (Å)	B4 (Å)	B5 (Å)
Fig. 20A	-3808.165693	1.43	1.42	1.43	1.44	1.24
Fig. 20B	-3958.377548	1.44	1.46	1.65	1.46	1.24
Fig. 20C	-4108.705771	1.38	2.66	2.98	1.47	1.24
Fig. 20D	-4259.187961	1.48	3.50	5.25	4.67	1.26
Fig. 20E	-4409.409991	1.55	3.11	4.95	4.62	1.26
Fig. 20F	-4559.823011	1.56	2.90	4.05	2.96	1.57
Fig. 21 (Fig. 20F with H passivation)	-4573.135841					1.59

However, when the edges of the CNT are passivated with hydrogen atoms the internal (B1) bond breaks with the attack and opens the tube as shown in Fig. 21. The attack of the oxygen pairs is not strong enough to break the external bond B5, which ends up with a C-C distance of 1.59 Å.

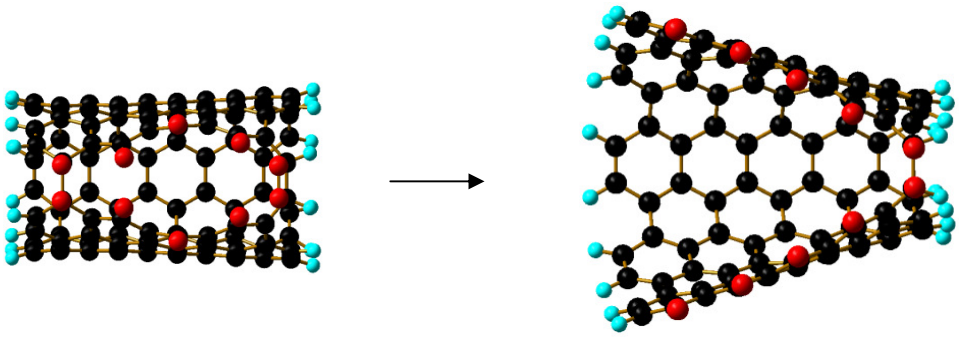

Fig. 21. The edges of the unopened (5,5) CNT are passivated with hydrogen atoms (left) and the optimized structure (right) opens only on the internal edge; there is not enough weakening to break the external carbon-carbon bond.

This finding suggests that if oxidation takes place along a longitudinal path containing an edge bond, then complete unzipping of the armchair CNT does not take place. This, may be due to an edge bond (such as B5 in Fig. 18A) being much stronger (about 16% for the armchair CNT of Fig. 18A) than the internal bonds (B1-B4), thus more difficult to break (see Table 5). Thus, in general oxidation of the armchair CNT

along a longitudinal cleavage path is not enough for the complete unzipping to take place.

Finally, in a zigzag (6,0) CNT (of diameter 5.3 Å) the cleavage path spirals along the tube in an angle about 30º with the CNT's axis. As indicated in Fig. 21 and Fig. 22, unzipping of the CNT takes place only when its rims are passivated with hydrogen atoms. Because of the high reactivity of the rims of the zigzag CNT(*165*) some of their C-atoms begin to locally cluster tighter together (not shown) when they are not passivated with H-atoms, effectively blocking the unzipping. Specifically, in runs we have made for an oxygen pair on the rim of an non-passivated zigzag CNT, the O-atom in the coordination three site moved to the nearest unoccupied site on the zigzag border (which has coordination two) forming an epoxy-like bridge between the two sites. A few small triangular C-rings formed on the zigzag rims too. This effect was more pronounced for smaller diameter tubes, as our (6,0) CNT (Fig. 22). For the latter CNT, in contrast to the armchair CNTs we have tested, the unzipping of the CNT may start with an oxygen-pair attacking a C-C bond in the zigzag edge, as H-passivation effectively transforms the C-atoms at the edge into coordination three sites. In fact, the passivated CNT becomes more stable by oxidation and breaking of an edge bond than a central bond along the oxidation path (not shown).

So far we have assumed that either the MnO_4^- anion or pair of O-atoms is readily available. We now present an *ab initio* model calculation showing how the unzipping might take place when an armchair (3,3) CNT reacts with potassium permanganate, KMnO4, in an acidic medium here represented by H_2SO_4+H_2O molecules. We show in Fig. 23 such a reaction.

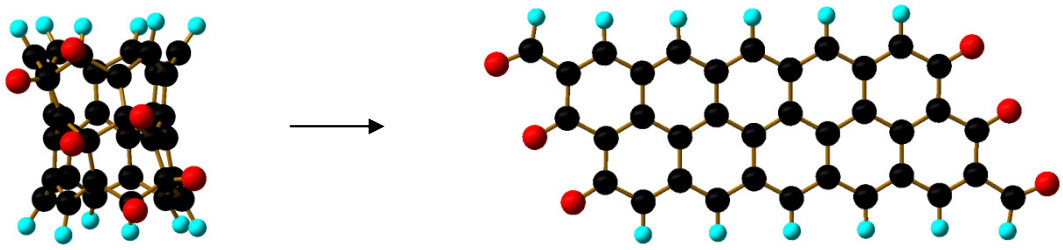

Fig. 22. Unzipping of a passivated (6,0) zigzag CNT upon oxidation of internal bonds (ends of the bond have coordination three) slanted by 30º relative to the CNT rim.

We let the attack take place along the longitudinal path of two internal bonds (parallel to the CNT's rims) located at the top of the CNT in Fig. 23A, starting from the back of the tube. As expected, bond-breaking takes place, yielding CNT-bound moieties [CNT](MnO_2)OH and [CNT]O---K^+---$SO_3(OH)^-$ at the sides of the broken bond (Fig. 23B). This system is further hydrated with three water molecules and then fully reoptimized (not shown). Next, we place another $KMnO_4$ group attacking the CNT on the second internal bond on the longitudinal path and add one molecule of each H_2SO_4 and H_2O. What takes place next depends on the angle of attack of the $KMnO_4$ molecule to the bond. For a slanted K-Mn axis (relative to the CNT's axis) as shown in Fig. 23C, so that the forward attacking O-atom is aligned with the CNT's axis, there is no bond breaking and thus no unzipping of the CNT (Fig. 23D). In contrast, if the K-Mn axis is roughly parallel to the axis of the CNT, as illustrated in Fig. 23E, with the forward attacking O-atom pointing downward to the hole left by the breaking of the first bond, the second attacked bond is stretched and broken yielding the complete opening of the CNT (Fig. 23F).

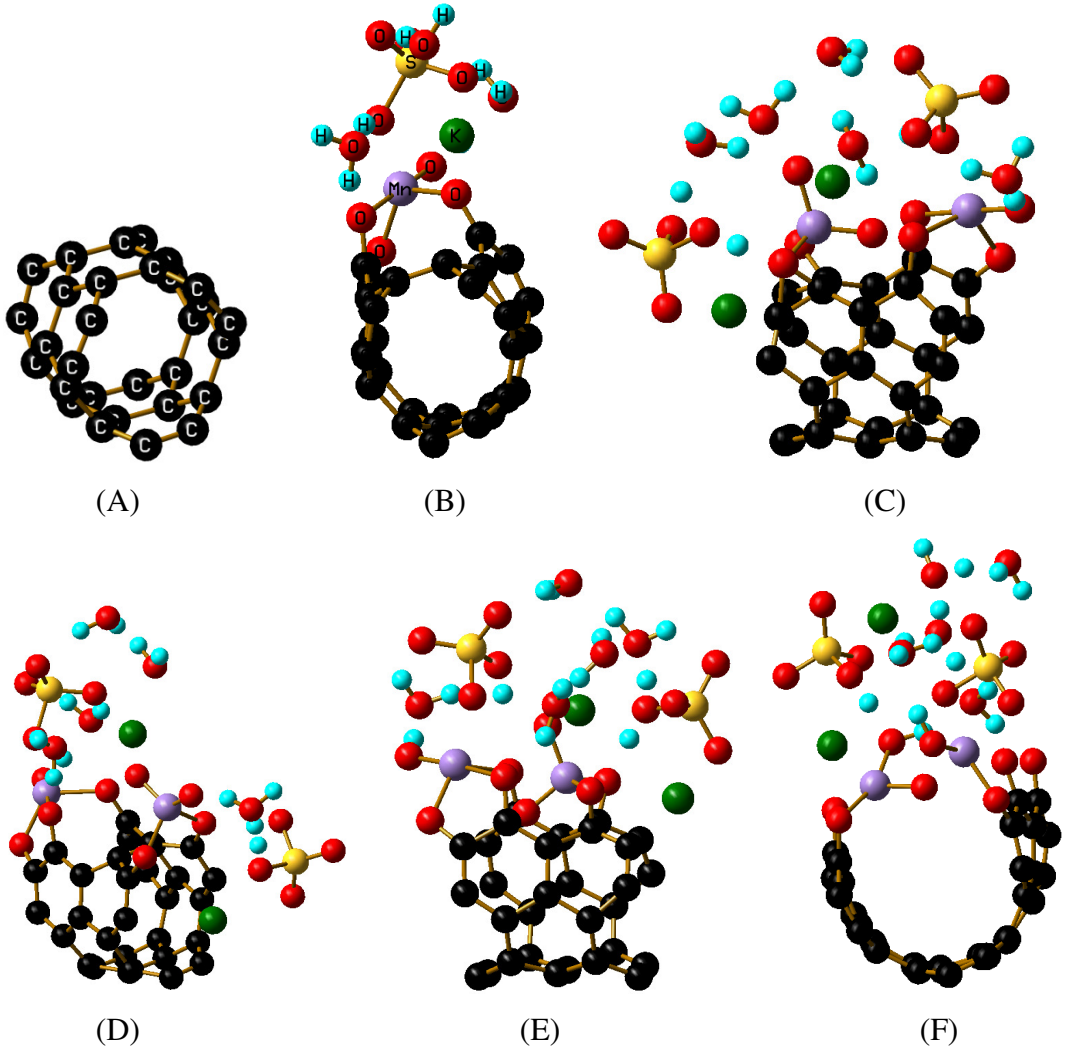

Fig. 23. Chemical reaction of an armchair (3,3) CNT with $KMnO_4$ on an acidic environment of H_2SO_4. The entire system has zero total charge. (A) A bare armchair (3,3) CNT. (B) CNT attacked on an internal bond by $KMnO_4$, acidic medium is represented by H_2SO_4, plus H_2O. (C) CNT is attacked on the same ring, in a parallel bond to the first attacked bond. The forward pointing attacking O-atom is about parallel to the CNT axis; acidic medium here is $2H_2SO_4$ plus $5H_2O$. (D) Final configuration for the reaction started in (C). The attacked bond does not break and the attacking MnO_4^{-1} anion migrates to the edge of the CNT. (E) Another configuration for a second attacking potassium permanganate. The forward attacking O-atom points downward to the hole created by the first attacking permanganate anion. The attacked bond and acidic medium are as in (C). (F) Final configuration for the reaction in (E). The attacked bond is broken leading to an unzipped CNT. Further flattening of the ribbon is impeded by the moieties product of the reaction.

In summary, pairs of oxygen atoms from the permanganate anion bind and break the internal C-C bonds in the CNT, the stretching of the bonds involved in the first attack weakens the neighbor parallel bonds making them more vulnerable for the next oxygen

pair attack, which takes place longitudinally along the CNT, consistent with what was found in the experiment. However, the strength of external bonds in the armchair CNTs is not defeated with the permanganate attack and therefore these bonds cannot fully open yielding ribbons with amorphous shapes and edges. Furthermore, our results suggest that the initial attack takes place in the middle section of the CNT because the population of B3 bonds is higher. In addition, bonds in the unzipping path whose ends have coordination three are most likely broken as inferred from the fact that armchair bonds are broken by the attack of an oxygen-pair and the zigzag bonds, though stretched, remain unyielding. This difference in strength of edge bonds for armchair and zigzag CNTs suggests that bonds with an end-site connected to C-atoms only are more likely to be broken under the attack by oxygen pairs.

On the other hand, there is no much difference whether the anionic MnO_4^- or the neutral $KMnO_4$ species are used or even when the highly possible formed, $HMnO_4$, is used in the calculations. When $HMnO_4$ attacks, it breaks internal bonds just as in the anionic case and when the attack is on an edge bond, no breaking takes place. These results suggest that all CNT end up in zigzagged edge ribbons no matter what we start with; the unfolded ribbon have zigzag edges along the oxidized unzipping path. Nevertheless, information will be very useful from additional experimental evidence as theory and experiment can have complementary information about the systems being analyzed rather than a mutual validation or exclusion of each other.

CHAPTER V
NANO-MACRO INTERFACE TO READ MOLECULAR ELECTROSTATIC POTENTIAL BASED ELECTRONICS*

Molecular potentials are unreadable and un-addressable by any present technology. It is known that the proper assembly of molecules can implement an entire numerical processing system based on digital or even analogical computation. In turn, the outputs of this molecular processing unit need to be amplified in order to be useful.

There several ways and methods to strategically arrange molecules on a surface. One of the earliest developed ways is to manipulate molecules on a surface by using the scanning tunneling microscope (STM) (*166*). Other methods include several variants of controlled self-assembly monolayers (*167*) and the use of replicative molecules, such as DNA, to fabricate and locate molecules such as amino acids on a surface (*168*). These techniques are still being developed and will hopefully provide new ways to utilize molecules as electronic devices.

However, no matter how well chemistry can assemble molecules into systems, the molecules need to be linked or interconnected to build electronic systems. The solution to this addressing problem is something that may take an exponentially more complicated turn than the one created by the assembly of the molecules on a surface. It is our view that interconnection between neighboring molecules, as opposed to random molecular connection, would be the best resolution; with perhaps ideas similar to a cellular automata (*169-171*) or the like.

A technique that fulfills the requirements needed for the development of molecular circuits is the use of molecular potentials to encode and process information. The molecular potentials "outside of a molecule" vary between +3 and –3 V (*172*).

---

* Parts of this chapter are reprinted with permission from:
- Nano-micro interface to read molecular potentials into current-voltage based electronics, by N. L. Rangel and J. M. Seminario, 2008. *J. Chem. Phys.* **128**, 114711. Copyright 2008 by the American Institute of Physics.
- Molecular electrostatic devices on graphite and silicon surfaces, by N. L. Rangel, J. M. Seminario, 2006. *J. Phys. Chem. A*, **110** (44), 12298. Copyright 2006 by the American Chemical Society.

They were first used to determine the reactivity of molecules (*7, 172, 173*). Later, they were used to create indicators or descriptors (*174, 175*) to determine several properties of molecules. These indicators and descriptors have also been used in bulk materials with extrapolation to different phases (*176*). As such, positive potentials outside a molecule or in the space where it interacts with others imply a shortage of electrons while negative potentials imply an excess. The practical importance of molecular potentials is the possibility to use them to act on and modify the potentials of neighbor molecules.

With this in mind, several molecular gates have been designed and studied. Consequently, these type works have made it possible to determine properties of materials such as energetic materials, biological and chemical agents that are very difficult to determine experimentally (*6, 177-181*). Another important application of molecular potentials is their use to determine a set of point charges that better reproduce the potentials on a surface around a molecule. This provides much better consistency with concepts of charge and bonding used in chemistry (*182, 183*).

5.1 Molecular Logic Devices

The use of molecular potentials also include applications to hydrogen bonding interactions (*184*). It has been demonstrated that the topography of the molecular electrostatic potential (MEP) provides a measure of the cavity dimensions and an understanding of the hydrogen-bonded interactions involving primary and secondary hydroxyl groups. The MEP topography qualitatively explains the binding patterns of the guest molecule with the host.

Molecules using MEP were able to perform logical operations. One of these included an OR operation (*4, 5*) to yield an output of 1 if at least one of its inputs is 1, otherwise it yields 0. It has also been demonstrated that other molecular single gates, such as organic molecules less than 1 nm^2 in size that consist of two or more isolated functional groups such as ethynyl and butyl (*10*), are able to successfully interconnect to

each other. This opens the door to extremely low-power consumption molecular devices (*185*). The dihydroxylbenzene molecule is an OR logic gate (*13*). The 1,3,5-trifluorobenzene (TFB) molecule could function as a AND gate when input signals are applied to the 3- and 5-fluorine atoms and the output signal is taken from a buffer Be atom at 3.2 from the 1-fluorine (*3*).

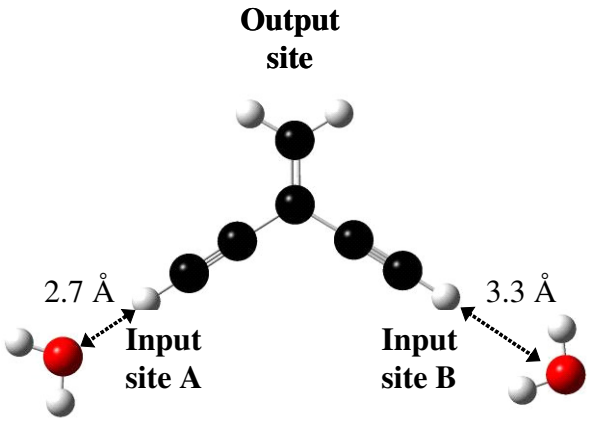

Fig. 24. The OR-gate based on 1,1 diethynylethene (DEE) also known as 1,4 pentadiyne, 3 methylene. The two water molecules in the figure provide the negative and positive potentials to the gate inputs, A and B. The output is read from the "Output site".

In this chapter, we test the effect on a molecular OR-gate (Fig. 24) of two substrates, planes of graphite and a hydrogen-passivated surface of silicon. The electrostatic potential of water molecules are used to model the inputs to the logical gate. Then, we use aza-OPE molecule to amplify the output of a molecular gate and amplify the signal through changes in its current-voltage characteristics; however, the addressability and fabrication of a single molecule is inconvenient for practical purposes, thus the same concept is confirmed thanks to the morphology of graphene ribbons, its atomic thickness allow us to read signal from self-assembled molecular monolayers and amplify them through traditional current-based electronics. Using *ab initio* methods, we computationally demonstrate the amplification of molecular potential signals into currents that can be read by standard circuits.

Fig 25 shows the MEP of the molecular device and the water molecule used as the input to the device. The color-coded scale ranges from - 2 V to 2 V covering colors from red to blue, respectively. Any potential smaller than 2 is represented by red; and by blue, potentials smaller than –2 eV. This color scale allows us to precisely determine if a region in the molecule shows negative or positive potentials. As expected, potentials in the neighborhood of the nuclei are positive showing a blue region when the atoms are exactly on the MEP plane.

The selection of the electrostatic potentials of water to simulate an input in the molecular gates is simply based on its dipole moment. There is no special constraint other than the need to have a simple dipolar molecule, which unambiguously shows its polarity. In principle, any pair of positive and negative molecular potentials could be used for proving the concept.

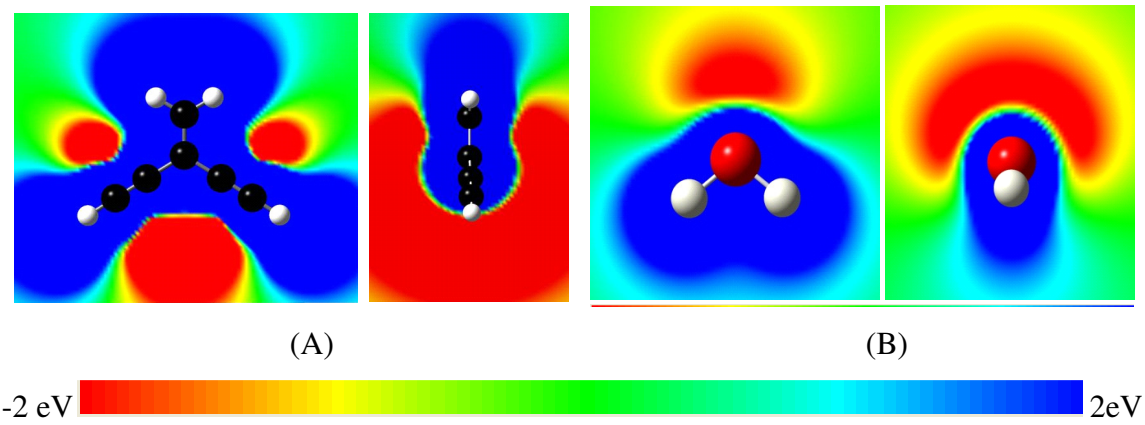

Fig. 25. Shows the MEP on a plane perpendicular to the molecular plane that includes the C_{2v} axis of the molecule. Thus only two carbon atoms lay on this perpendicular plane; all other atoms are above or below the plane.

Fig. 25A; however, on the right view, they show a mix of red and blue colors because these hydrogen atoms are not on the plane of the MEP. The MEPs clearly indicate the effects of charge accumulation in a molecule. For instance the red regions are due to the presence of double and triplet bonds in the DEE molecule or to the two lone pairs in the water molecule. Unambiguously, for the simple case of water, the oxygen side can be used as a negative potential probe and the hydrogen side as positive.

Fig. 26 shows the MEP of graphene and silicon sheets. The most striking difference between the two surfaces is the potential distribution on the active sites. For graphene, we calculate the MEP on a surface of one sheet and two sheets. The results are very similar. Both show a strong positive potential on the plane of the sheets and a strong negative potential above and below the surfaces. We can notice the negative potential between sheets in Fig. 26B; this channel becomes a conduction path for positive ions such as Li_+ in lithium-ion batteries. Notice that the top view in Fig. 26B shows all atoms from the two sheets. In this case the separation between sheets is chosen to be 3.35 Å, which corresponds to the experimental value in graphite. These strong changes in the MEP at neighborhoods of graphite require that the substrate be fully considered in the design of the gates in order to unambiguously determine the behavior of molecules passing information encoded in molecular potentials.

On the other hand, the silicon sheets show a more relaxed potential distribution at the neighborhood of the surfaces. Figures 3c and d, corresponding to one and two silicon sheets, respectively, yield a potential practically near to zero for both cases. This is confirmed by the green regions, which show up near the sheets in the case of Fig. 26C and Fig. 26D, as opposed to the red regions in Fig. 26A and Fig. 26B.

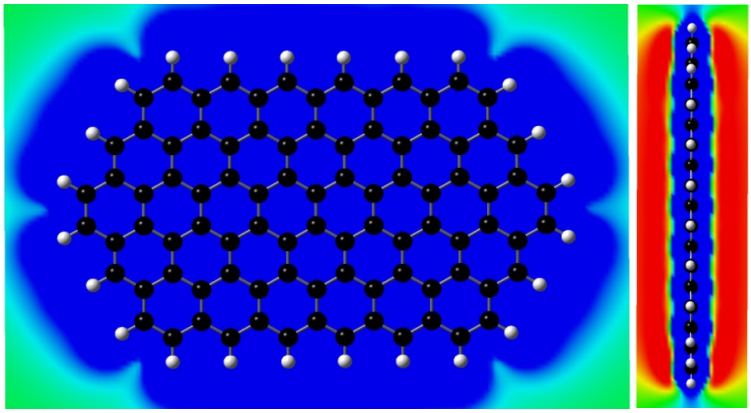

(A)

Fig. 26. The MEP of the graphene used as the substrate. A) One layer, B) two layers. The MEP for hydrogen passivated silicon used as a substrate C) one layer, and D) two layers. As a reference for the size, the C-H bonds are 1.07, C-C 1.42, Si-H 1.47, and Si-Si 2.34.

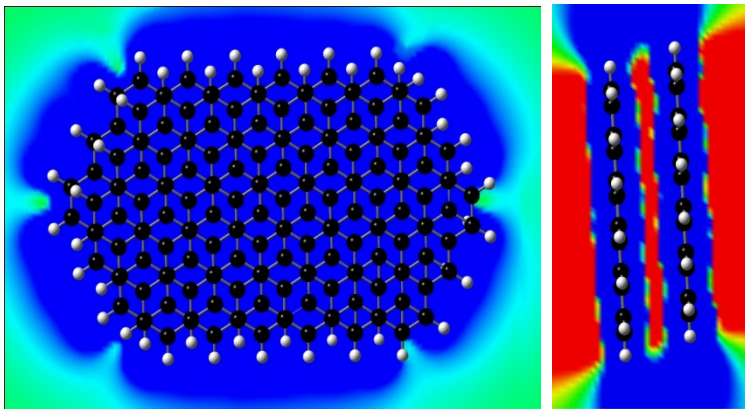

(B)

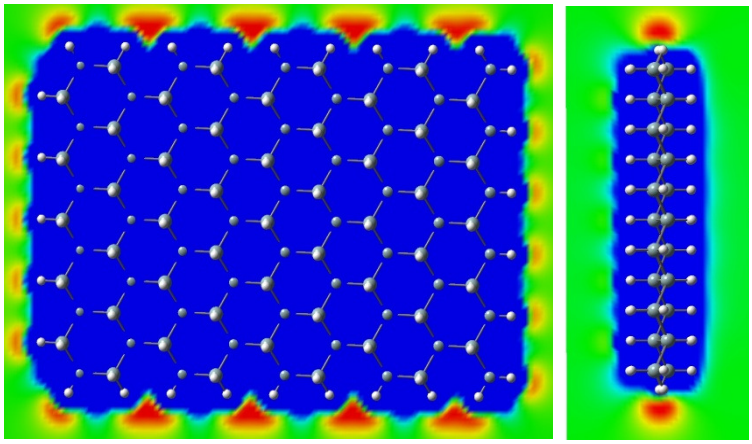

(C)

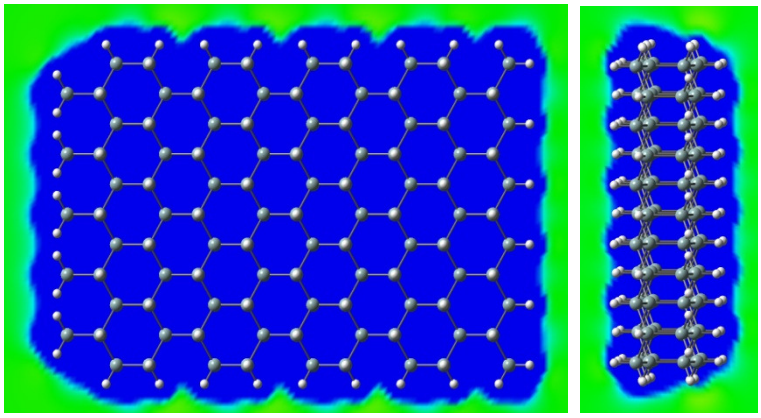

(D)

Fig. 26. Continued.

5.1.1 Results and Discussion

Fig. 27 shows the supported molecular gates in graphite and silicon sheets.

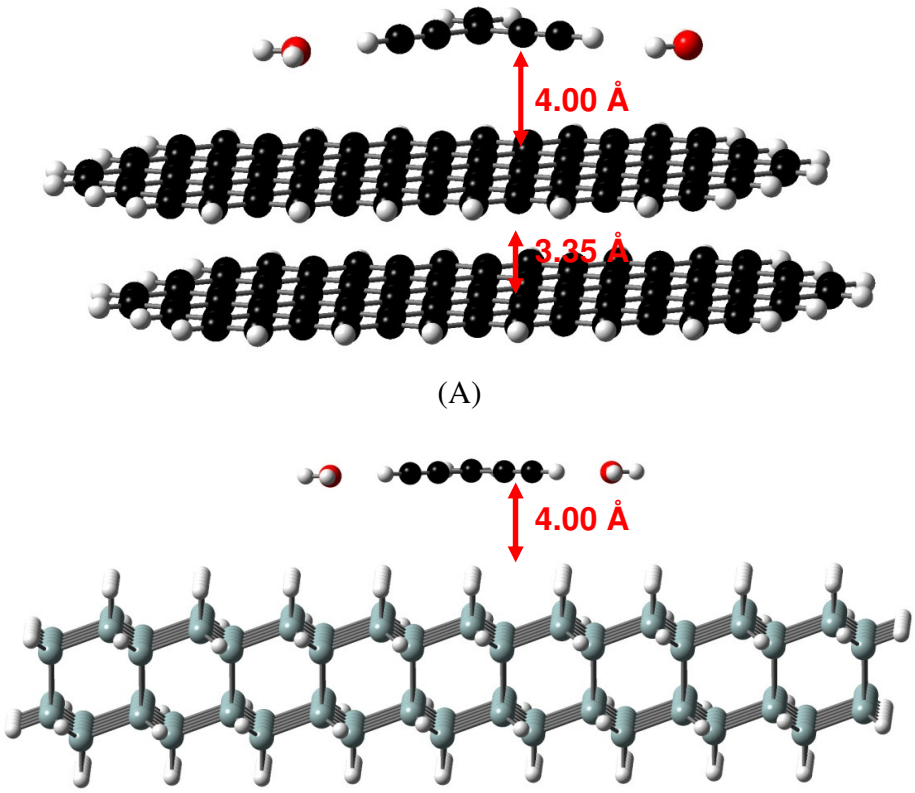

Fig. 27. The molecular logic device on a substrate of (A) graphite and (B) hydrogen-passivated silicon. The molecule is 4.00 Å above of the substrates. For each case, calculations are performed with one and two layers.

Since the OR gate has two inputs, there are four possible input combinations: 00, 01, 10, and 11. Thus for an OR gate the outputs are 0, 1, 1, and 1, respectively. And for an AND gate the outputs are 0, 0, 0, and 1, respectively. By symmetry considerations the 01 is identical to the 10 thus we just need to analyze three combinations of inputs for the gate in each substrate.

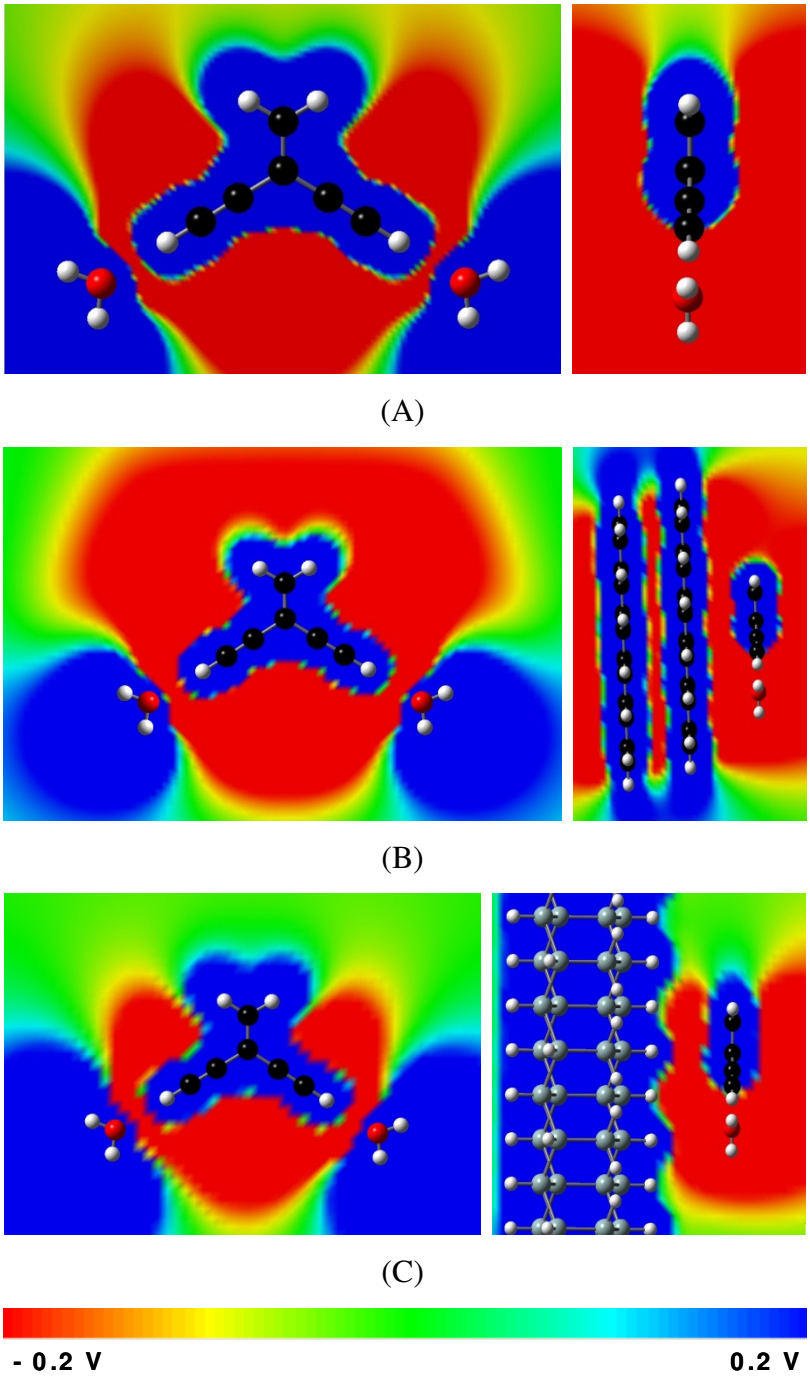

Fig. 27. Shows the case when the two inputs are negative (00) for the molecular gate with and without the substrates. The application of the 00 inputs using the negative side of the water molecule in the inputs of the gate yields a slightly negative potential at the output site. The green-yellow region is unambiguously negative, in the range of ~0.1 volts. The introduction of the two negative potentials of water changes the MEP of the isolated molecule.

Fig. 27A, have only three small regions of negative potential, covering most of the molecule with negative regions. The strong negative potential when one small graphene sheet is used washes out the potential at the output (not shown) because the border effects; however, potentials are back to normal if one or two sheets of graphene are used as shown in Fig. 27B. This is perhaps a more realistic situation as a few layers of graphene would be present in practice. Surfaces not shown in this paper can be seen in the supplementary information.

On the other hand, the passivated silicon substrates do not change much the MEP distribution obtained with a single molecule. Fig. 27C shows the MEP when a double layer of passivated silicon atoms are used. The results are identical when one layer of passivated silicon atoms is used (not shown). This is due to the low potentials shown by the isolated silicon layers, thus the effect on the molecular gate is minimum.

Fig. 28 shows the MEPs when one input is positive and the other negative (01). The isolated molecule yields a well-defined positive potential at the output; however, when two sheets of graphene are used, the molecule yields a negative potential due to the strong negative potential of the graphene layers able to shift the positive values to the negative side. The silicon substrate does not affect strongly the molecular potentials at the output site; practically, the potential distribution is very similar to the one produce by the isolated molecule.

Fig. 26 to Fig. 29 show several of the results of this work; a complete summary is given in Table 6. The so called truth tables define the operation of each gate.

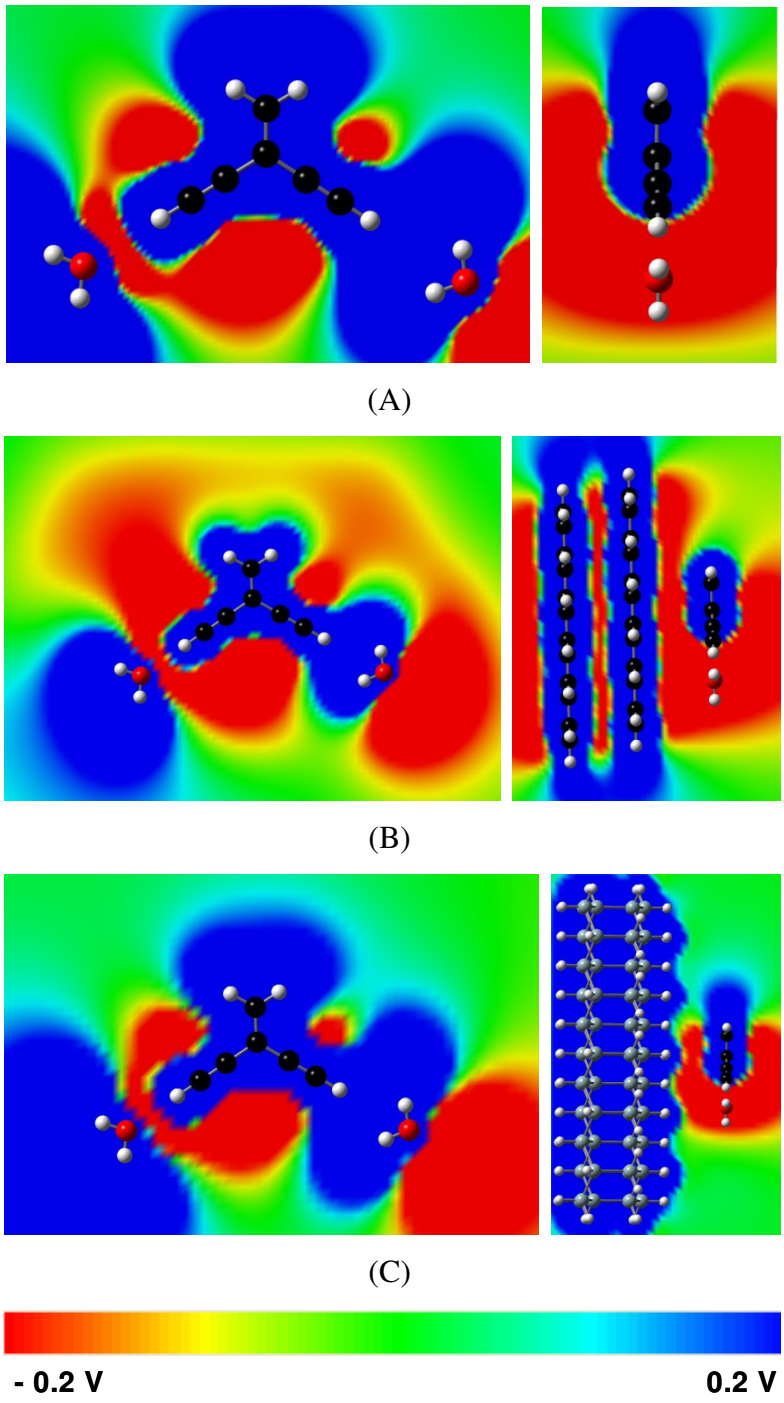

Fig. 28. Molecular electrostatic potentials for (A) the isolated molecular gate in vacuum and over substrates of (B) graphite, and (C) H-passivated silicon when one input is negative and the other is positive.

Finally, Fig. 29 shows the case when the two inputs are positive (11). The isolated molecule and the molecule with the two substrates yield a positive potential at the output site. Graphite is the most difficult as the graphene layer tends to shift potentials to negative values.

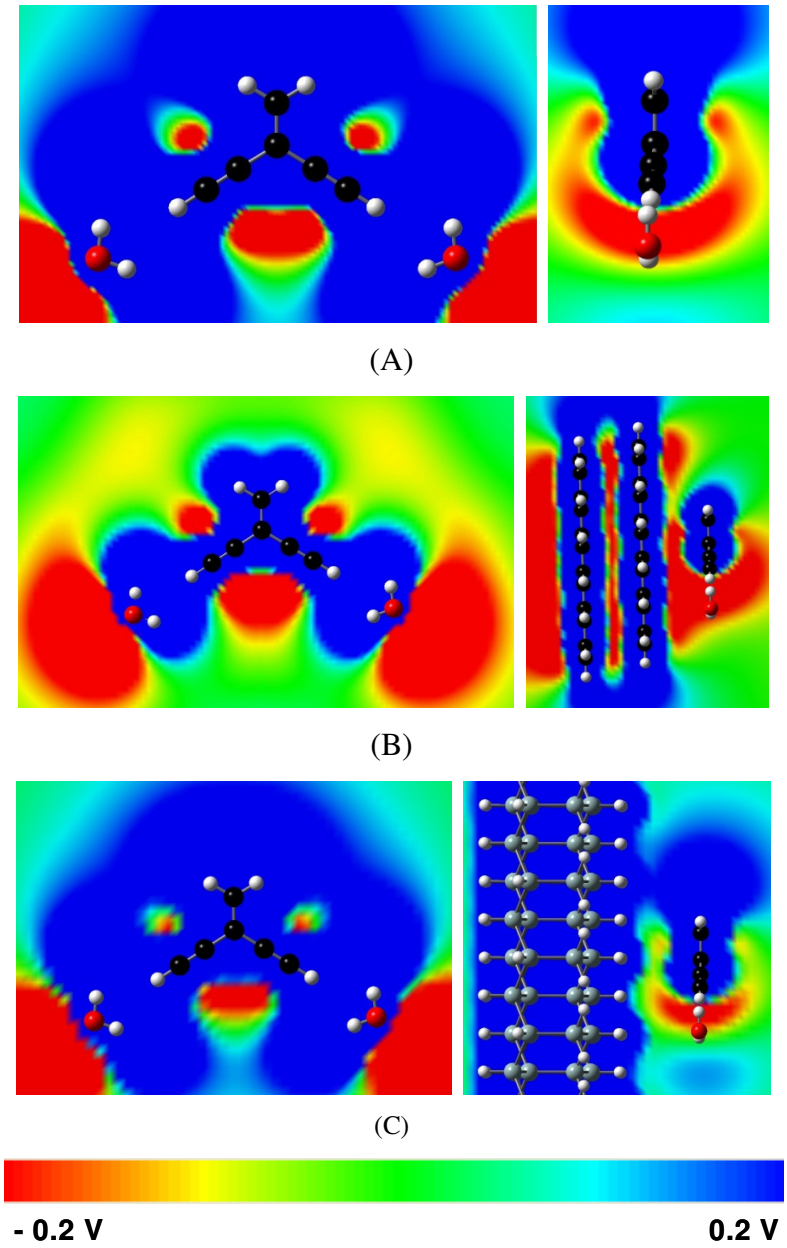

Fig. 29. Molecular electrostatic potentials for (A) the isolated molecular gate in vacuum and over substrates of (B) graphite, and (C) hydrogen-passivated silicon when the two inputs to the gate are positive.

Table 6. Truth table for the MEP OR-gate with and without substrates.

Input potentials	Logical Input	Isolated	one sheet grapheme	two sheets graphene	one sheet of silicon	two sheets of silicon
– –	0 0	0	0	0	0	0
– +	0 1	1	1	0	1	1
+ –	1 0	1	1	0	1	1
+ +	1 1	1	1	1	1	1
Gate		OR	AND	AND	OR	OR

5.1.2 Conclusions

We demonstrate that molecular gates using molecular electrostatic potentials can be used on hydrogen-passivated silicon substrates without any disturbance of the behavior that the molecular gate had in vacuum; however, the use of graphite as a substrate strongly affects such behavior. As expected, the substrate become one more design variable if strongly affects the potentials on its surface. The ability to have several substrate alternatives is very important for the practical implementation of the molecular potentials scenario. In general, the effect of the substrate can be determined by calculating the MEP of a surface as this indicates how strongly its intrinsic potential may affect the molecular device.

5.2 Nano-micro Interface to Read Molecular Potentials

There are two general approaches for the use of a single molecule to perform computation (*186*) and other so called electronic functions (*4, 187*). One is to continue the standard current-voltage approach: simply introduce molecules to continue the successful scaling-down of electronic devices based on silicon to sizes that still allows fabricating them and interconnecting them in a small integrated circuit (*15, 186, 188-192*). The second approach involves using other alternatives to encode and transport information (*185, 193*). One of the attractive approaches involves the concurrent use of molecular potentials and vibronics to perform logic, computation processing, and several other functions now performed by standard complementary metal-oxide semiconductor (CMOS) integrated circuits (*194, 195*).

However, no matter the approach to be adopted in the future, there is one important issue that is common to both major scenarios for nano and molecular electronics: the nano-micro interface. As the nano and molecular world cannot be directly addressed presently, any data or signal extraction of the nano-micro interface has to be done by using the standard CMOS technology.

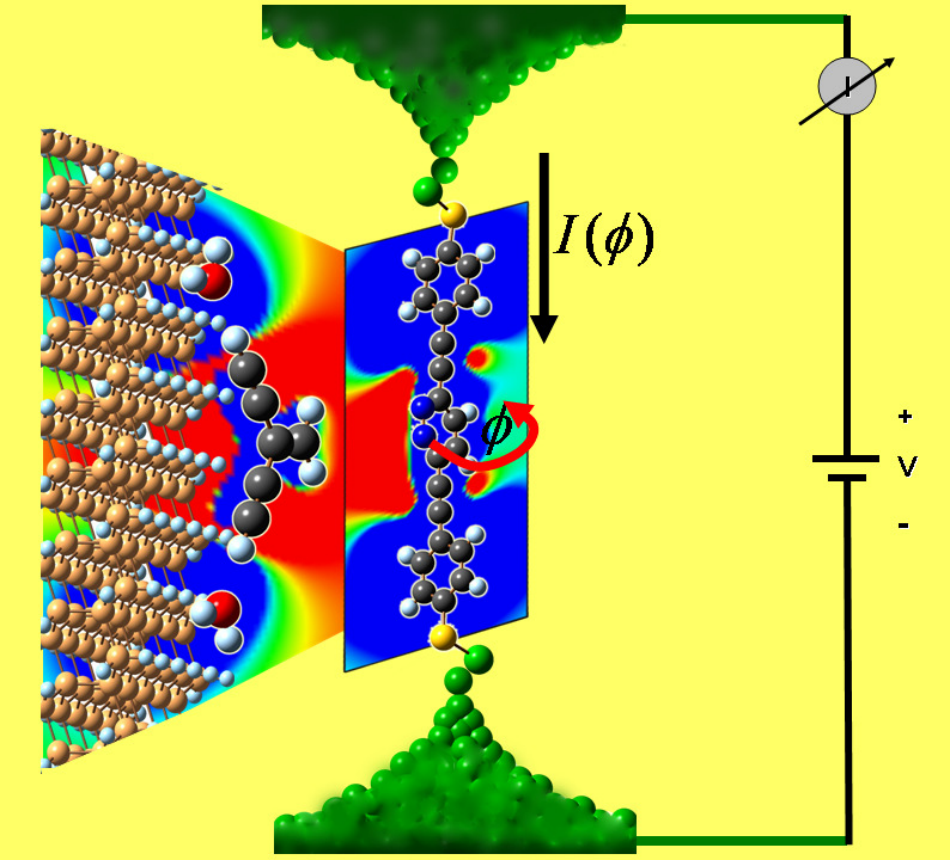

Fig. 30. Proposed nano-micro interface to read signals from molecular circuits operation using molecular potentials. Variations of the MEP are able to slightly rotate the central ring by an angle ϕ of the aza-OPE molecule, this in turn varies the current $I(\phi)$ through the external circuit.

The introduction of data is not as difficult as the extraction, as the latter requires amplification of signals from individual molecules. A few years ago, the idea of a molecular amplifier was introduced (*187, 196*). In this amplifier (Fig. 30), the rotation of a ring in a dithiotolane molecule was used to control the current through the molecule.

The rotation of one of the phenyl rings was able to increase the current through the molecule more than 60 times for the planar conformation over the perpendicular conformation and much more still for larger voltages. Although the calculations were performed using a simple molecule of the oligo phenylene–ethynylene (OPE) family, whereby the rotation of one ring was constrained, turning the control ring exclusively requires further analysis.

A modified OPE molecule that contains a local dipole moment in the central ring is implemented. Thus, two of the central carbon atoms are changed by adding polar substituents such as nitrogen, yielding the aza-OPE molecule (Fig. 31). Thus, the molecule can be rotated by the effect of an external electric field. The effects of this rotation, and the changes in the molecular potential it produces, are tested. With the aza-OPE connected externally to a power source and to standard electronic amplifiers, it was discovered that the results can be used to design a specific amplifiers able to transform a small signal interacting with the dipole moment of the rings to a much larger signal through the aza-OPE, as shown in Fig. 30.

5.2.1 Methodology

An OR logical gate with two ethynyl groups is used (Fig. 24) to model the circuit from where the signal is read. The input potentials are applied to the ethynyl groups, and the output signal is taken outside the ethylene hydrogen. The input the may be triggered through metallic electrodes, for example using an external electric field of an ultra-fast laser, or by using other molecules bearing a dipole, or simply by the output of other MEP devices (*185*). This approach considers that the molecular gate is in vacuum. The substrate, certainly represents another design variable because the potential of the substrate may or may not affect the behavior of the molecular gate as already established in the literature (*197*).

Due to the symmetry of the device the vector input 01 yields identical result than the vector input 10, which is also the case in practical gates used in present CMOS technology.

How does one read signals from molecules? We use a specific molecule with the properties necessary to act as an amplifier, i.e., able to interact with the device and simultaneously be externally connected to a power source that transforms small signals to much larger signals. The pyridazine, 3,6-bis(phenylethynyl) (aza-OPE) molecule (Fig. 31) is chosen as the amplifier. Its electronic structure, properties, and response for a device are calculated and determine terminating the molecule in a hydrogen, HS, and SAu.

The amplifier and the gate are optimized using the Becke three-parameter hybrid exchange functional with Perdew-Wang correlation functional (B3PW91) (*23, 24, 198*). The 6-31G(d, p) (*199*) basis set is used for the H, C, N, S and O atoms. For the gold atoms, LANL2DZ basis sets and effective core potentials are used (*20, 21, 200*). Calculations are performed using the Gaussian 03 program (*201*).

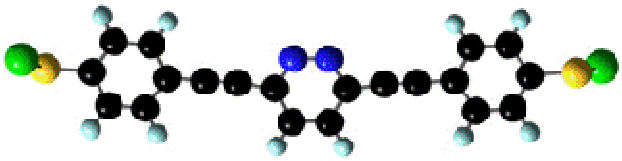

Fig. 31. Molecular amplifier molecule. Pyridazine, 3,6-bis(phenylethynyl), aza-OPE for short, with AuS terminals. Carbon (black), sulfur (yellow), gold (green) and hydrogen (white).

5.2.2 Results and Discussion

The relative and total energies for the aza-OPE molecule are shown in the Table 7. A small amount of energy, 2.6 kcal/mol, is required to rotate the central ring 90 degrees; hopefully only small rotations requiring only fractions of kcal/mol would be needed in order to discriminate logical levels. It is also observed that the highest occupied molecular orbital-lowest unoccupied molecular orbital (HOMO-LUMO) gap or HLG increases in 0.34 eV, which yields a decreasing of conductivity.

Table 7. Energies, relative energies, dipole, and HOMO and LUMO energies for the plain, aza-OPE–AuS.

Angle (°)	Energy (Ha)	Relative Energy (kcal/mol)	Dipole Moment (Debye)	HOMO (eV)	LUMO (eV)	
0	-1944.46131	0.00	3.46	-6.10	-3.56	opt
15	-1944.46099	0.20	3.48	-6.10	-3.56	sp
30	-1944.46003	0.81	3.55	-6.15	-3.54	sp
45	-1944.45792	2.13	3.91	-6.20	-3.54	sp
60	-1944.45765	2.30	3.94	-6.29	-3.54	sp
75	-1944.45729	2.53	3.97	-6.37	-3.51	sp
90	-1944.45714	2.62	3.98	-6.39	-3.51	opt

Isolated current voltage curves are for the aza-OPE molecule shown in Fig. 32. The central ring of the molecule is rotated at 15 degree intervals from 0 to 90 degrees. The calculations from 90 to 180 degrees are omitted since they yield the same results as for 0 to 90 degrees (e.g. the results for 105 degrees equal to the results for 75 degrees). The most interesting result is that the current decreases in a distinguishable as the central ring is rotated.

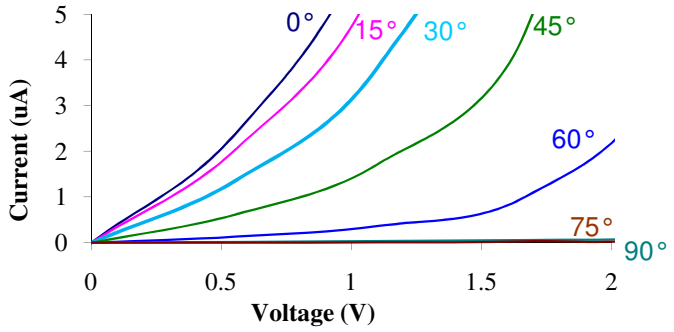

Fig. 32. Current-voltage curves for the aza-OPE molecule at several torsional angles of the central ring with respect to the other two coplanar ones.

The MEP behavior for this molecule is also calculated as the central ring is being rotated. Fig. 33 shows how the negative potential in the plane of the molecule (red region) disappears when the central ring is rotated.

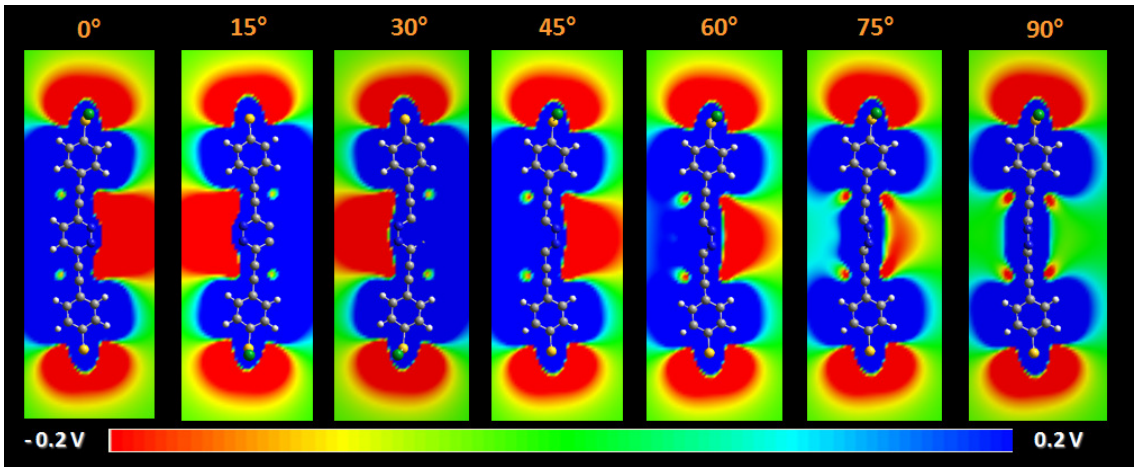

(A)

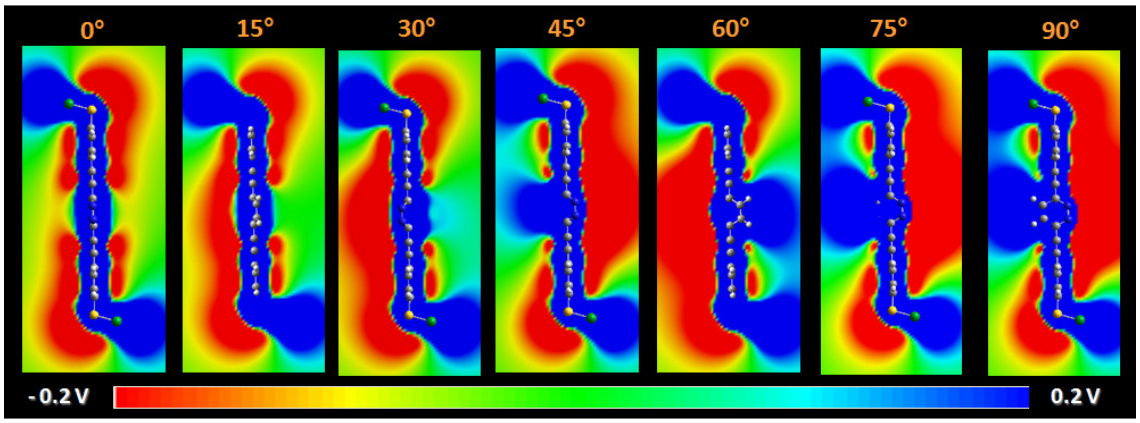

(B)

Fig. 33. MEP for the aza-OPE molecule rotating its central ring from 0 (coplanar) to 90 degrees (perpendicular). (A) Front view; (B) Side view.

The high conductance of the coplanar conformation is explained in Fig. 34; the coplanar conformation is fully delocalized and becomes more localized when the central ring is rotated. No sharp changes are observed indicating that the change in current also follows a steady behavior as the angle is changed.

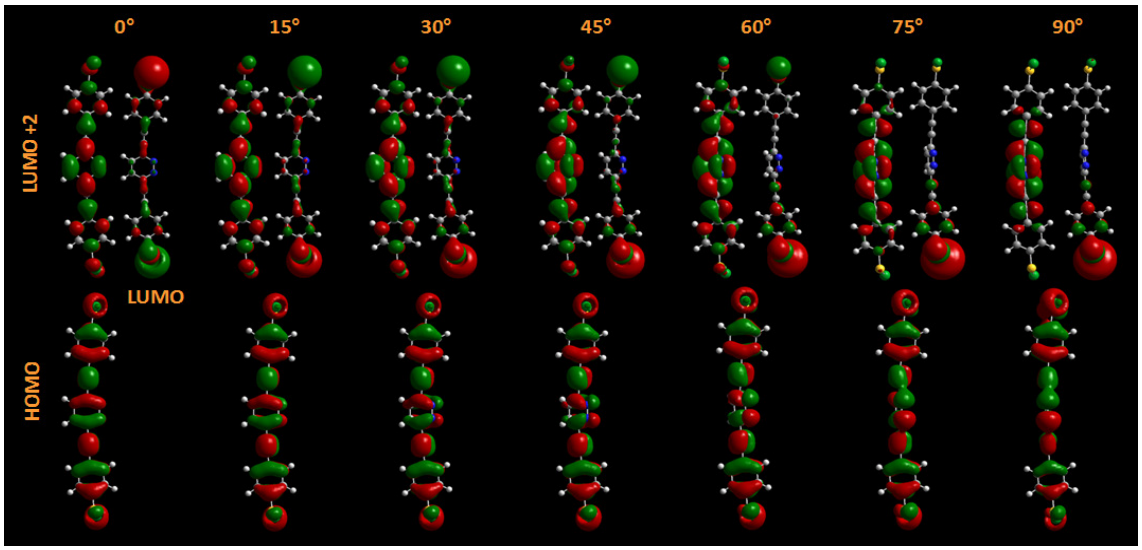

Fig. 34. Molecular orbitals for the aza-OPE molecule when its central ring is rotated from 0 (coplanar) to 90 (perpendicular) degrees. A bigger delocalization is shown in the LUMO+2 than in the LUMO. As the rotation angle increases, both LUMO and LUMO+2 become more localized, while the HOMO does not show an appreciable change.

The device is then assembled at two different distances from the output to the nitrogen atoms in the central ring of the molecule aza-OPE (used as amplifier) as is shown in Fig. 30. Each different combination of inputs is tested at both distances with the results summarized in Table 8. In this case, because of the symmetry, the negative, positive input or 01 vector has the same result as the positive-negative or 1 0 input vector. Starting with different angles of the central ring we get two different sets of optimization angles. One set is just 0 and the other set of angles changes depending on the output and the distance between the output and the nitrogen atoms. The energies for these optimizations with their corresponding inputs, angles, and distances are shown in Table 8.

Table 8. Optimization angles, relative and total energy for each system at two different distances when the inputs are applied.

Input potentials	Device Logical Input	Device Logical Output	Distance (Å)	Started angle	Deflected angle	Energy (Ha)	Relative Energy (kcal/mol)
– –	0 0	0	2	0.0	0.0	-2327.99032	7.85
– +	0 1	1	2	0.0	0.0	-2327.98697	9.95
+ +	1 1	1	2	0.0	0.0	-2327.98269	12.64
– –	0 0	0	2	140.0	55.8	-2327.99707	3.61
– +	0 1	1	2	140.0	54.7	-2327.99228	6.62
+ +	1 1	1	2	140.0	49.7	-2327.98696	9.96
– –	0 0	0	3	0.0	0.0	-2328.00283	0.00
– +	0 1	1	3	0.0	0.0	-2327.99867	2.61
+ +	1 1	1	3	0.0	0.0	-2327.99362	5.78
– –	0 0	0	3	140.0	143.0	-2327.99962	2.02
– +	0 1	1	3	140.0	140.0	-2327.99334	5.95
+ +	1 1	1	3	140.0	136.7	-2327.98642	10.3

The more negative the output, the bigger the optimized angle and the lower the energy. In general, the lowest value of energy corresponds to the cases when the distance is 3 Å, and the highest energies occur when the logical device is closer to the molecule, at 2 Å and 0º. Current voltage characteristic calculated for each case are graphed in Fig. 35. For all cases, the highest values of currents through the aza-OPE occur at 3 Å and 0°, separation and torsional, respectively, followed by 2 Å and 0 degrees. The fact that we get different currents for the same angle is an indication of a field or potential effect in the central ring able to control the current through the molecule. For the non-zero optimized angles, the current is lower. This is particularly true for the cases with the negative input and the larger separation of 3 Å, and with an optimization angle of 143 degrees. The current is distinguishable and the energy needed considerably low.

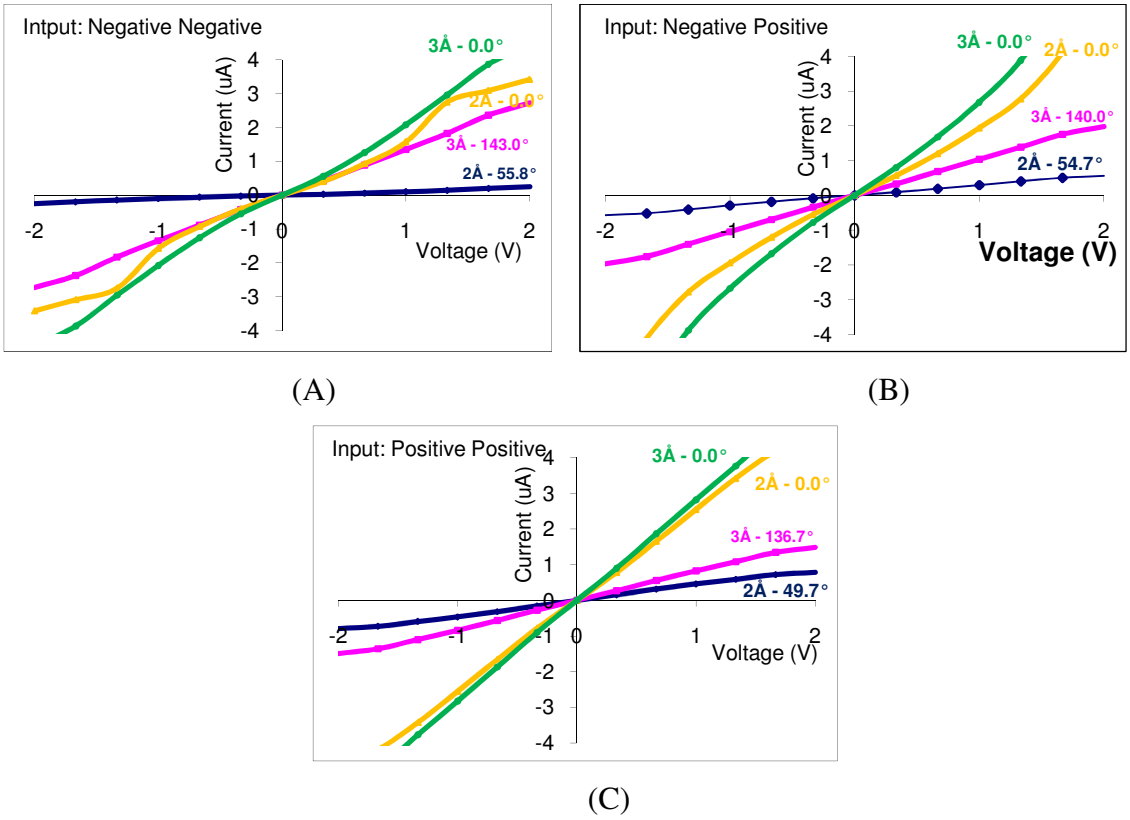

Fig. 35. Current-voltage curves for each logic input combination. (A) Input 00, (B) Input 01 and 10, (C) Input 11.

Table 9 shows the truth table of the logical molecular gates and the possible conversion to current at the molecular amplified using threshold values of 1 and 2 V to discriminate between a logical zero and one. To describe the signals using the current flowing through the aza-OPE molecule, the current at these two different voltages are used as outputs. For every case studied, the response obtained by the amplifier also corresponds to an OR gate.

Table 9. Logical gates truth tables (three first columns) and response of the amplifier at a distance *d* from the gate to the aza-OPE nearest point. For each distance *d*, two initial angles are tabulated (0 AND 140); however, other initial neighbor angles were used yielding the same optimized angle. The output currents are calculated at two bias potentials 1 and 2 V and for each case, a suitable threshold is used and shown at the last row of each truth table where also the type of gate is reported according to the amplified signal (current) levels.

Device Input Potentials	Device Logical Inputs	Device Logical Output	*d* (Å), initial angle (˚)	Optimized angle (˚)	Output current at 1 V (μA)	Output current at 2 V (μA)	Amplifier logical output at 1V	Amplifier logical Output at 2V
– –	0 0	0	2, 0	0.0	1.57	3.42	0	0
– +	0 1	1	2, 0	0.0	1.94	5.93	1	1
+ +	1 1	1	2, 0	0.0	2.55	4.53	1	1
		OR			1.70	5.50	OR	OR
– –	0 0	0	2, 140	55.8	0.10	0.25	0	0
– +	0 1	1	2, 140	54.7	0.30	0.56	1	1
+ +	1 1	1	2, 140	49.7	0.46	0.79	1	1
Thres/gate		OR			0.20	0.40	OR	OR
– –	0 0	0	3, 0	0.0	2.08	4.47	0	0
– +	0 1	1	3, 0	0.0	2.68	9.52	1	1
+ +	1 1	1	3, 0	0.0	2.82	5.20	1	1
Thres/gate		OR			2.60	5.00	OR	OR
– –	0 0	0	3, 140	143.0	1.35	2.72	1	1
– +	0 1	1	3, 140	140.0	1.04	1.98	0	0
+ +	1 1	1	3, 140	136.7	0.83	1.49	0	0
Thres/gate		OR			1.20	2.00	NOR	NOR

The molecular electrostatic potentials as the central ring rotates from 0 (coplanar) to 90 (perpendicular) to 180 (coplanar) are shown in Fig. 36 for the three distinguishable combinations of inputs. Notice that as the atoms of the central ring get inside the plane of the other two rings are not visible due to the opaque picture representing the MEPs on the surface of the other two rings.

We find a very interesting and unexpected finding: for cases when there is no rotation of the central rings, still the current through the molecule is different because of the different molecular potential applied to the aza-OPE molecule. Thus we conclude

that the effect of the molecular potential is reminiscent of the effect of a bias gate potential in a field effect transistor.

The weak MEP potentials are able to modulate the current through the aza-OPE molecule, providing in addition a possibility to have an analog device. The current increases as the applied potential from the molecular gate increases as indicated in the first truth table from Table 9. This creates the possibility of having transistor channels of just 1 or 2 nm long that are able to be controlled by molecular potentials thus yielding the important ingredients for the next generation of molecular devices that are compatible with present silicon microelectronics.

As indicated in Table 9, the important angles correspond to 0, ~60 and ~150 degrees but all of them yield similar results. This fact has also strong importance in the development of molecular circuits as the actual resting position of the central ring with respect to the other two, in most cases, would be unknown. Certainly, this molecular system is just presented as proof-of-concept system rather than as a proposal for the final design.

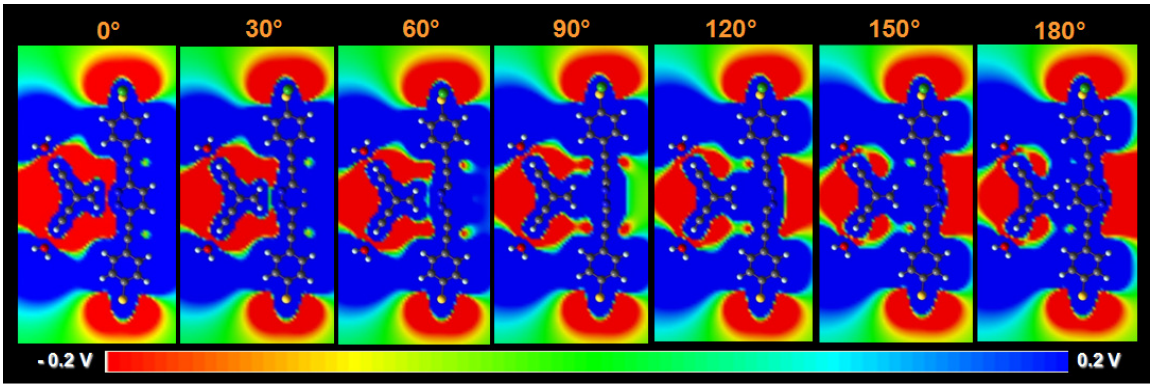

(A)

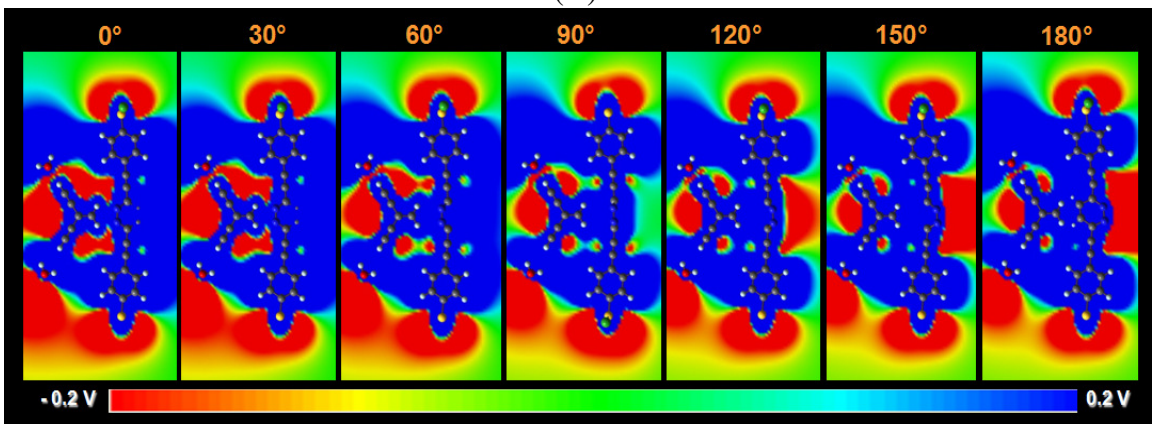

(B)

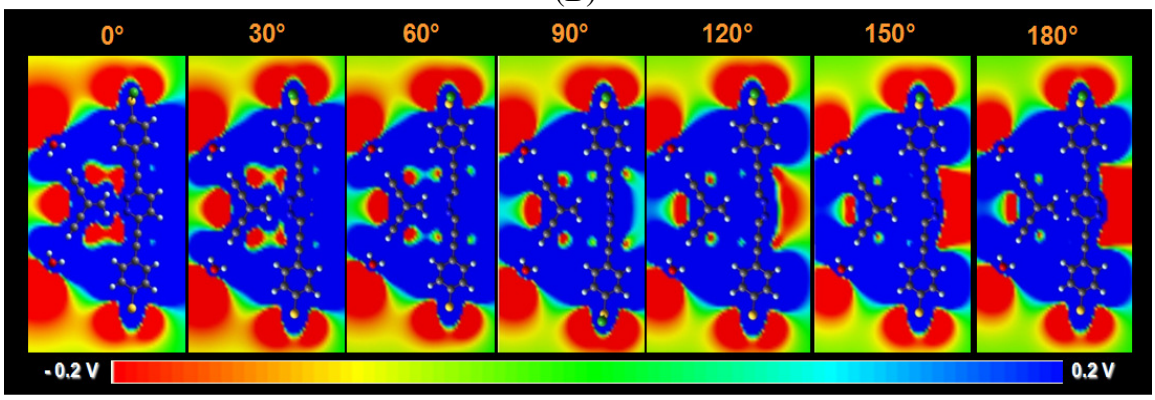

(C)

Fig. 36. MEP for the aza-OPE molecule when the device is at 2 Å from the central ring and the central ring is rotated from 0 to 180 degrees when inputs are (A) 00, (B) 01 and (C) 11.

Strong coordination/collaboration with the chemical synthesis is paramount for the successful implementation of molecular electronics.

5.2.3 Conclusions

The aza-OPE molecule has the necessary properties to act as an amplifier such as large discrimination for different torsional angles. However, this is not only limited to actually get a current due to the rotation of the angle but also due to just the value of the molecular potential, which strongly affect the current through the molecule even if the torsional angle has slightly or not changed.

Our setting can read molecular potentials from molecular devices and convert (amplify in terms of power) their signal to be compatible with the standard microelectronics. Thus, the molecular potential gates attached to the interface amplifier can be also be used as sensors with built-in logic for molecular discrimination purposes. The output current through the aza-OPE molecule is the amplified signal from a chain of logical gates representing the results of specific logical functions.

5.3 Graphene MEP Amplifier

The delocalized electronic density of graphene is highly sensitive to moieties adsorbed on the surface, using the vibronics scenario graphene sensors (*40*) and transducers (*41*) have been previously shown.

It has been demonstrated that information can be coded and process using molecular electrostatic potentials, then we would like to amplify this signals to be readable in the conventional microelectronics.

This work is a theory-experiment approach; we attempt to develop a graphene-based sensor of MEPs from molecules in the neighborhood of the graphene surface.

5.3.1 Theoretical Approach

We propose to use graphene as a sensor of molecular electrostatic potentials; we design a graphene sensor device able to detect negative or positive molecular electrostatic potentials with signal amplification suitable for conventional microelectronics. The amplification is obtained from calculations of the changes in the

current values due to applied potentials along graphene ribbons. The source of electrostatic potential is obtained from self-assembled monolayers of molecules featuring positive or negative potentials at their ends (depending of their functional groups).

Then we carried out accurate computational chemistry techniques, ab-initio calculations and our GENIP program to calculate the conductivity along a graphene ribbon when molecules with a strong dipole moment and either negative or positive molecular electrostatic potential are interacting in the two neighborhood sides of the graphene surface as is shown in Fig. 37.

Changes in the current-voltage characteristics calculated longitudinally on the graphene ribbon show the effect of the MEP on the electron transport when a negative potential is applied using the molecules on the surface, the conductivity of the graphene ribbon increases; at the same time when a positive potential is applied the conductivity of the ribbon decreases and when the ribbon is polarized by applying a negative potential at the left of the ribbon and a positive potential at the right side a diode-like behavior is shown in the conductivity calculations. These results suggest a strong sensitivity of the graphene ribbons under the presence of a molecular electrostatic potential absorbed on the surface.

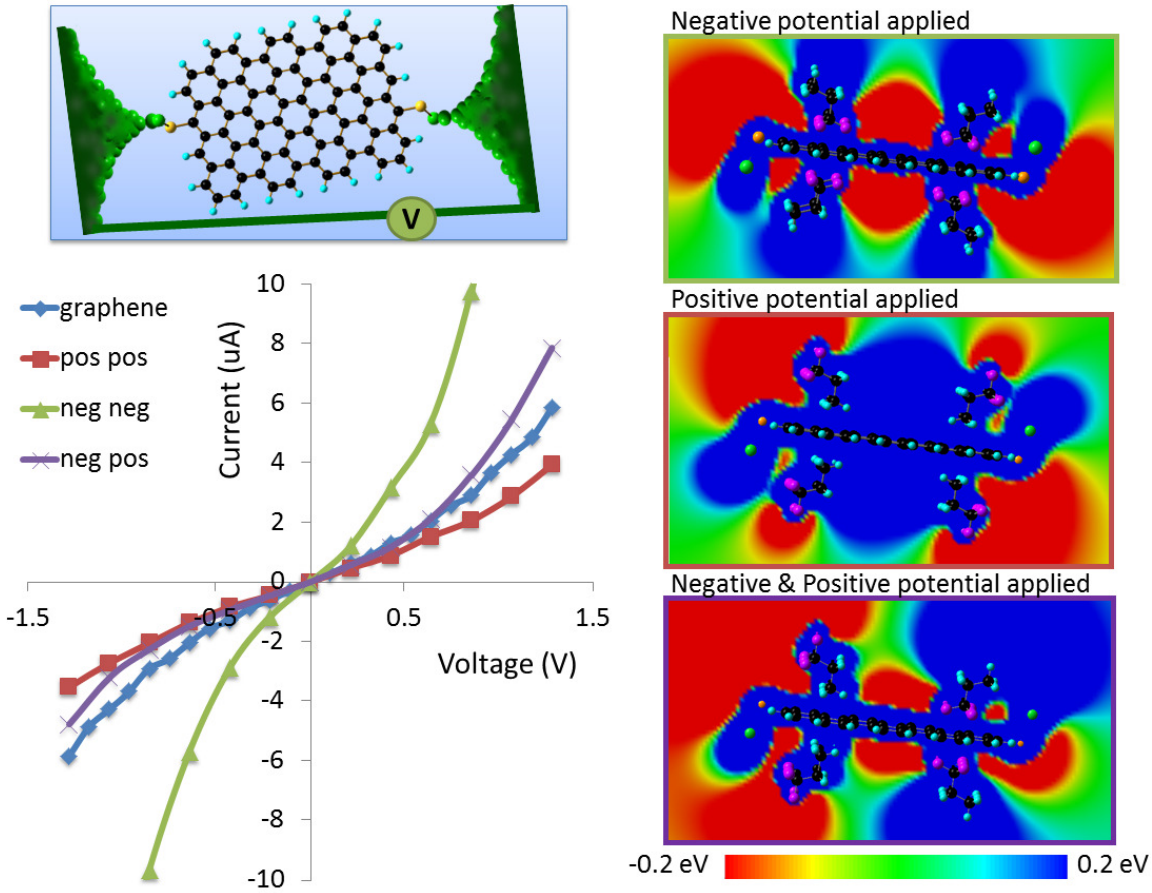

Fig. 37. Graphene amplifier of molecular electrostatic potentials. Current response when a self-assembled monolayers of molecules with a high dipole are adsorbed on both surfaces of the graphene layer. Three different configurations are used: only negative potential applied, only positive potential and half positive and half negative potential applied creating a diode-like polarization on the graphene ribbon.

5.3.2 Experimental Approach

We perform a preliminary proof of concept experiment of the sensitivity of graphene to external changes. We placed a graphene sample suspended between two metal electrodes, also, between the two electrodes and under the suspended graphene there is a third metal electrode which we use as a gate electrode (Fig. 38).

When we applied a sweep voltage through the graphene from source to drain we obtained the current voltage characteristics shown in pink, at this point there is not gate voltage applied, however as soon as a gate voltage is turned on the conductivity of the ribbon changes dramatically. We tried this for different gate voltages and with these

results we expect to find the same sensitivity of graphene when instead of the gate voltage a self-assembly of molecules applies the field.

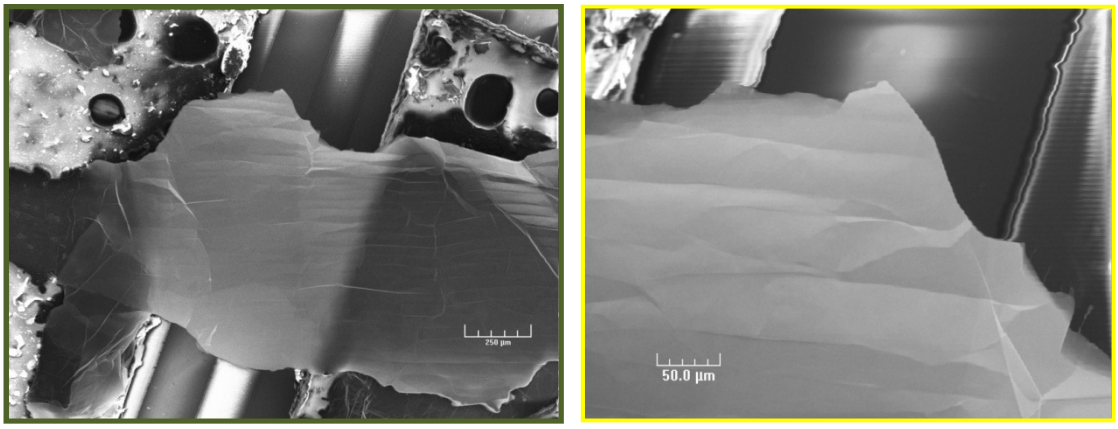

(A) (B)

Fig. 38. (A) **Fabricated device. (B) Close view of the graphite layer edges, and of several graphene layers.**

Two pieces of copper are used as electrodes for the electrical measurements, and are placed over photolithographic fabricated copper metal lines. Using the scotch tape method a thin layer of graphite is placed between them as shown in Fig. 38. The copper metal line is isolated below the graphene sample and is used as gate. The source and probe tips are placed on the graphite layer as is shown in the diagram (Fig. 39B).

The results show that graphene is very sensitive to the electric field created by applied electrical potential, and thus suggest a potential application of graphene as a sensor of molecular electrostatic potentials in which the source of electrostatic potential is obtained from self-assembled monolayers of molecules featuring positive or negative potentials at their ends (depending of their functional groups).

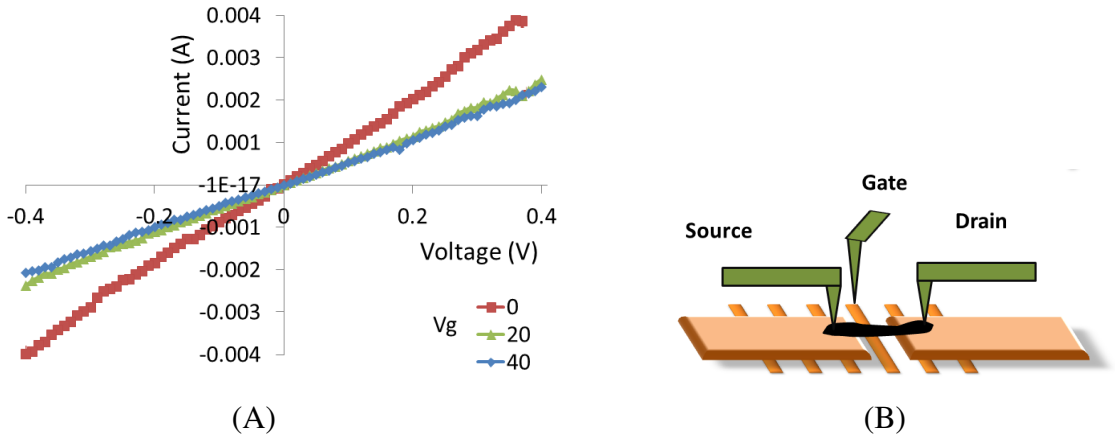

Fig. 39. (A) Experimental results of the current-voltage characteristics when gate voltages of 20 and 40 V are applied. (B) Diagram of the fabricated device.

5.3.3 Conclusions

Graphene surface sensitivity to a negative or positive electrostatic potential on the near neighborhood has been shown using ab-initio calculations and Green function theory. Calculations shown that signals processed at the molecular level using MEPs can be amplified using graphene ribbons through changes in the conductivity of the graphene ribbons. Experimentally we have shown that an electric field is digitally detected and amplified by graphene ribbons through changes in the conductivity.

CHAPTER VI
COMMUNICATION BETWEEN MOLECULAR SCENARIOS*

Within the margins of what is allowed by quantum mechanical rules, the ability to read small perturbations of molecules, such as vibrations or molecular potentials, is a key point to implement the use of molecules as sophisticated molecular/electronic devices. Vibronics, along with the capability of molecular potentials to encode information, are the two key scenarios for a new era of electronics (*4, 202*). However, amplifiers and transducers of signals for these two scenarios are required to detect, transport, and encode information at the molecular level, and to reach the delivery of this technology. We are proposing graphene molecules used as terahertz generators (*19*) as the base molecules to elaborate the reading/writing of information at the molecular level thanks to its atomic thickness. Graphene systems are considered the perfect materials to serve as interfaces between molecular/nano electronics and current silicon electronics.

In this chapter, we achieve communication between MEPs, vibronics and current-voltage characteristics by using the sensitive surface of graphene ribbons and a water molecule as a simple example. The molecular potential of a molecule is affected by the vibrational movement of atoms and the changes are then amplified through changes in the current-voltage characteristics.

6.1 Single Molecule Detection Using Graphene Electrodes

It is shown, using density functional theory that the trapping of molecules between graphene electrode plates can be used to sense molecules through their vibrational fluctuations. This hypothesis is tested using water trapped on two graphene molecules connected to a potential difference. The electric current fluctuations generated through the junction correspond to the fluctuations of the vibrational modes.

---

* Parts of this chapter are reprinted with permission from Single molecule detection using graphene electrodes, by N. L. Rangel and J. M. Seminario, 2010. *J. Phys. B*, **43**, 155101. Copyright 2010 by IOP Publishing.

Since this system yield currents in a range workable by present electronic devices, the need of further "molecular amplification" is not required. Fluctuations of the three modes of water yield similar changes of potentials in the neighborhood accessible by other molecules; therefore, vibrations from a single water molecule, as an example, or vibrations from any other molecule can be transduced into electrical currents of magnitude compatible with present silicon-technology. In the particular case of the water molecule, a rectified potential signal is obtained from the fluctuations of the antisymmetric stretching mode and a simple transduction is obtained from the symmetric stretching and bending modes. It is argued that the high sensitivity is due to the strong delocalization of the frontier molecular orbitals or molecular plasmons on graphene electrodes, which guarantees the detection based on molecular potentials or molecular vibrations; these plasmon-like molecules are of major importance for the development of molecular and nano electronics.

6.1.1 Methodology

Graphene molecules (*19*) are used as plasmonic plates connected to a power supply through gold electrodes and sulfur clips. Optimized water molecules (as a typical example of a molecule) and with different geometries that simulate the vibrational movement of atoms for each vibrational mode, are placed between the graphene plates, the different geometries yield changes in the molecular electrostatic potentials (MEP).

The level of theory used is the Becke three-parameter hybrid exchange functional with the Perdew-Wang correlation functional (B3PW91) (*203*). The 6-31G(d) (*18*) basis set is used for the H, C, S and O atoms, and the LANL2DZ basis sets and effective core potentials (*20, 21*) are used for Au atoms. Specifically, we use full optimizations with no constrains with initial geometries based on a previous reported experience (*42*), and perform calculations as described in Chapter II.

In this particular case, partially optimized or optimized separately calculations are done to graphene molecules attached to sulfur clips and with a water molecule in-between, in order to compare current responses at the same distance because a full

optimization would yield unparallel graphene plaques that would beat the comparative purpose of the calculation.

6.1.2 Results and Discussion

Molecular potential variations while the movement of atoms due to the vibrational modes of the water molecule is shown in Fig. 40.

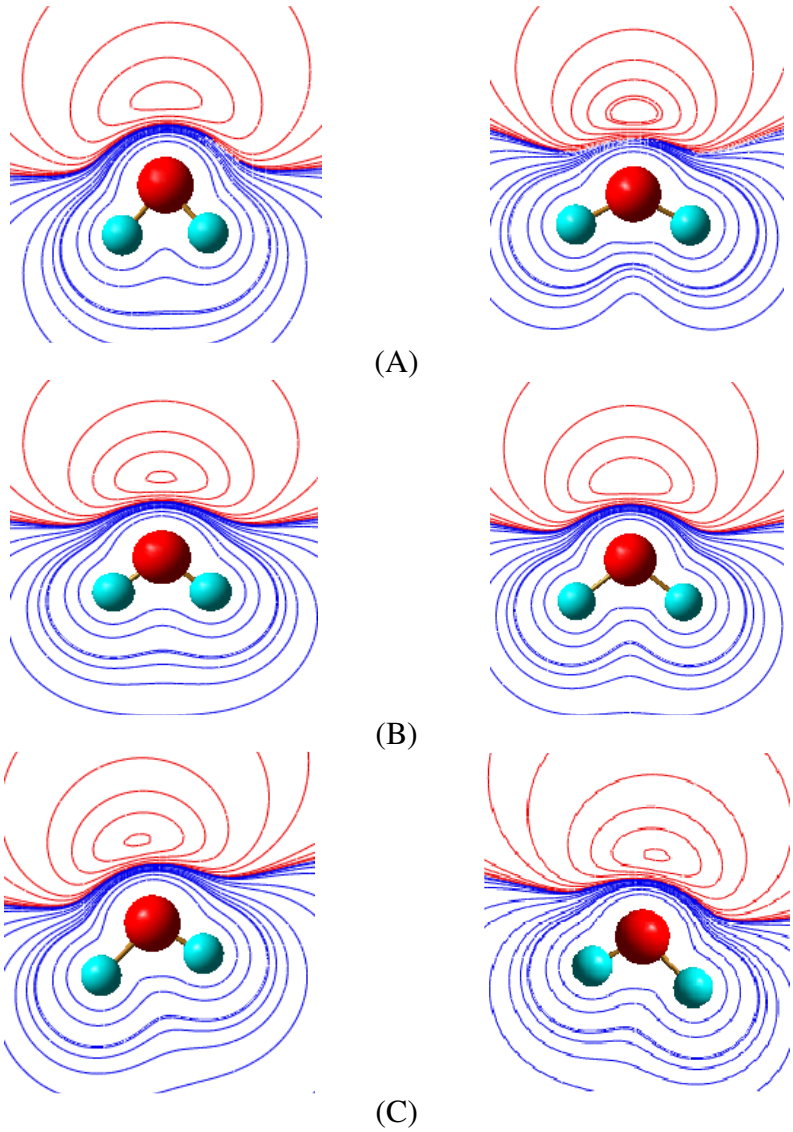

Fig. 40. Molecular electrostatic potentials of the water molecule while atom movements due to vibrational modes (A) bending, (B) stretching and (C) anti-symmetric stretching.

Molecular vibrations of the water molecule yield oscillations of the molecular potentials, which are calculated at 1.8 Å above the oxygen atom (Fig. 41A). This is a suitable distance to observe the MEPs because most of the important inter-molecular interactions take place around that distance (*172, 204*). Usually, vibrations of the agent (water in this case) are far beyond those of the detector and therefore, are not able to follow the vibrations of the agent; however, the concerted motion of delocalized electrons in the detector may allow us to follow those vibrations.

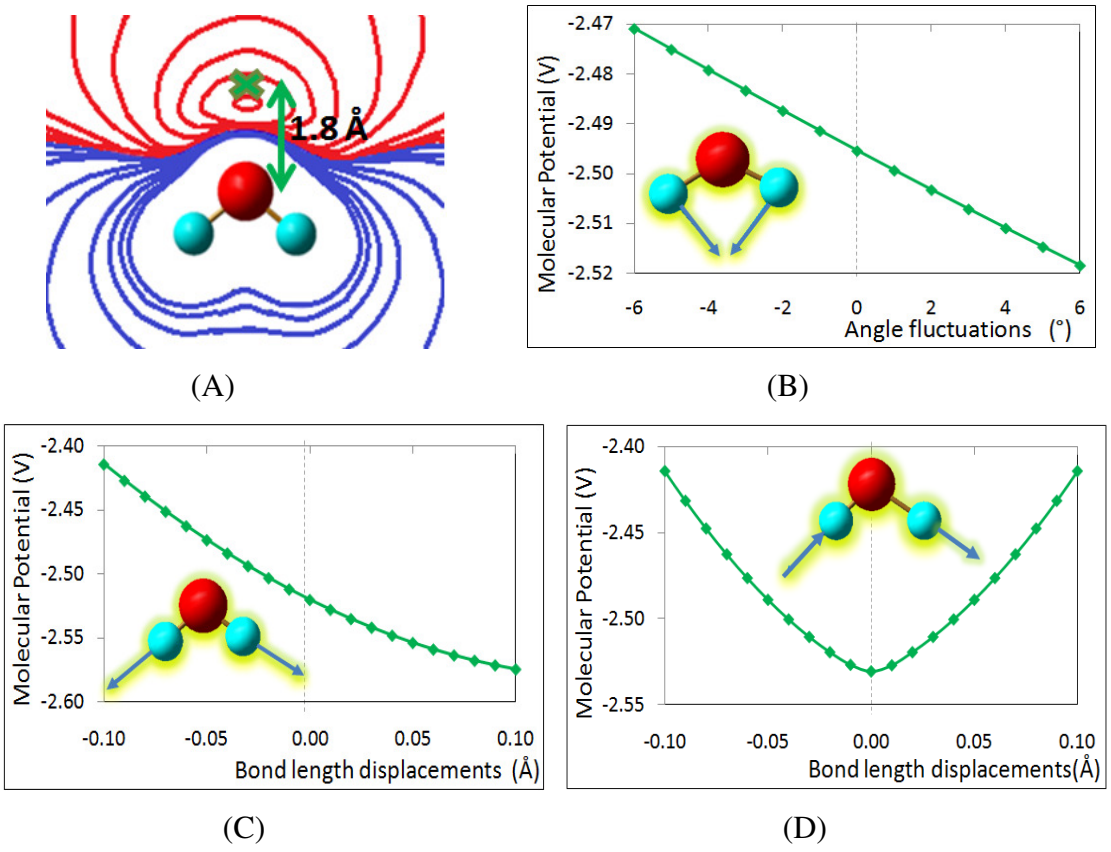

Fig. 41. (A) Molecular potential contours of the optimized water molecule in vacuum. Red lines are negative and blue lines are positive potential contours of values ranging from -2.7 to 2.7 V. All potential fluctuations of the water molecule are due to its vibrational modes and are calculated at the point × located at 1.8 Å from the oxygen atom. (B) Bending mode and (C) symmetric stretching: The MEP is linear for bending and symmetric stretching displacements; therefore, the potential (MEP) corresponds to the variations in geometry at the point x (transduction). This correspondence is highly linear for the angle fluctuations and quadratic for the bond lengths. (D) Anti-symmetric stretching mode: positive or negative displacements in either of the O-H bond lengths with respect to the equilibrium geometry yield the same value of the molecular potential, resembling the behavior of a full rectifier.

Classically, a transducer is a device able to convert energy of one type into energy of other type; for instance, a microphone converts pressure vibrations in air into an electrical current. In this case, we extend the use of the term transducer to include, for instance, changes in molecular potentials due to the vibrational movement of the atoms. When comparing the molecular potentials versus the movement of atoms due to their vibrational modes, we find that a linear relation (transduction process) takes place due to the bending mode of the water molecule (Fig. 41B). Another transduction is observed, at least for small displacements, from the antisymmetric stretching mode (Fig. 41C) and a full rectification can be observed from the symmetric stretching mode (Fig. 41D).

Therefore, changes in molecular potentials due to molecular vibrations can be transduced and amplified into current-voltage characteristics on the delocalized electronic surface of graphene molecules (*42*). A current response from each vibrational mode is obtained when a constant voltage of 0.5 V is applied through a couple of graphene plates as shown in Fig. 42. These changes in the molecular geometry due to vibrational modes produce current fluctuations in the two-layer graphene junction.

The presence of a molecule between the graphene plates (sensor) produces changes in the current response, due to perturbations of the fully delocalized electronic density of graphene molecules (plasmons) which is sensitive to not only the trapped molecule (probe) but also to changes in the molecular electrostatic potentials due to the movement of the atoms. The contribution of the electrons can be either constructive or destructive to the conductivity, producing changes in the current response for each change in the molecular electrostatic potentials.

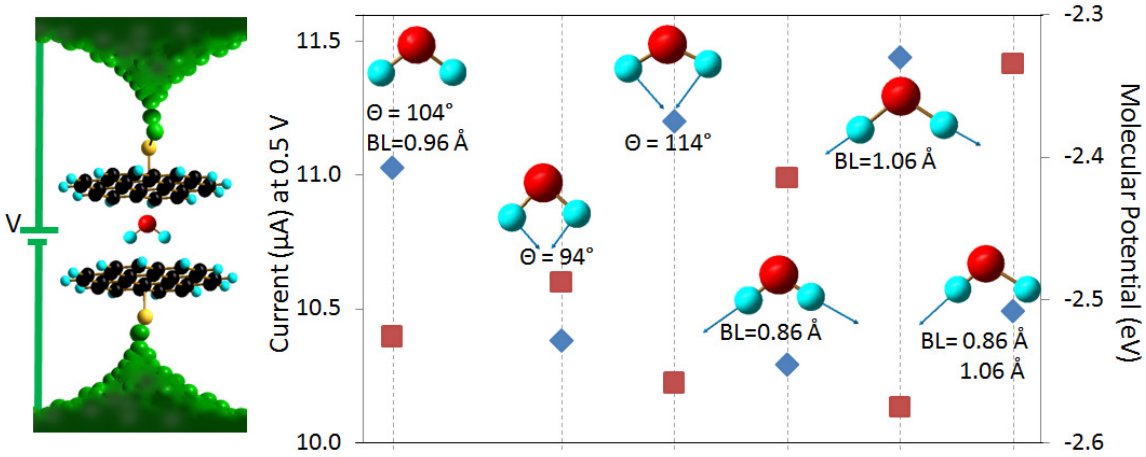

Fig. 42. Current response when a bias of 0.5 V is applied through two graphene ribbons acting as electrode plates and a water molecule (with several geometries associated to their vibrational modes) is placed in between the plates. From left to right the optimized geometry is shown (HOH angle 104° and OH bond lengths of 0.96 Å) followed by variations of this geometry due to the normal vibrational modes. For each geometry, the bond length and angle fluctuations affect the molecular potentials (squares and right vertical axis) and are detected through their effects on the current (diamonds and left vertical axis) across the junction.

If instead of the water molecule, another graphene molecule is placed in-between the junction, i.e., having now a junction of three graphene molecules, the current-voltage characteristics can be compared to the empty two-graphene junction characteristics (Fig. 43). The optimized triple layer graphene distances of 3.26 and 3.44 Å are found and we start the optimization with the layers at the same distance of 3.47 Å, which is slightly longer (0.02 Å) than the optimized bilayer and no imaginary frequencies are found indicating that the 3-layers graphene is a local minimum. As Fig. 42 shows how vibrational modes can be detected using graphene plates, Fig. 43 shows the effect of the external voltage on the current (Fig. 43A and Fig. 43B) through the graphene plates when nothing (Fig. 43C) and when another graphene molecule (Fig. 43D) is placed in between of the graphene plates.

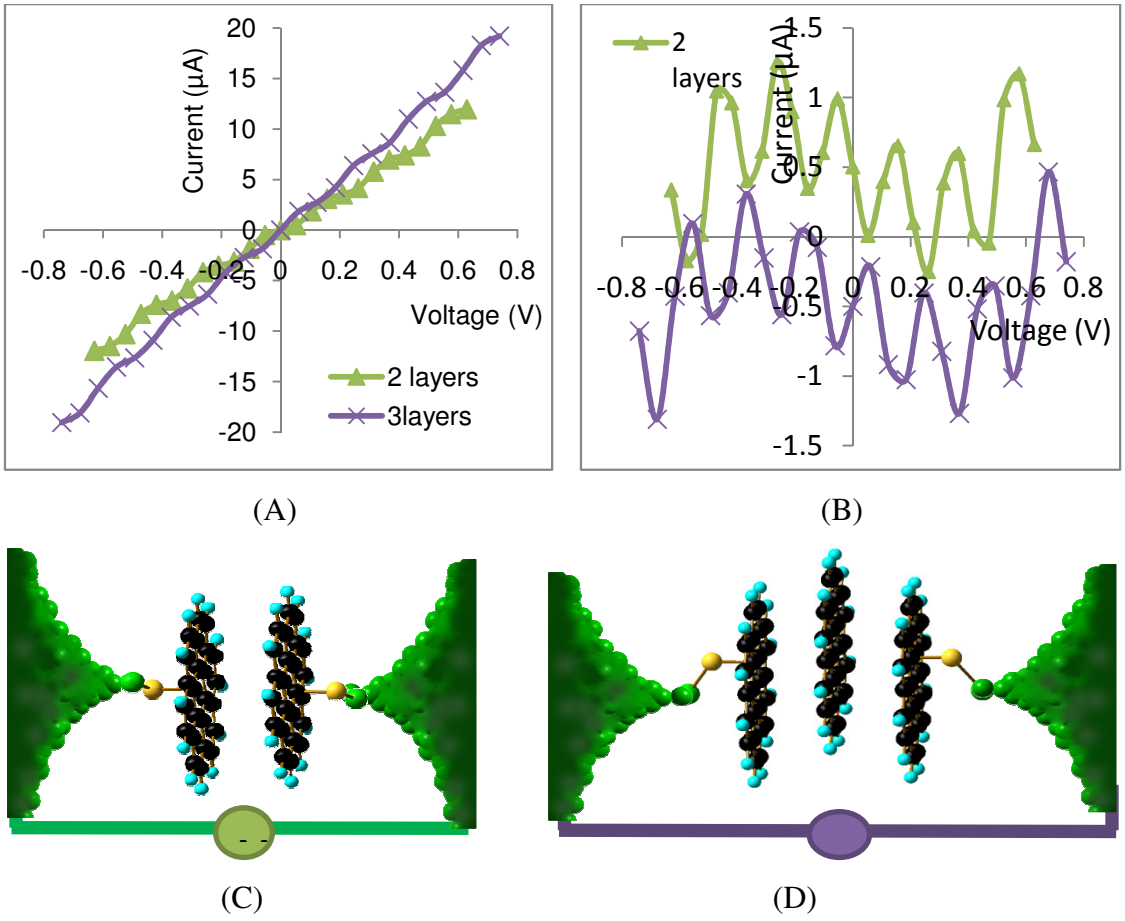

Fig. 43. Current-voltage characteristics (A) and their fluctuations (B), of two (C) and three (D) graphene molecules. The effect of the external voltage on the current through the graphene plates when nothing (3C) and when another graphene molecule (3D) is sandwiched in-between the plates.

The three-layer graphene molecule yields a slightly larger current than the two-layers (Fig. 43); this is against the expectation that longer systems would yield smaller currents thus there is an additive effect when the third graphene molecule is added. The two-graphene junction shows oscillations due to the vibrational modes between the graphene plates; the three-graphene junction current-voltage characteristic oscillations are also shown. We clearly observe two similar and additive oscillations in both curves. The low frequency one corresponds to 1.2 cycles/V and the high frequency, to 5 cycles/V and their corresponding amplitudes are 0.4 and 0.5 mA respectively.

6.1.3 Conclusions

There are fluctuations in the current through the detector when an external bias is applied. These fluctuations come from two contributions: one from the nuclei vibrations (vibronics) and the other from electron oscillations (plasmonics). The former is the trivial one, nuclei move according to their intrinsic frequencies affecting the instantaneous potential in their neighborhood (Fig. 42). However, in the later, electrons are fully delocalized on the graphene molecules; their nature allows fluctuations and oscillations of the electron density corresponding to the HOMO and other near molecular orbitals. Thus, the two types of fluctuations yield changes in the current-voltage characteristics.

Plasmons on the graphene surface enhance transduction of molecular characteristics into signals readable by standard electronics. Thus, changes in both molecular electrostatic potentials and vibrations of an arbitrary molecule can be transduced and amplified into current-voltage characteristics.

CHAPTER VII
MOLECULAR DEVICES: SWITCHES*

The main-streaming of personal computers and the surge in use of hand-held digital devices such as cellular phones have been accompanied by a continued demand for faster, more versatile electronic circuits. On the forefront of research in this area is nanotechnology—designing and fabricating nano-sized electronic devices and components that provide increased functionality compared to current silicon-based technologies while occupying a fraction of the size. One promising solution for scaling–down electronic devices below the present limits of photo-lithography is the molecular circuit. Understanding and manipulating molecular conductivity is one of the initial steps in the development of such circuits (*3, 29, 186, 205*), and this requires knowledge of a particular molecule's electrical character.

Indeed, many organic and biological molecules with conductive properties have been examined as potential circuit elements. (*202, 206, 207*) Two different materials are used in this chapter to perform as molecular switches activated by light or a mechanical force. The first section shows a switch based on the photoreaction of vitamin D molecule, a molecule whose electrical conductance changes in response to light is an excellent candidate for light-activated circuits. In the second section of this chapter, a film of gold nanoparticles encapsulated with citrate molecules is used to demonstrate a switchable molecular conductivity activated by an external mechanical force, this switch also has a catalytic effect that produce the release of carbon dioxide molecules from the film.

---

* Parts of this chapter are reprinted with permission from:
- Light-Activated Molecular Conductivity in the Photoreactions of Vitamin D_3; by N. L. Rangel, K. S. Williams, J. M. Seminario, 2009. *J. Phys. Chem. A*, **113** (24), 6740. Copyright 2009 by the American Chemical Society.
- Switchable Molecular Conductivity, by K. Wang, N. L. Rangel, S. Kundu, J. C. Sotelo, R. M. Tovar, J. M. Seminario, and H. Liang; 2009. *J. Am. Chem. Soc.*, **131** (30), 10447. Copyright 2009 by the American Chemical Society.

7.1 Light-activated Molecular Conductivity in the Photoreactions of Vitamin D_3

One light-sensitive biological molecule of interest is 7-dehydrocholesterol (provitamin D_3), which, upon exposure to ultraviolet (UV) light in the range of 240-300 nm (*208*), undergoes photoconversions that lead to the production of cholecalciferol (vitamin D_3). These reactions occur in the skin, naturally providing the body with a supply of this vitamin. Its physiological importance has been established; vitamin D is known to offer protective effects against the development of cancers of the breast, colon, prostate, lung, and ovary (*209, 210*) and the therapeutic intervention and prevention of many disorders including diabetes and osteoporosis (*211*).

Through extensive studies using various cellular and liposomal models, the production of vitamin D_3 in the epidermis is currently well-understood (*212-217*). An equal effort has been given in characterizing these photoreactions outside of the body through experimental (*218-222*) and, more recently, computational techniques (*223-226*). Through their analyses, many have contributed to a more complete understanding of the photochemical process at each stage as well as the factors—solvent and wavelength, in particular—that influence the progression through subsequent stages (*208, 227-230*).

Neither the electrical properties of the molecules in these photoreactions nor their potential usage in a biomolecular circuit has yet to be considered. None has explored the ability to maximize any useful electrical properties by controlling provitamin D conversion and eliminating the undesired side products that result from over-irradiation (*231*).

In this theoretical-experimental approach, we show using *ab initio* calculations a behavior consistent with the activation of 7-dehydrocholesterol, a provitamin D_3, as an initial process toward ultra-violet—activated reactions of vitamin D_3. We find using molecular orbital theory that a conformation between the provitamin and the vitamin shows higher conductance than reactant and product. We also find experimental evidence of this electrical character by directly measuring current-voltage characteristics

on irradiated and non-irradiated samples of the provitamin. The activation of the provitamin D_3 is characterized with an increase in current during the irradiation.

7.1.1 Methodology

7.1.1.1 Theoretical approach

The energies and geometries of the molecules participating in the photoreaction of vitamin D_3 are calculated with first principles density functional theory (DFT) using the program Gaussian 03 (*232*) by means of the B3PW91 hybrid functional which uses the fully nonlocal Becke 3 (B3) exchange functional and a combination of the generalized gradient approximation and the GGA Perdew-Wang 1991 (PW91) correlation functional with the 6-31G* basis set (*23, 24, 162*). This level of theory been successfully tested to yield acceptable energetic (*19*). Electron transport is calculated using our program GENIP (*233-235*) to, which calculates current through molecules using an *ab initio* density functional theory for the discrete and continuum components of the system merge through a Greens function approach as is described in the methodology Chapter II.

7.1.1.2 Experimental approach

We prepare a solution of provitamin D_3 (~2mM) in a nitrogen atmosphere by dissolving crystalline 7-dehydrocholesterol in cyclohexane (≥99%). Both are obtained from Sigma-Aldrich and are used as received from the vendor. By using a micro-pipette, we deposit 4μLof this solution onto a borosilicate biochip patterned with gold array microelectrodes (ABTECH *Scientific, Inc.*) shown in Fig. 44. The chip is dried under nitrogen for ~3 hours and then transferred to the measurement chamber to the TTP4 Cryogenic Probe Station customized with reaction inert red light shown (Fig. 44B) and a UV lamp. We connect the probe tips to the IME portion of the chip (Fig. 44A), and bias voltages are applied across the electrodes using a semiconductor analyzer. We apply voltage in two ways—swept linearly from -1V to 1V and at constant steps of 1V. During alternate applications of constant voltage, we expose the chip to UV light of wavelength 254±10 nm obtained from a 4-watt-peak power lamp (90% efficiency) with

a filter centered at 254 nm and with a bandwidth of 30 nm (hand-held UV lamp from LDP, LLC.) for 80-second intervals. Output DC values are measured simultaneously, and are presented in time-domain plots. We repeat this procedure until the measured current values indicate complete photoconversion of the initial 7-dehydrocholesterol. Identical current measurements are made for a new, clean biochip as well as one covered with 4μL of cyclohexane. All phases of the experiment are conducted under darkroom conditions at 298K and 1atm of pressure.

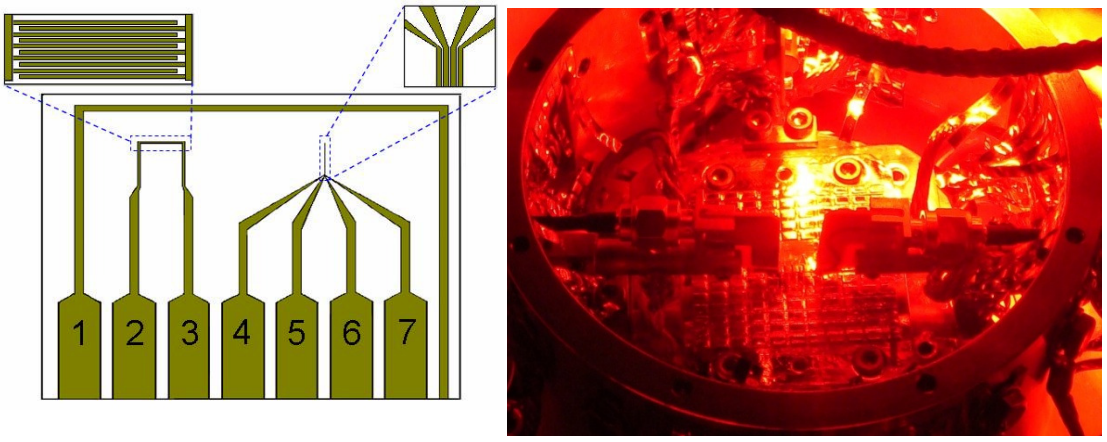

(A) (B)

Fig. 44. (A) The IAME-co-IME series chip from ABTECH Scientific, Inc. used for the experiment. It contains a total of seven gold electrodes in two different configurations: electrodes 2 and 3 are the interdigitated microsensor electrodes (IME) configuration and 4, 5, 6, and 7 are the independently addressable microband electrodes (IAME) configuration. The chip dimensions are 1.0 cm x 1.0 cm x 0.05 cm. Each electrode is 3 mm long, 2 μm wide, with 1-μm spacing between electrodes. (B) TTP4 Cryogenic Probe Station (Desert Cryogenics, LLC.). Taken from Rangel *et. al.* (*44*)

7.1.2 Results and Discussion

Fig. 45 shows the initial provitamin D_3 molecule, its immediate UV product previtamin D_3, and the final product vitamin D_3, which comes out from thermal stabilization rather than from further UV exposure. Fig. 45 does not show the additional photoproducts that come from over-irradiation of previtamin D_3 such as the ring-closure product lumisterol, which is favored at wavelengths above 300 nm and tachysterol, a product due to *cis-trans* isomerization that is more probable at smaller wavelengths

(*221*). Further wavelength-dependent side-products are generated from the over-exposure of vitamin D_3.(*228*)

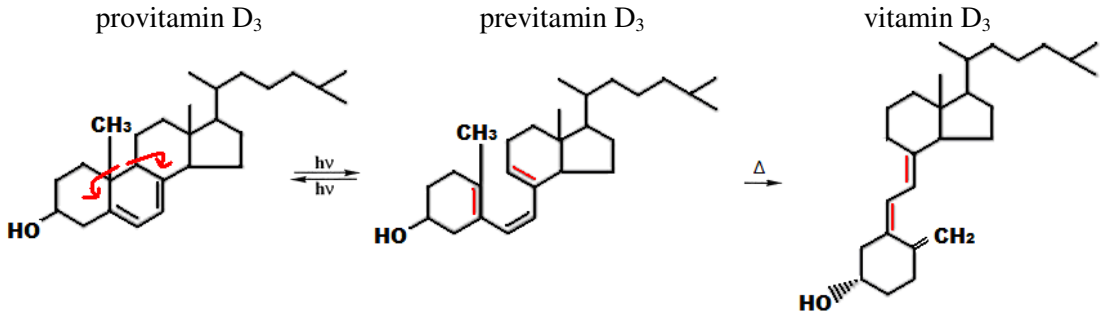

Fig. 45. Simplified photoreactions of vitamin D_3 showing the molecules analyzed in this work. The red arrows show that the single bond is broken to form the red bonds in the previtamin D_3.

Table 10. Energies, relative energies, dipole, HOMO and LUMO energies and HOMO-LUMO gaps.

Molecule	Total Energy (Ha)	Relative Energy (kcal/mol)	Dipole (Debye)	HOMO (eV)	LUMO (eV)	HLG (eV)
Provitamin D_3	-1130.182971	0.0	2.02	-5.26	-0.41	4.85
Previtamin D_3	-1130.038827	90.5	1.61	-3.37	-2.29	1.08
Vitamin D_3	-1130.162394	12.9	1.49	-5.31	-0.69	4.62
Tachysterol	-1130.174090	5.57	1.78	-5.17	-0.69	4.35
Lumisterol	-1130.162776	12.67	1.34	-5.21	-0.81	4.46
Cyclohexane	-235.799891		0.00	-7.95	2.56	10.50

The relative and total energies of the molecules in the simplified reaction scheme are shown in Table 10. The intermediate conformation at 3.92 eV (90.5 kcal/mol) above the provitamin and the vitamin is only 12.9 kcal/mol above. From Table 10 and Fig. 47, we notice that the highest occupied molecular orbital-lowest unoccupied molecular orbital (HOMO-LUMO) gap (HLG) for the initial (provitamin D_3) and final product

(vitamin D_3) of the photoreaction are 4.85 eV and 4.62 eV, respectively, while the molecular transition conformation (previtamin D_3) has a shorter HLG of 1.08 eV.

Fig. 46 shows the current-voltage curves calculated using our in situ developed program GENIP (*233-235*). In contrast with the experimental findings, higher conductivity is found for the final stage vitamin D_3 than for the initial state provitamin D_3. We attribute this difference to the side products formed by the long exposure periods able to activate those states below the tail on the onset of the UV lamp spectrum such as tachysterol and lumisterol formed in photoreactions with wavelengths of about 295 nm (*221*). Because the low stability of previtamin D3, its calculation under a current-voltage approach is really a challenge and perhaps beyond of what present methods can calculate. Self-consistent field calculations are superb for stable molecules but very problematic, as expected, for unstable ones. Short HOMO-LUMO gaps, i.e., low hardness, are indicative of poor stability of the wavefunction, which worsens as an external field is applied to the molecule.

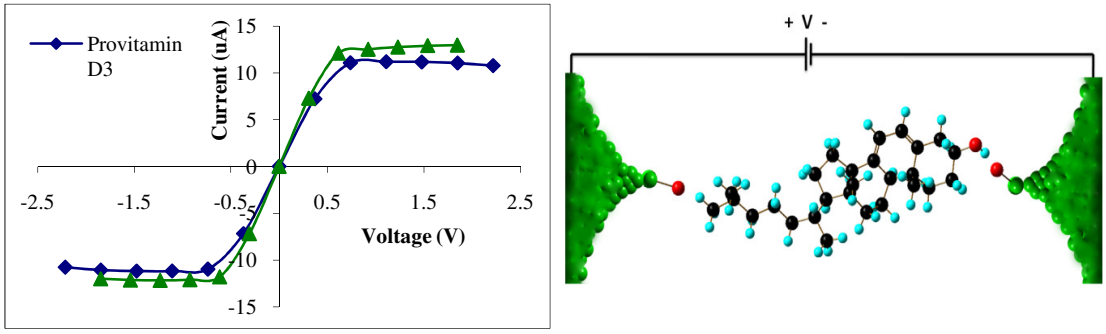

(A) (B)

Fig. 46. (A) Current-voltage characteristics for the provitamin D3 and the vitamin D3 obtained using GENIP. The differences in current are approximately 2 µA (B) Schematic representation of the contact between the studied single molecules and the gold electrodes (green), physical adsorption is assumed through hydrogen bonding. The calculations only refer to a single molecule addressed by two electrodes; certainly, in the experimental setting, a random distribution of vitamin contaminated with side products is expected with the ends of the random sample (not each molecule) connected to the electrodes. Thus calculations and experiment are at most complementary in their results in order to analyze several aspects of the system rather than to make validations of each other.

The UV light in the experiment has a wavelength of 254±10 nm, which corresponds to an energy range of 4.70-5.08 eV. Thus, the photons from the UV source provide the energy to excite an electron from the HOMO to the LUMO (4.85 eV) of provitamin D_3 which in turn yields to the intermediate conformation (previtamin D_3) at 3.92 eV above. The provided energy breaks the bond of one ring as is shown in Fig. 45 and consequently stabilizing in vitamin D_3. The HLG at the transition conformation decreases but it is actually a local minimum as the reactant and the product are. The energies of the molecular orbitals are shown in Fig. 47. The shapes of the HOMO (H) and LUMO (L) for the three molecules in the photoreaction show localizations in the neighborhood of the three adjacent six-member carbon rings, in which the photoreactions take place.

Previtamin D3 and vitamin D3 both have the HOMO (Table 10) closer to the Fermi level (-5.3 eV) of the gold contacts thus based on the solid state, they are "electron" conductors, but on the other hand the electron-hole model is perhaps not the best model to explore the conduction behavior in this case. A more sophisticated picture is given by the molecular orbital theory. The localization of the molecular orbitals (MOs) on the rings of the molecules and their HOMO-LUMO gaps suggest poor conduction with a transport path expected through nonbonded sites connecting the double bonds, in the experiment a self-assembled monolayer physically absorbed in the glass substrate is expected. To make sure that no other MO's is strongly involved in the conduction process, we calculate the shape and energies of the HOMO-1 and HOMO-2; they show the same degree of localization as the HOMO (shown in Fig. 47) but at larger energy separation (1.55 eV or more) than the HOMO energy from the Fermi level. This explanation taken from molecular orbital theory is much more suitable than using the electron-hole models from solid state theories in which the conduction could be regarded as "electron" conduction as opposed to "hole" conduction.

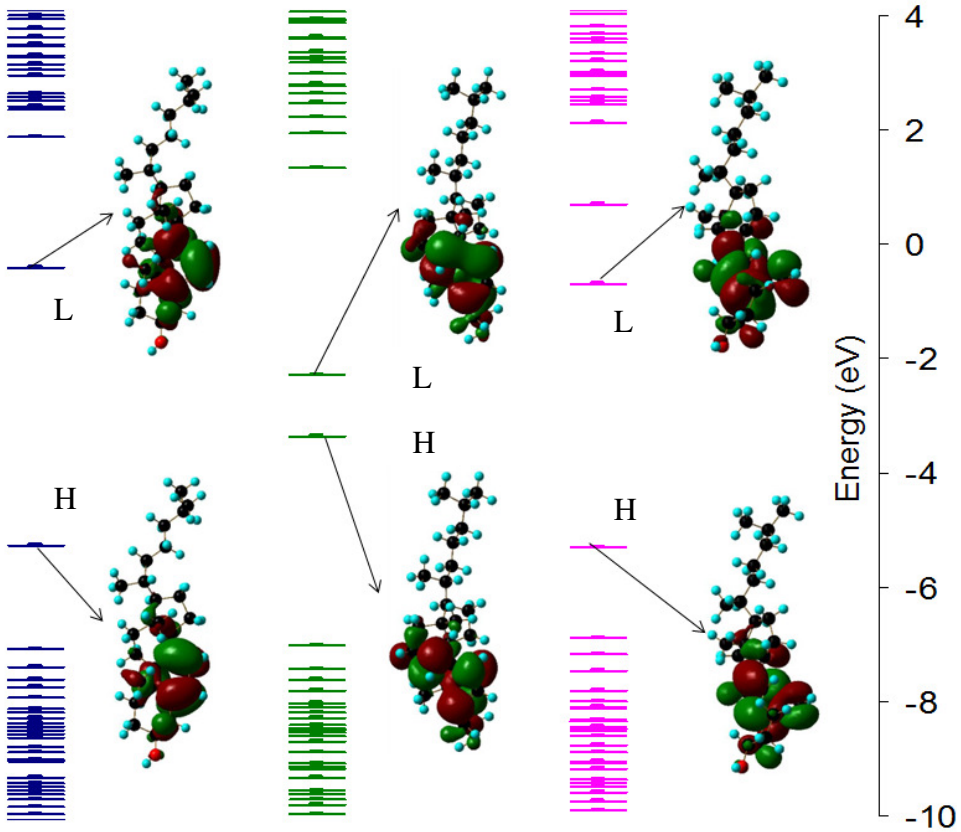

Fig. 47. Molecular orbitals of provitamin D_3 (blue), previtamin D_3 (green), and vitamin D_3 (pink). LUMO (L) and HOMO (H) shapes and energies are shown; only energies are shown for the other MOs.

Fig. 48A shows the experimental current response of the chip when a constant voltage of 1 V is applied between the metallic contacts. A reversible decrease in current is observed before the application of UV light as is shown in Fig. 48B. Immediately upon UV exposure, the current increases up to a maximum and then decreases in a manner similar to that when the UV source is off. This behavior is only observed when the chip is covered with the provitamin D_3 solution, i.e. when the solvent is completely evaporated and only the provitamin D_3 molecules are filling the gaps between the electrodes. The current responses for both the clean chip and the chip covered with only solvent are measured under the same irradiation conditions used for the provitamin D_3. Neither the chip nor the solvent displays the electrical behavior observed when the

provitamin is present. Thus, we can confidently assign the peak in current that accompanies UV exposure to the provitamin D_3 molecules. In the experiment a change of 5 pA is measured between the initial and final stage, such small current values can be measured in standard CMOS electronics.

The gradual decreasing current response observed after UV exposure is unexpected from the HLG of the molecules in the simplified reaction scheme. Because of their similar HLGs and shape of molecular orbitals, we could expect the initial and final resistivity to be also similar.

Additional photoproducts are guaranteed to be present due to our experimental approach (i.e. long UV exposure times), such as lumisterol and tachysterol that are not shown in our analysis. However, we found properties very similar to the vitamin D_3, and the presence of the additional photoproduct molecules can account for the change in resistivity as the provitamin D_3 molecules undergo photoconversion.

However, a possible change in the orientation of the molecules from a higher order in the case of the provitamin due to its larger dipole moment to lower order in the vitamin due to its 25% lower dipole that may carry out the decrease in conductivity in the final stage is not ruled out.

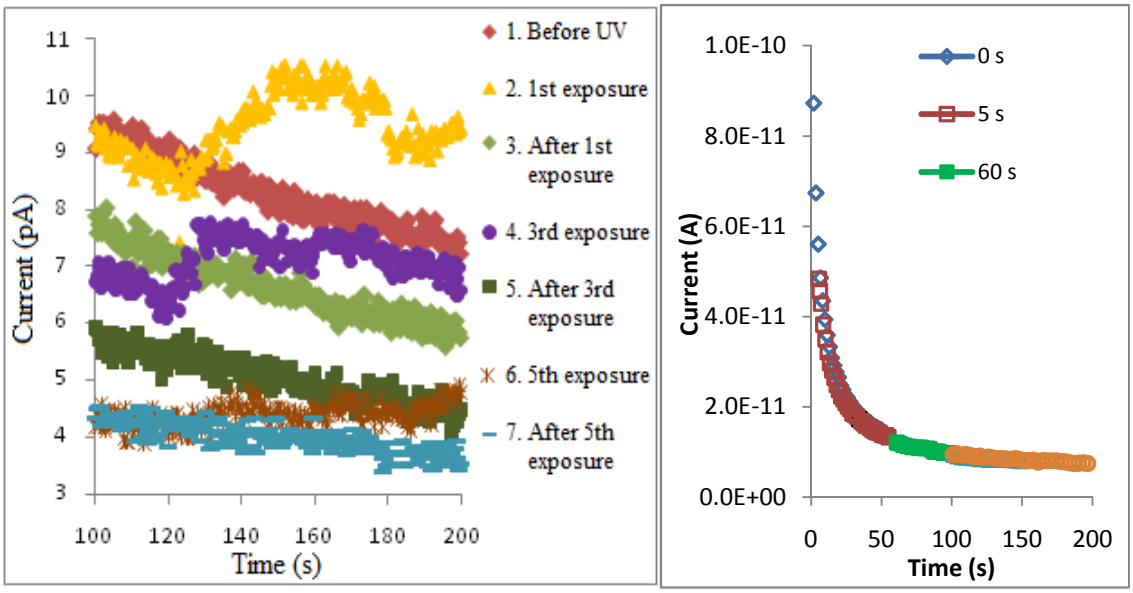

(A) (B)

Fig. 48. (A) Current responses when a constant voltage of 1 V is applied on the electrodes 2 and 3 of Fig. 44 using a wait time of 100 s during an interval of time of 0.5 s. The total time for each consecutive measurement is 6.3 minutes. The exposure to UV starts at 120s of voltage application and continues until 200 s. (B) Current versus time plot for the provitamin D_3 before irradiation using different wait times (voltage application time before start measuring), the results presented in (A) follow the orange curve (from 100 to 200 s) where the change in current was 0.02 pA/s. Thus no matter how many times we repeat the experiment, the I-V behavior is identically the same as long as the sample is not irradiated. Notice in (A) that the behavior is different when the sample is expose to UV radiation (curve 2). The UV exposure is repeated five times, when no more changes in current are detected.

Control experiments such as pure reaction compounds and mixtures can be performed; however, the information we would obtain as a control experiment is already available as only the first measurement corresponds to pure provitamin D_3; all other measurements correspond to a mixture of provitamin D_3, vitamin D_3 and side products. These measurements were needed to analyze provitamin D under UV irradiation.

We expose the sample five times to the UV light. Fig. 48 shows the first, third, and fifth exposures. During the third exposure a change in current occurs when the UV is turned on and the switching behavior is smaller each time that the UV is turned on and after the fifth time when no change in current is observed which we attribute to the end of the photoreaction, when all the provitamin D_3 has reacted and no more previtamin D_3 appear when the light is on.

7.1.3 Conclusions

We have shown by a theoretical-experimental *ab initio* based approach the activation of 7-dehydrocholesterol, a provitamin D_3, as an initial conformation toward ultra-violet—activated reactions of vitamin D_3. A molecular conformation between the provitamin and the vitamin is found with higher conductance than reactant and product. We also find experimental evidence of this electrical character by directly measuring current-voltage characteristics on irradiated and non-irradiated samples of the provitamin. The activation of the provitamin D_3 is characterized with an increase in current during the irradiation. Energetic of the conformations and electronic structure suggest a consistent behavior with the experiment showing a molecular switch by its change in conductivity triggered by ultraviolet radiation of energy similar to the calculated theoretically for the molecules. It is also proposed that based on the dipole moment we can explain the behavior of reactant and product that happen to have most other similar characteristics but the dipole, which strongly affects intermolecular order.

7.2 Citrate Encapsulated Gold Nanoparticles Film: Mechanocatalytic Switches

We demonstrate the switchability of the molecular conductivity of a citrate. This was made possible through mechanical stretching of two conformers of such citrate capped on and linked between gold nanoparticles (AuNPs) self-assembled as a film. A complementary theory-experiment approach is used to find the electron flux in the backbone. We found that the molecular conductivity depends on the pathways of electrons that were controlled by the applied mechanical stress. Under stress, we could turn the conductivity up and down for as much as ten-fold. The mechanochemistry behind this phenomenon is an alternative branch of chemistry.

Under a tensile stress, it is possible to activate the oxidation of gold nanoparticle and its capping citrate molecules. The mechanoactivation of oxidation was studied using the X-ray photoelectron spectroscopy (XPS) and *ab initio* simulation of self-assembled gold nanoparticles (AuNPs) on a polyvinylindene fluoride (PVDF). Generally, stress

associated oxidation of inorganic materials is related to the stress corrosion cracking or chemical-mechanical polishing. In contrast to modify a surface, we demonstrated the mechano-oxidation under a highly controlled manner and the externally applied stress was able to guide the reaction pathways and to release certain reaction products.

7.2.1 Experimental Section

Gold film samples are fabricated at Dr. Liang's laboratory in the Mechanical Engineering Department in Texas A&M. Polyvinylindene fluoride (PVDF) was used as the substrate for the thin film preparation. The PVDF substrates were cleaned thoroughly in acetone with sonication for 20 minutes and functionalized with poly allylamine hydochloride (PAH, 0.1% by weight). The PAH has been used widely in literature for surface functionalization due to its positive charge. The functionalized substrates were immersed in the AuNPs solution for about 30 minutes and dried in a vacuum chamber. After the first monolayer was deposited, the substrate was visible as light pink. Subsequent layers were deposited by repeated alternate immersion in AuNPs solution and drying. Finally a golden metallic luster was obtained after 8 times depositions. Typically, these films contain aggregates of AuNPs as particles.

Surface morphologies using atomic force microscopic (AFM) images of the film over a 1 μm x 1 μm area are shown in Fig. 49A for the as-prepared film and Fig. 49B for the mechanically stretched film (strain=0.5%).

The AuNPs in the as-prepared film have an average diameter of 80 nm, those in the stretched film 100 nm, a variation of less than 25%, showing that quite possibly some of the particles have coalesced under strain conditions while most of them remain on the whole unstrained. The stretch, moreover, reorients the particles in the elongation direction (left-to-right) and seems to cause the brunt of the deformation in the gaps between adjacent particles as suggested by the increase of interstitial space between particles in the stretched film relative to that in the as-prepared film. As a result, the RMS surface roughness increases from ~7.6 nm for the as-prepared film to ~13.4 nm for the stretched film. The above results relate to deformations that have been observed on

the film surface. We do not have direct evidence that the same deformations occur also inside the film. Nevertheless, the reorientation of the particles in the direction of the stretching seems to indicate that this may well be the case.

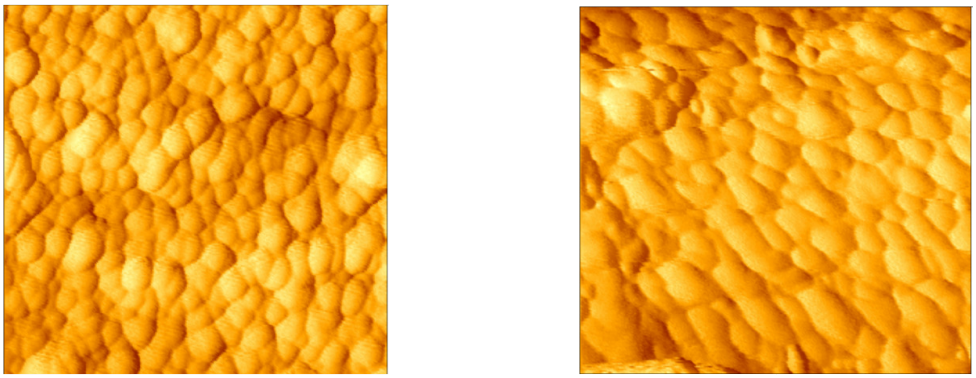

(A) (B)

Fig. 49. Noncontact mode AFM images of self-assembled Au NP film. (A) Surface morphology without deformation. (B) Surface morphology with deformation.

7.2.2 Theoretical Section

Sodium citrate (trisodium 2-hydroxypropane-1,2,3-tricarboxylate) is used in the experiment to encapsulate the gold NPs. In the final system all the Na^+ is released and the negatively charged molecule act as interface between gold NPs.

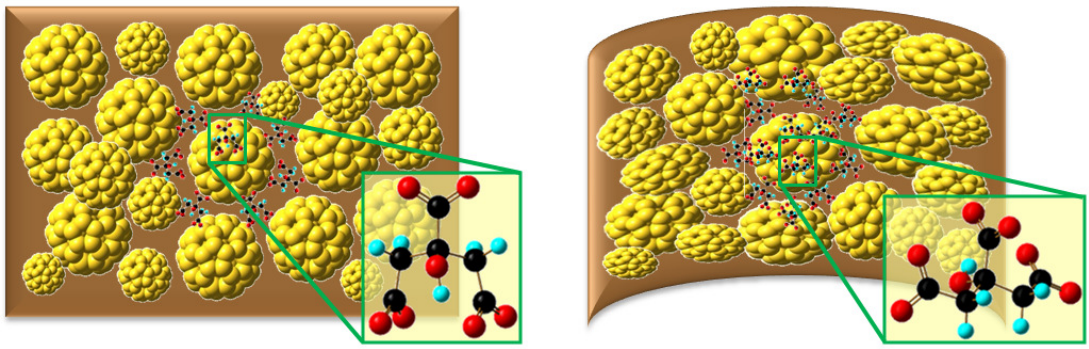

(A) (B))

Fig. 50. Two conformers of 2-hydroxypropane-1,2,3-tricarboxylate. (A) Citrate-1 with relative energy of 4.60 kcal/mol is expected on the film before deformation and (B) Citrate-2, a more stable conformer (relative energy 0.00 kcal/mol) present on the film after deformation.

Within our model citrate molecules are encapsulating the gold NP as is shown in Fig. 50; Citrate-1 would be present in the film before stretching and Citrate-2 after the stretching, reaching the most stable conformation under an external force.

Finite-cluster calculations as described in Chapter II are done using density functional theory (DFT), as implemented in the Gaussian 03 program (*201*), by means of the B3PW91 hybrid functional—the electron correlation energy is computed using the nonlocal Perdew-Wang (PW91) functional whereas the exchange contribution is computed with the hybrid Becke3 (B3). All the calculations are performed using the 6-31G(d) (*199*) basis set for hydrogen, carbon and oxygen atoms, and the LANL2DZ basis sets and effective core potentials (*20, 21, 200*). The current through the junction is computed via a density functional theory DFT and Green's function implementation of an extended Landauer formalism (GENIP (*233-235*)).

7.2.3 Switchable Molecular Conductivity

With recent success of making small two and three (2-D and 3-D) dimensional structures, new understanding in electronic transfer and tunneling effects (*236-243*) has provided alternative methods to detect the electronic flux (or pathway) of encapsulated molecules. Vapor sensors and strain gauges being two widely known applications (*244, 245*). To date, a precise characterization of the backbone of the flux pathway is still lacking and control of the same has not been reported (*246, 247*). In this work, we demonstrate that it is possible to switch the molecular conductivity of self-assembled citrate-capped gold nanoparticles (AuNPs) through mechanical stretching of two conformers of the capping citrate. We could turn the conductivity as much as ten-fold. Our results suggest that the molecular conductivity depends moderately on the local neighborhoods of these conformers in the film of AuNPs.

7.2.3.1 Experimental results

To examine the electronic transport properties of the AuNP film, a current-voltage (I-V) curve was measured at the room temperature. In the elongation direction (Fig. 51), the resistance of the film was increased from 0.31 MΩ to 1 MΩ, due to

deformation, about 223% increase. On the contrary, only a moderate increase (from 62 mΩ to 80 mΩ) was found in the sputtered Au film, i.e., 29% increase.

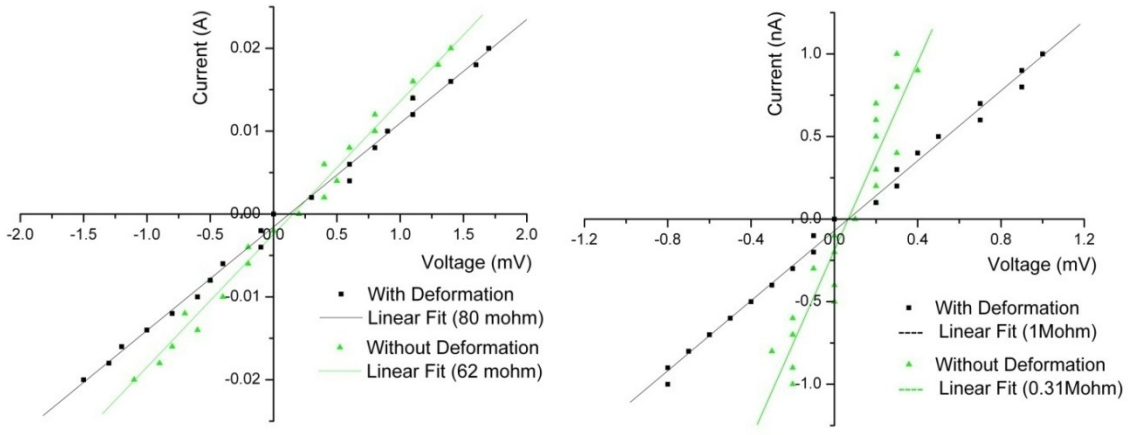

(A) (B)

Fig. 51. I-V measurements of sputtered Au film and self-assembled AuNP film. (A), Sputtered Au film with and without deformation; (B), Self-assembled AuNP film with and without deformation.

Our results showed that the conductivity of a self-assembled AuNP film was dominated by the encapsulated molecules under strain. In order to understand this further, we conduct molecular *ab initio* calculations.

7.2.3.2 Theoretical results

Two conformers of sodium citrate (trisodium 2-hydroxypropane-1,2,3-tricarboxylate) with the lowest energies (Table 11) are considered to model the bridge-molecule between two AuNPs before and after the application of an external force, as labeled Citrate-1 (Fig. 52A) and Citrate-2 (Fig. 52B). Their configurations, when inserted in the junctions (namely, extended with one-atom gold electrodes), are shown in Fig. 52C and Fig. 52D. When a force is exerted on the film, it is likely that the average inter-particle distance between the particles increases. We choose the shortest of the molecular bridges (as measured by the distance between gold atoms), Citrate-1 (6.2 Å), as the representative between NPs before film stretching; and the longest, Citrate-2 (8.93 Å), as that after. We assume that they are the representative bridges along the

conductivity percolation paths in our model film before and after elongation, respectively.

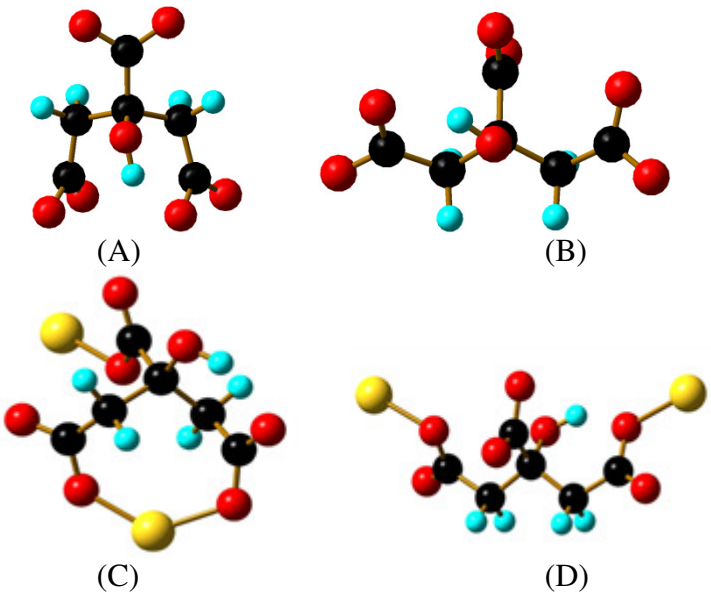

Fig. 52. Two conformers of 2-hydroxypropane-1,2,3-tricarboxylate. Stand-alone Citrate-1 (A) and Citrate-2 (B); Extended (with one-gold-atom electrodes) Citrate-1 (C) and Citrate-2 (D).

There are two reasons for such a choice. Firstly, Citrate-1—Au_2 is more stable than Citrate-2—Au_2 by 7.20 kcal/mol (Table 11). It is therefore a more likely configuration to be present in the relaxed (unstretched) film. Secondly, the length difference between each citrate is 2.73 Å, such that using the average diameter of AuNPs (70 nm), the stress-induced transition from Citrate-1 to the Citrate-2 structure is ~0.4%, close to the calculated strain (0.5%).

Table 11. List of energies, relative energies, HOMO and LUMO energies, and HOMO-LUMO gaps (HLG) for the standalone and extended citrates.

Molecule	Energy (Ha)	Relative Energy (kcal/mol)	HOMO (eV)	LUMO (eV)	HLG (eV)
Citrate-1	-757.729473	3.60	-8.54	-5.90	2.64
Citrate-2	-757.735219	0.00	-8.49	-5.90	2.59
Citrate-1 Au_2	-1028.609268	0.00	-7.46	-6.07	1.39
Citrate-2 Au_2	-1028.597795	7.20	-7.18	-4.90	2.29

The transformation from a Citrate-1 junction to a Citrate-2 will affect the electrical properties of our model film. This is already apparent from the ~65% increase in the transport barrier as measured by the junction's HOMO-LUMO gap (Table 11). In such, the presence of a Citrate-2 junction will decrease the conductivity of the film. This is in fact what we observe in the calculated I-V characteristics of the junctions (Fig. 53A).

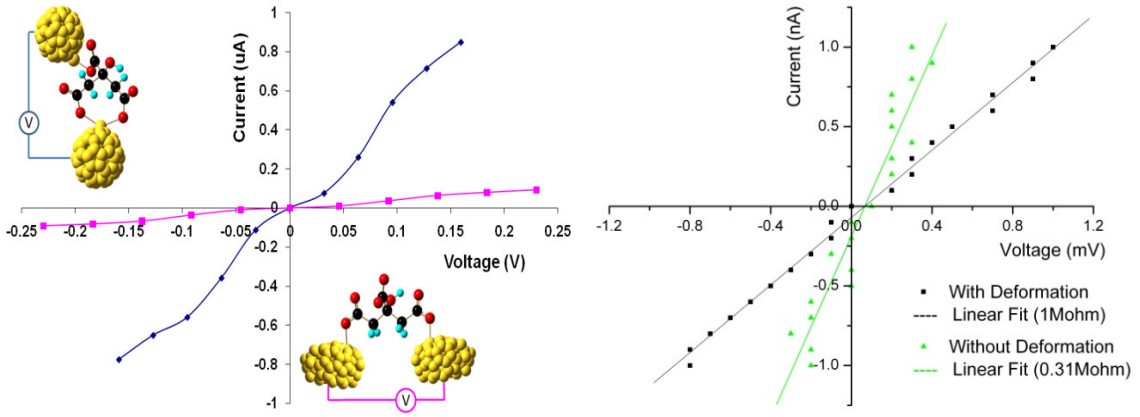

(A) (B)

Fig. 53. Comparison of I-V characteristics for the AuNPs film. (A) I-V curve for the model film; and (B) Measured I-V curve.

The resistance of the Citrate-1 junction (sample without deformation) is 0.2 MΩ (blue line); that of the Citrate-2 junction (sample with deformation) is 2 MΩ (pink line). These are compared with the resistances obtained from the measured I-V characteristics of the self-assembled-AuNP film, with and without deformation (Fig. 53B). The film

sample has a resistance of 0.31 MΩ before deformation and 1 MΩ after. In model and experimental results (Fig. 53A and B), an increase of the resistivity is found after film elongation. Nevertheless, they have different increasing ratio (resistance-to-deformation/initial resistance). For simulation this ratio is 10 and for experiment about 3. This is to be expected due to the simplicity of the interface structures used in our model film, i.e., a binary set. A slightly more realistic interface would consider a mixture of both junctions, whereby there are more Citrate-1 junctions at the interface before deformation and more Citrate-2 junctions after, resulting the reduction of the increase ratio.

7.2.3.3 Conclusions

We investigated the response of electron flux of a self-assembled AuNPs film to a mechanical force. Under stress, the electron pathway underwent a transition between conformers of citrate encapsulated molecules. The stress-induced transition of conductivity was confirmed both in experiments and simulation. This indicates that it is possible to design single-electron devices which molecular conductivity could be switched on and off and to a desired value.

7.2.4 Activation of Carbon Dioxide and Film Oxidation

Research work driven by the perspective applications in catalysis has demonstrated that, the application of electrochemical potentiostat to core-shell assembled Au NP catalysts can activate the surface reconstitution of the nanostructured catalysts. The action of potential polarization on Au NP deposited glassy carbon electrode is to trigger the catalytic activities (*248, 249*). It proves the property tailoring of Au nanostructures upon electrocatalytic activation.

Most recently, an interesting work was conducted by Fernandez *et al.* (*250*). They investigated the catalytic mechanism of Escherichia coli thioredoxin (Trx) by applying a mechanical force in the range of 25-600 pN to a disulphide bond substrate and monitoring the reduction rate of the bonds by Trx. Their results show that the applied mechanical force can alter the chemistry of the catalytic site in thioredoxin

significantly. The reduction rate decreases dramatically as the force increases from 35pN to 300 pN for higher Trx concentration. They proposed that the increased mechanical forces applied to target di-sulphide bonds would inhibit the activity of thioredoxin and diminish the effectiveness of the antioxidant properties of the enzyme. It shows the possibility that we can control the catalytic activation through mechanical force.

7.2.4.1 Simulation Results

The geometries and charges of the two citrate conformers used to describe the model are shown in Fig. 54.

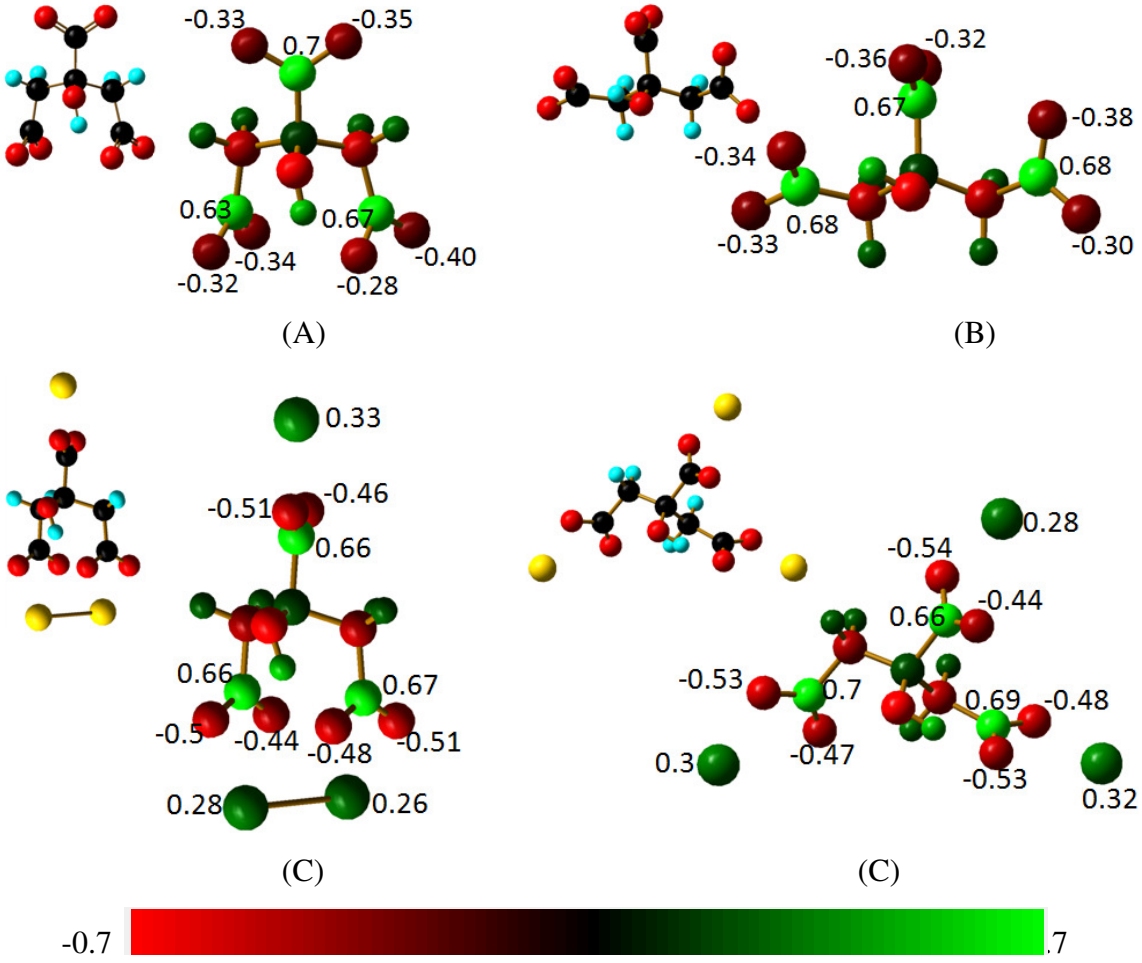

Fig. 54. Optimized geometries and Mulliken charges for the isolated Citrate-1 (A) and Citrate-2 (B). Bottom figures correspond to (C) Citrate-1 and Citrate-2 (D) when a gold atom is located nearby each CO_2 groups.

The Mulliken population analysis for Citrate-1 and Citrate-2 is shown in Fig. 54A and Fig. 54B; both structures are negatively charged in each CO_2 group. In Fig. 54C and Fig. 54D a gold atom is added per CO_2, showing that the gold becomes positively charged and helps to neutralize the negative charges of the citrates.

The Citrate-1, Citrate-2 and a layer of gold atoms are optimized, total energy, relative energy, highest occupied molecular orbital (HOMO) and lowest unoccupied molecular orbital (LUMO) energies along with their corresponding HOMO-LUMO gap (HLG) are shown in Table 12.

Table 12. Total, relative and binding energies, dipole moment, HOMO, LUMO and HLG for every system studied.

Molecule	Energy (Ha)	Dipole (Debye)	HOMO (eV)	LUMO (eV)	HLG (eV)
Citrate-1 – 3Au	-1164.391179	0.44	-6.91	-4.65	2.26
Citrate-2 – 3Au	-1164.391438	2.76	-6.78	-4.08	2.69
Gold Layer	-1219.861774				
Citrate-1 – 1 lay	-1977.894613	3.59	-5.88	-3.48	2.39
Citrate-2 – 1 lay	-1977.876243	2.72	-6.31	-3.59	2.72
Citrate-1 – 2 lay	-3197.787219	5.01	-5.22	-4.19	1.03
Citrate-2 – 2 lay	-3197.760451	2.48	-6.48	-5.52	0.95

The same neutralization of the negatively charges in the CO_2 groups of both citrate conformers by the positively charged gold atoms occurs when two layers of gold atoms are used as the surface of two AuNPs as is shown in Fig. 55A and Fig. 55B, each citrate linking in-between AuNPs acts as stable molecules encapsulating the AuNPs, however, when only one layer of gold is used reproducing the upper surface of the particle, there are un-neutralized CO_2 groups weakening the bond of the negatively charged CO_2 and yielding its release as is shown in figure Fig. 55C and Fig. 55D.

The gold acts as a catalyst of CO_2 carboxyl groups. When citrate molecules are in between AuNP there is not release of CO_2 molecules. Under the deformation the

distance between AuNP increases and more citrate molecules are expected on the film surface, or simply their charge are not sufficiently neutralized and therefore increasing the release of CO_2 groups. This result explains the decreasing in oxygen from carboxyl groups after the deformation shown in Table 13.

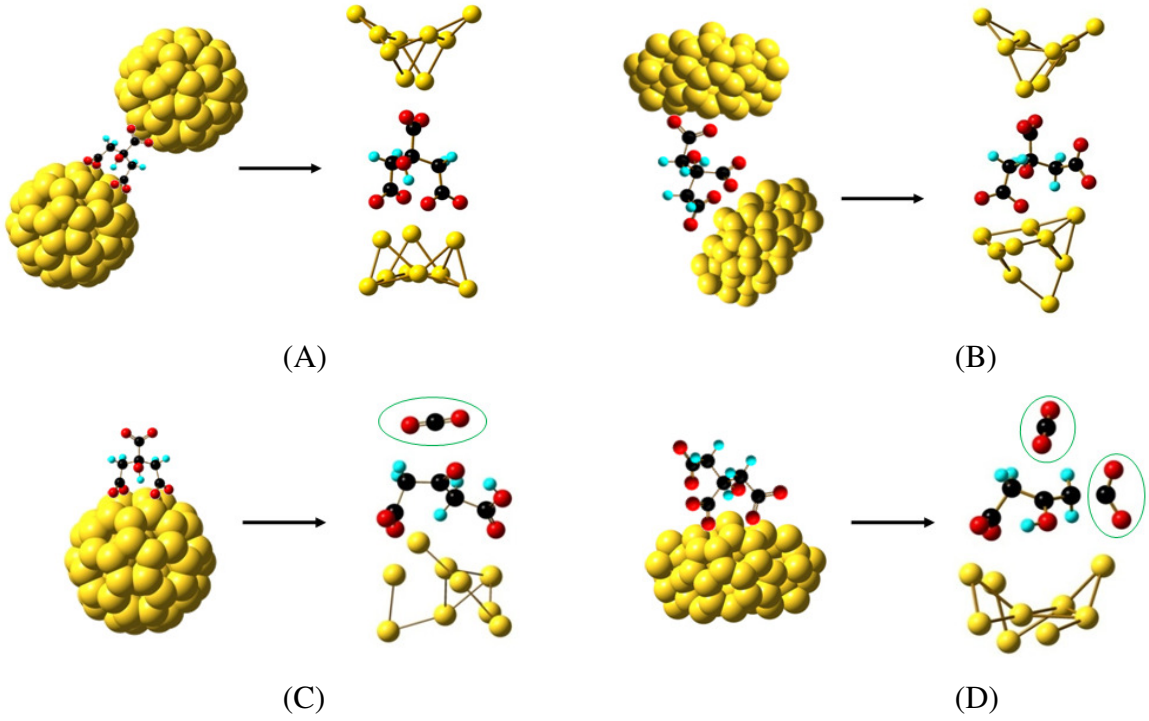

Fig. 55 Optimized structure of (A) Citrate-1 in between two gold layers and (B) Citrate-2 in between two gold layers. (C) Citrate-1 on top of a gold layer, a CO_2 group is released (D) Citrate-2 on top of a gold layer, two CO_2 groups are released. The figures show a release of CO_2 when the citrate molecules are not encapsulated by gold.

Table 13. Binding energies percentage before and after deformation.

	Without Deformation			With Deformation		
	Total Area	Area	Ratio	Total Area	Area	Ratio
O 1s (Au Oxide)	3689.9	518.9	14.06%	3906.4	1136	26.19%
O 1s (Carboxil)		738.5	20.02%		448.7	13.48%
O 1s		2432.5	65.92%		2321.7	60.33%

As we have seen, the AuNPs respond to a tensile stress with structural modifications such as adjusting inter-particle separations. This leads to stretching of the citrate molecules capping the AuNPs. We have used X-ray Photoelectron Spectroscopy (XPS) to explore such effects under longitudinal elongation (strain=0.5). The electron binding energy (BE) Au $4f_{7/2}$ (metallic) is shifted 0.4 eV compared with the un-stretched. The peak's full width at half maximum (FWHM) is increased by 90%. This suggests that the chemical environment of Au atoms is altered by the stress. The shift in BE is an indicative of the presence of Au oxide and Au-O coordination. For the sample without deformation, the difference of Au 4f peaks between two sets of deconvoluted peaks is 0.7 eV that is consistent with the reported Au-O coordination XPS result. The deconvolution results confirm that there is only a small portion of gold atoms in coordination with oxygen. For the sample with deformation, the difference of Au 4f peaks (between the first and third sets) is 2.9 eV, similar to the reported XPS data of Au_2O_3. The deconvolution results demonstrate the presence of Au oxide and a large portion of gold atoms in coordination with oxygen, which causes the spectrum shift under deformation.

7.2.4.2 Conclusions

We investigated mechano-oxidation of capping citrate molecules in self-assembled AuNPs. Results showed that a mechanical force could catalyze the carboxylate group in the capping citrate resulting in the oxidation of citrate and releasing of CO_2. The gold itself was also oxidized. The oxidation of citrate and gold under stress was controllable by its amplitude. The simple method is feasible for other chemical systems. The use of NPs further improves the controllability of reactions.

CHAPTER VIII
VIBRONICS AND PLASMONICS GRAPHENE SENSORS*

A high sensitivity and selectivity sensor is proposed using graphene ribbons able to read molecular vibrations and molecular electrostatic potentials, acting as an amplifier and as a transducer converting molecular signals into current-voltage quantities of standard electronics. Two sensing mechanisms are used to demonstrate the concept using ab-initio density functional methods. The terahertz region of the graphene spectrum can be used to characterize generated modes when single molecules are adsorbed on the ribbon surface. Characteristic modes can be obtained and used as fingerprints, which can be transduced into current by applying a voltage along the ribbons. On the other hand, the fully delocalized frontier molecular orbitals of graphene ribbons, commonly denominated plasmons in larger solid state structures, are extremely sensitive to any moiety approach; once plasmons are in contact with an "agent" (actually its molecular potential), the transport through the ribbons acting as electrodes catching the signals, is strongly affected.

In this chapter two detection scenarios are used for detection using graphene ribbons (Fig. 56): The generation of terahertz signals due to vibrations between the absorbed molecule and the ribbon (Fig. 56A) where the signals can be recovered thanks to the few low frequency modes present in the single layer graphene, and the effect on the electrical transport when the sandwich-like arrangement of ribbons are used as electrodes (Fig. 56B) as well as the effect when the agent molecule interacts with the delocalized electron density on the ribbon surface are presented.

---

* Parts of this chapter are reprinted with permission from:
- Graphene terahertz generators for molecular circuits and sensors; by N. L. Rangel and J. M. Seminario, 2008. *J. Phys. Chem. A*, **112** (51), 13699. Copyright 2008 by the American Chemical Society.
- Vibronics and plasmonics based graphene sensors, by N. L. Rangel and J. M. Seminario, 2010. *J. Chem. Phys.*, **132**, 125102: 1-4. Copyright 2010 by the American Institute of Physics.

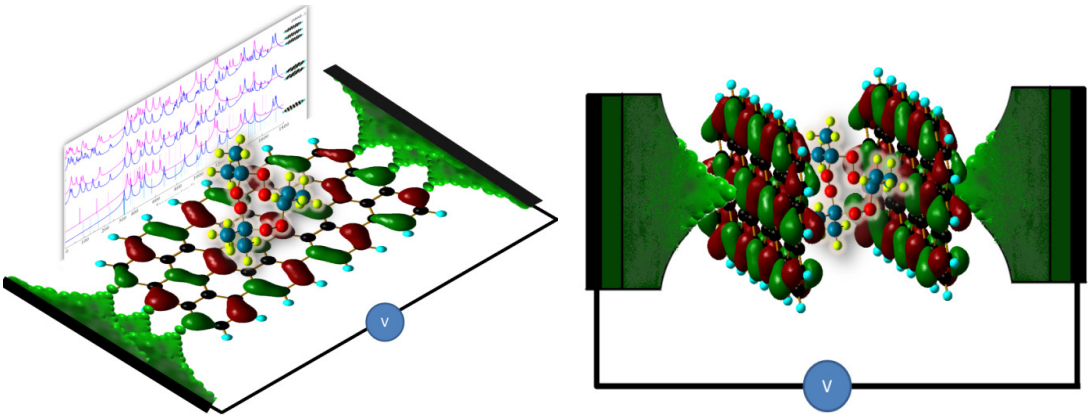

(A) (B)

Fig. 56. Proposed scenarios using graphene ribbons as detectors. (A) Characteristic vibrations under the presence of an agent molecule on the surface of a graphene ribbon. Terahertz signals are transduced and amplified in terms of current-voltage characteristics. (B) Graphene plasmonic electrodes: The fully delocalized molecular orbitals of graphene ribbons act as plasmons on the surface, and are able to detect molecular vibrations by changes in the current flowing through the two ribbons acting as electrodes. Both panels show the fully delocalized highest occupied molecular orbital (HOMO) of graphene.

The hybrid functional M05-2X, which has an improved performance for nonbonded interactions and π-π stacking,(*27*) is used as level of theory, the optimized structure of the graphene nanoribbons (GNRs) is calculated in every case. All calculations are performed with the 6-31G(d) basis using the program Gaussian 03 (revision E01).(*201*) Once the optimized geometries are found, the Raman spectrum is calculated. Current-voltage characteristics are calculated as needed using the program GENIP as described in Chapter II.

8.1 Graphene Terahertz Generator

Currently, graphene nanoribbons (GNRs) with less than 10 nm width can be fabricated and used as semiconductors (*251*). Their Raman spectra have been determined experimentally for different numbers of layers (*252*). With this information, an opportunity for new graphene applications is presented here: a sensor in the terahertz region.

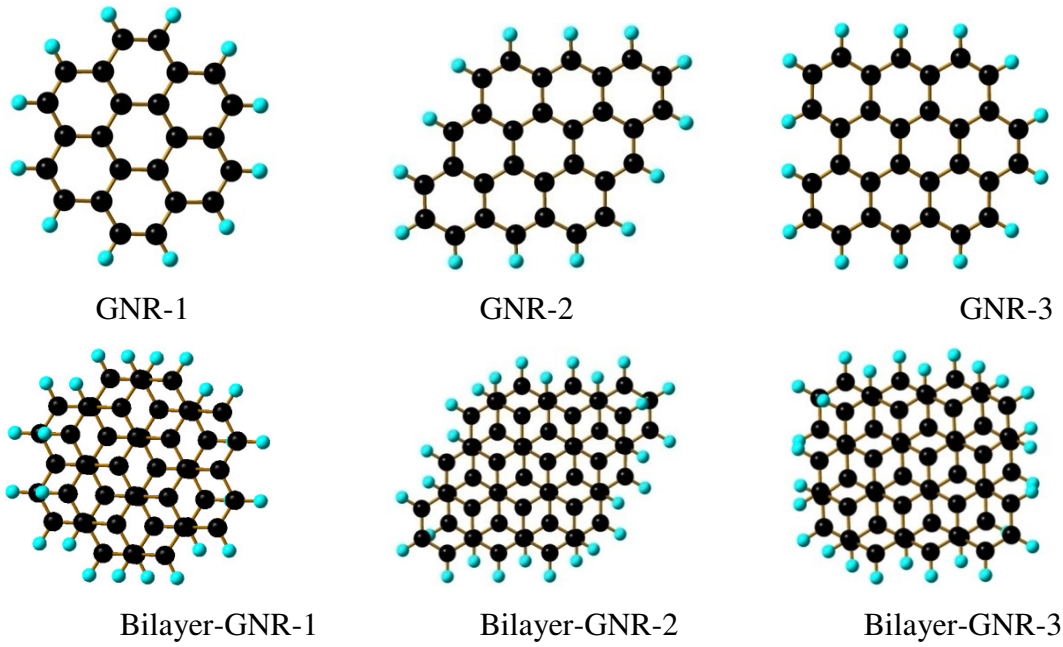

Fig. 57. Graphene nanoribbons (GNRs) used considering different edges configurations. GNR-1: zigzag and armchair edges GNR-2: Monolayer graphene with both zigzag edges and GNR-3: Monolayer graphene with zigzag (horizontal) and armchair (vertical) edges. At the bottom the bilayer structures of GRN-1, GRN-2 and GRN-3. Black spheres are carbon atoms and blue spheres are hydrogen atoms.

The coupling between graphene layers is evaluated through the binding energies, i.e., difference between the total energy of the optimized cluster with the energies sum of the optimized individual layers. The total and binding energies, highest occupied molecular orbital (HOMO) and the lowest unoccupied molecular orbital (LUMO) energies, HOMO-LUMO gap (HLG) energies along with their imaginary frequencies for the optimized structures are shown in Fig. 57 are presented in Table 14.

The only one imaginary frequency (11.1*i)* is obtained for the bilayer GNR-3. The interlayer distance is shorter for the GNR with zigzag edges and the binding energy is slightly affected by them. The GNRs shown in Fig. 57 are also calculated without hydrogen atoms at the edges (non-passivated structures), and the binding energy is 0.5 kcal/mol stronger, since the hydrogen-hydrogen repulsion are eliminated from the system. The HLGs are shorter in the bilayer compared with the single layer for each GNR case, the effect of the edges in the HLG is noticed comparing GNR-2 and GNR-3, larger gap is presented with armchair edges than with zigzag edges, and finally the gap is

also affected by the number of carbon atoms as is noticed comparing GNR-1 with GNR-2 and GNR-3, with a larger number of carbons the HLG trends to decrease.

Table 14. Monolayer and bilayer graphene nanoribbon results, including total energy, binding energy (between layers), HOMO and LUMO energies, HLGs and number of imaginary frequencies.

GNR Mono/Bi-layer	Total Energy (Ha)	Binding Energy (kcal/mol)	HOMO (eV)	LUMO (eV)	HLG	# of Im Freqs
GNR-1	-921.841934	-	-6.67	-0.63	6.04	0
Bilayer-GNR-1	-1843.702717	-11.83	-6.31	-0.63	5.69	0
GNR-2	-1151.680690		-5.61	-1.77	3.84	0
Bilayer-GNR-2	-2303.386572	-15.81	-5.36	-1.82	3.54	0
GNR-3	-1151.693127		-5.77	-1.61	4.16	0
Bilayer-GNR-3	-2303.410458	-15.19	-5.44	-1.55	3.89	1

Symmetry of the GNR-1 and GNR-2 is C_{2V}, and for GNR-3 is C_1. As is shown in Fig. 58, modes without Raman amplitude are presented at low frequencies for the ribbons with C_{2V}. They are all visible for the graphene with C_1.

None of the monolayer GNRs show either visible or hidden modes of frequencies in the range less than 50 cm^{-1}. The GNR-1 does not present any visible mode for frequencies lower than 300 cm^{-1}, for this reason this is the ribbon used for the sensing calculations in this section.

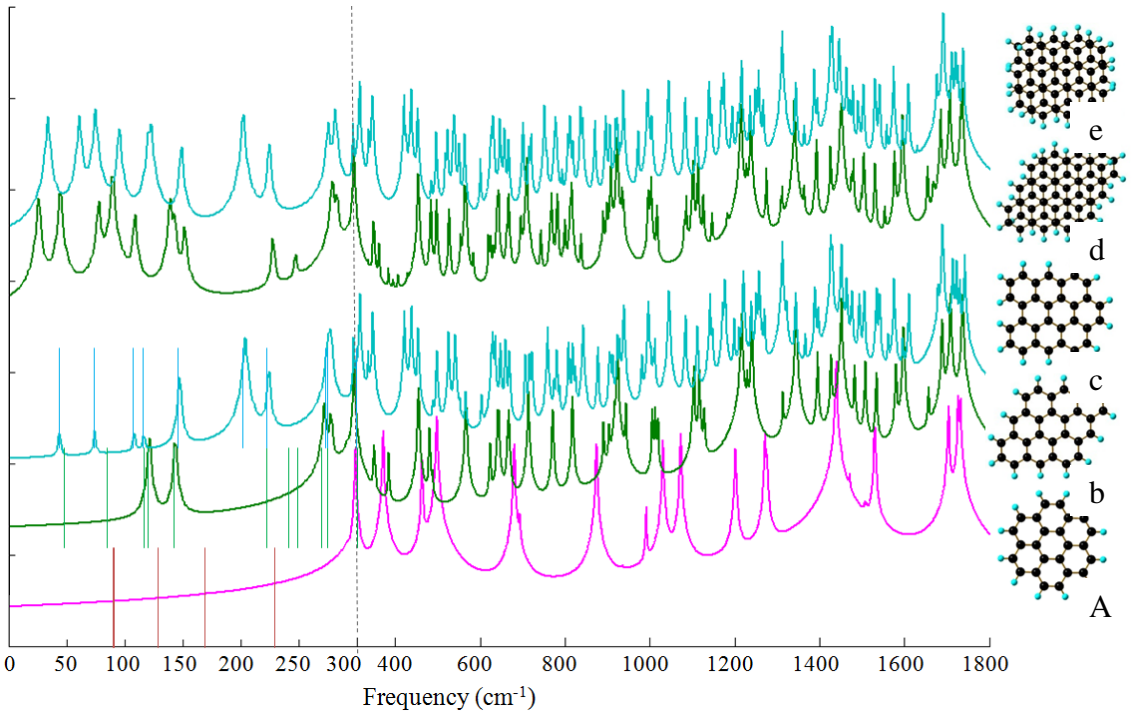

Fig. 58. Frequency spectrum for the nanoribbons described in Fig. 57. From bottom to top the spectrum of GNR-1 (pink), GNR-2 (green), GNR-3 (blue), bilayer GNR-2 (green) and bilayer-GNR-3 (blue).

One possible application of graphene is to use it as a molecular sensor using molecular vibrations (vibronics) (*3*). Vibronics can be used to sense or transport signals and theoretical simulations have shown the possible use for sensors to identify single molecules with modes in the terahertz (THz) region. The vibrational spectrum of monolayer and multilayer graphene, characterization along with its applications as part of a molecular circuit are the main topics focused in this work.

The GNR-1 and its bilayer shown in Fig. 57 with the trilayer clusters GNR-1 using Bernal and rhombohedral stacking shown in Fig. 59 are used to detect the presence of an adsorbed molecule in their surfaces.

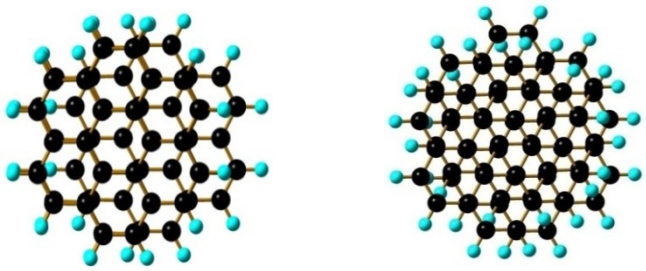

(A) (B)

Fig. 59. Clusters of three layers of GNR-1 passivated using hydrogen atoms (blue). (A) Top view of a tri-layer graphene using Bernal stacking ABAB. (B) Top view of tri-layer graphene with rhombohedral stacking order ABCAB.

The energies for the trilayer clusters of GNR-1 are shown in Table 15, in the same way as for the monolayer and bilayer shown in Table 14.

Table 15. Total energy, binding energy (between layers), HOMO and LUMO energies, HLG, number of imaginary frequencies, and interlayer distances for the GNR-1 clusters used for vibronics.

Trilayer GNR-1 stacking	Total Energy (Ha)	Binding Energy (kcal/mol)	HOMO (eV)	LUMO (eV)	HLG	Im Freq	Interlayer distance (Å)
ABA	-2765.562167	-22.82	-6.10	-0.54	5.55	2	3.43
ABC	-2765.562937	-23.30	-6.12	-0.57	5.55	0	3.44

Imaginary frequencies are obtained for the tri-layer with Bernal stacking (ABA) with values 10.8*i* and 5.2*i*. The binding energy is slightly affected by the stacking order being ~0.5 kcal/mol stronger in the Bernal stacking.

Raman intensities for low frequencies are shown in Fig. 60, for both passivated (blue lines) and non-passivated (pink lines) structures of the monolayer, bilayer and trilayer GNR. Fewer modes are present when there is not hydrogen passivation in the clusters, as expected if the number of layer increases the number of modes also increase and so the number of modes generated at the low frequencies.

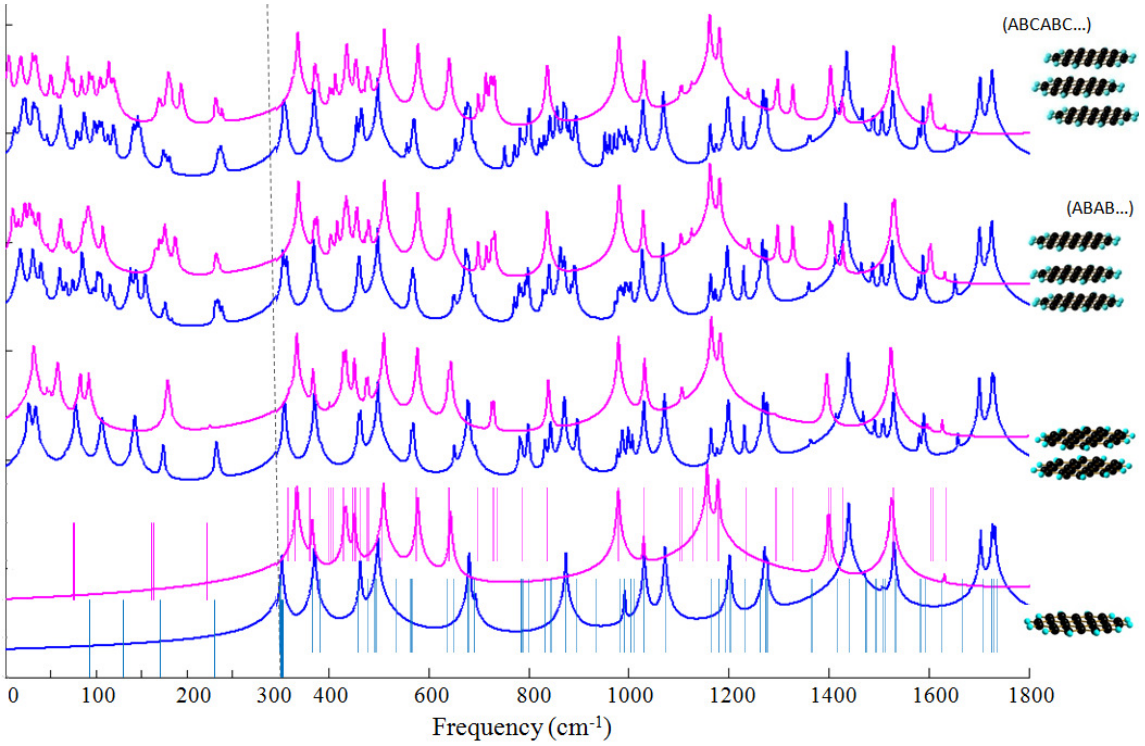

Fig. 60. Graphene nanoribbons as source of terahertz signals. Both hydrogen passivated and non-passivated structures show that the frequency spectrum for single graphene layer starts at frequencies greater than 300 cm^{-1}, while the second and third layered cluster structures show Raman intensities in the terahertz region (less than 100 cm^{-1}). Vertical lines in the two lower spectra show all, the non-active and active Raman vibrational modes.

8.2 Graphene Vibronics Sensor

The appearance of THz modes in the graphene spectrum occurs when molecules are adsorbed in the surface, even if the molecules do not have a signature in such region. These characteristic peaks can be used as THz-fingerprints of single molecules. Even though the effect of temperature and the substrate on the graphene Raman spectroscopy is still unclear (*253*), its room temperature vibrational modes could be used as sensors of single molecules and the FLG as a generator of THz signals. Certainly, vibronics is only one of the several possible graphene applications; however, as ideas emerge daily they are being developed and integrated in our current research.

The optimized GNR-1, its bilayer and trilayer (Bernal and rhombohedral) clusters are used as sensors of molecules. The molecules adsorbed in the surfaces are O_2

and N_2 for the sake of proof-of-concept; their small size facilitates the calculations, but this approach can be extended to any molecule, or explosive as is shown in the next section. Each cluster is optimized with the adsorbed molecule. Total energies of the structures, HOMO, LUMO and HLG energies along with the binding energies of the sensed molecules, i. e., the N_2 or O_2 are shown in Table 16 and Table 17, respectively.

Table 16. Total energy, binding energy (absorption of N_2), HOMO and LUMO energies, HLG, number (value) of imaginary frequencies for the graphene clusters with N_2.

GNR-1	Total Energy (Ha)	Binding Energy (kcal/mol)	HOMO (eV)	LUMO (eV)	HLG	Im Freq
Monolayer-N_2	-1031.358712	-1.51	-6.67	-0.65	6.01	1 (-46.68i)
Bilayer-N_2	-1953.220201	-1.95	-6.31	-0.63	5.69	1 (-7.08i)
Tri-layer-N_2 (ABAB…)	-2875.079784	-2.04	-6.12	-0.54	5.58	1 (-8.11i)
Tri-layer –N_2 (ABCABC…)	-2875.080712	-2.14	-6.12	-0.57	5.55	

Table 17. Total energy, binding energy (absorption of O_2), dipole moment, HOMO and LUMO energies, HLG, number (value) of imaginary frequencies for the graphene clusters with O_2.

-GNR-1	Total Energy (Ha)	Binding Energy (kcal/mol)	HOMO (eV)		LUMO (eV)		HLG	Im Freq
Monolayer-O_2	-1072.139125	-1.72	-6.67	-6.67	-0.63	-0.73	5.93	0
Bilayer- O_2	-1994.000466	-2.07	-6.29	-6.29	-0.60	-0.63	5.66	0
Tri-layer- O_2 (ABAB…)	-2915.859914	-2.06	-6.10	-6.10	-0.54	-0.54	5.55	
Tri-layer – O_2 (ABCABC…)	-2915.861017	-2.27	-6.12	-6.12	-0.57	-0.57	5.55	0

The Raman spectrum of clusters with molecules adsorbed on the surface, is calculated and compared with the spectrum for the GNR-1 before the presence of molecules, N_2 and O_2 and are shown respectively in Fig. 61 and Fig. 62. Hidden and visible modes in the range lower than 300 cm^{-1} are compared for each cluster before and after the adsorption of molecules, also the modes generated by adding more layers are considered.

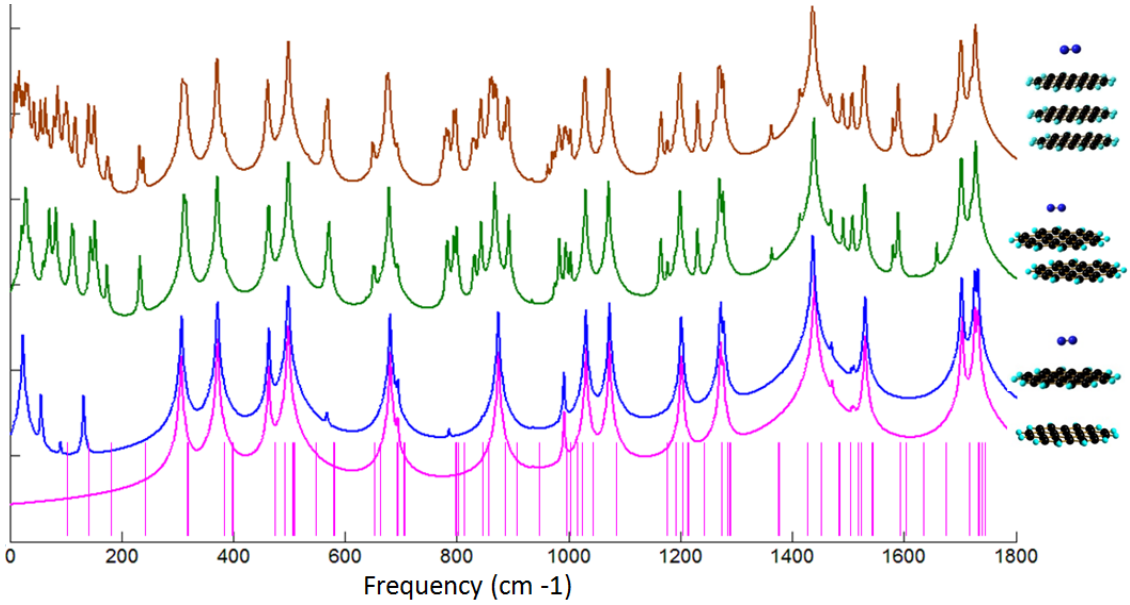

Fig. 61. Frequency spectrum for graphene nanoribbons acting as sensors of single molecules N_2 with terahertz fingerprints From bottom to top, GNR-1 frequency modes (pink vertical lines) and its Raman spectrum (pink). Spectrum of GNR-1 with N_2 adsorbed (blue), bilayer GNR-1 adsorbing N_2 (green) and trilayer GNR-1 adsorbing N_2 (brown).

At 29.2 cm^{-1} there is a mode corresponding to the nitrogen molecule, which appears for the single, double and triple layer. Other characteristic modes can be identified as fingerprints of the molecule sensed depending of the number of graphene layers used.

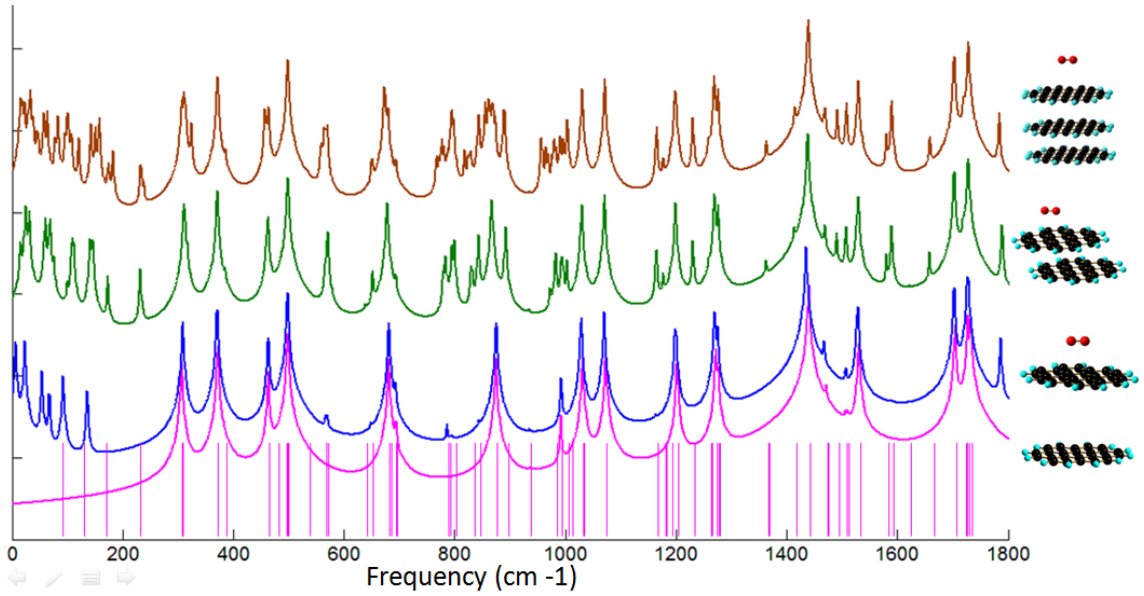

Fig. 62. Frequency spectrum for graphene nanoribbons acting as sensors of single molecules O_2 with terahertz fingerprints From bottom to top, GNR-1 frequency modes (pink vertical lines) and its Raman spectrum (pink). Spectrum of GNR-1 with O_2 adsorbed (blue), bilayer GNR-1 adsorbing O_2 (green) and trilayer GNR-1 adsorbing O_2 (brown).

Between 23 and 25 cm^{-1} a mode appears in each GNR cluster due to the presence of the oxygen molecule.

This sensing mechanism can be applied to any agent molecule. We use an armchair ribbon with four units of zigzag edge Fig. 63B, because from the HLG calculations shown in Chapter IV we notice a strong dependence of the dominant edge that we wanted to avoid in order to generalize the results for graphene ribbons. As a side advantage, the zigzag ends are more reactive and thus convenient for the chemical attachment of the graphene ribbons to the electrodes, through sulfur clips in the transport calculations.

The surface sensitivity of graphene ribbons is studied using the molecules shown in Fig. 63 (the dimer Fig. 63A top) and trimer (Fig. 63B bottom) of acetone peroxide explosive molecules. They can be used as models to develop sensors for other explosives because they are very challenging to be detected by current sensors due to their minimal absorbance, fluorescence, and molecular recognition patterns. However,

the same concept of novel signature mechanisms using graphene ribbons as mentioned earlier in this chapter can be used with other chemical or biological agents.

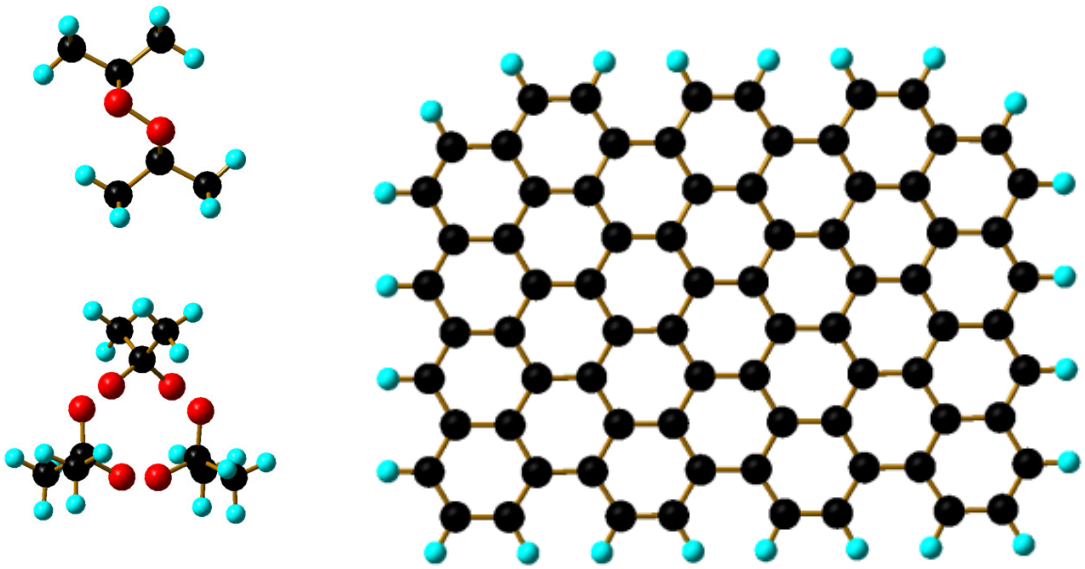

(A) (B)

Fig. 63. (A) Molecules used to show the sensing application, the dimer (top) and trimer (bottom) of acetone peroxide. (B) Graphene ribbon used as sensor material of acetone peroxide based explosives.

The characteristic modes that can be used as fingerprints of the triacetone triperoxide dimer for the detection using graphene ribbons are, 0.7, 0.75 and 0.95 THz, and for the trimer, 0.3 and 0.35 THz (Fig. 64). These modes are attributed to the adsorption of the molecules on the graphene surface; however, it is difficult to distinguish differences between spectra taken with and without the agent because the observed modes of the agent can be mixed with the intrinsic modes of graphene. Therefore, spectroscopic detectors that could handle intensities in the THz region, different than those used in IR or Raman spectroscopies are needed. For example, inelastic electron tunneling spectroscopy (*254*) could be used for the for detection purposes.

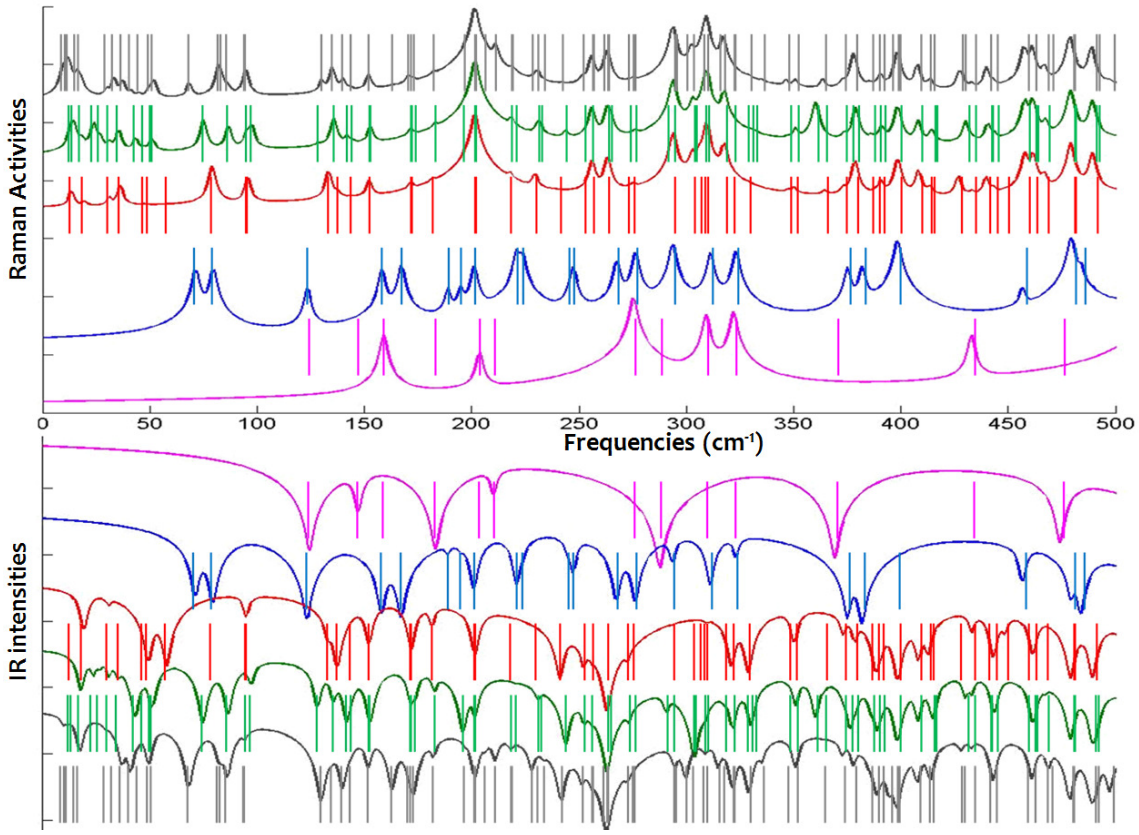

Fig. 64. Raman and infrared vibrational frequency spectrum of diacetone diperoxide (pink line), triacetone triperoxide (blue line), graphene ribbon (red line) diacetone diperoxide adsorbed in graphene (green) and triacetone triperoxide adsorbed on graphene (gray line). Vibrational modes generated in the low region of the spectrum (below 50 cm^{-1}).

8.3 Plasmonic Graphene Sensors

Graphene ribbons are used as sensors of dimer and trimers of acetone peroxide by calculating the current transversally and longitudinally. When the agent molecule is adsorbed on the surface of the graphene ribbon, new vibrational modes are generated in the terahertz region as previously shown in Fig. 64. The frequency calculations for multiple graphene layers show that vibrations between layers are in the same region as vibrations layer-molecule and therefore multiple layers of graphene are not convenient for the spectroscopic sensing in the terahertz region because the frequencies of modes can be misleading.

The electronic density on the graphene ribbons is completely delocalized on the surface, as shown with the molecular orbitals in Fig. 65,

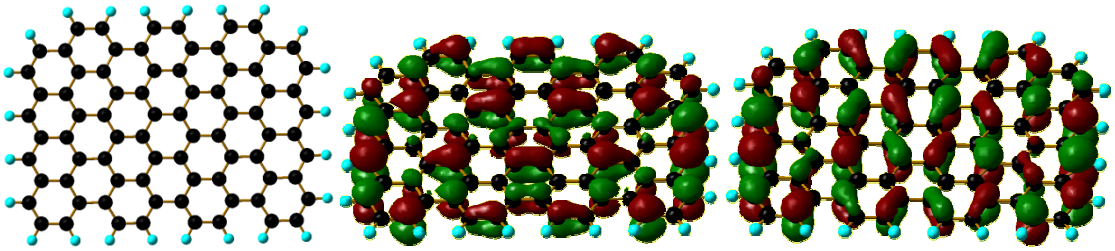

Fig. 65. Shape and energies of the molecular orbitals for the graphene ribbon chosen for the sensing calculations (left), following Fig. 14 the size is 7ac×4zz.

In Fig. 66 we show an attempt to amplify the vibrations between the ribbon and the adsorbed agent by measuring the current longitudinally through the ribbon; however, the changes in conductivity are very small with and without the dimer and trimer molecules to be reliable and used as a sensing mechanism. The absorption of the agent molecules has a week effect on the electronic density of the graphene ribbons; the frontier molecular orbitals are always delocalized in the surface of the graphene molecules, and therefore the conductivity of any adsorbed agent is does not affect the graphene conductivity.

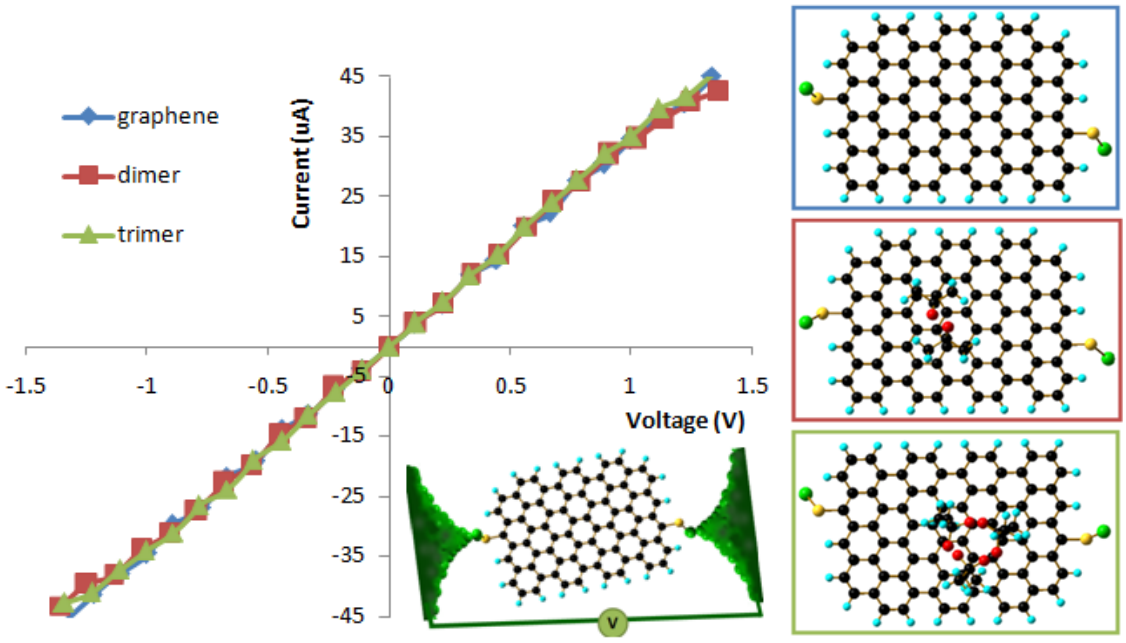

Fig. 66. Current-voltage characteristics calculated longitudinally on the ribbon isolated (blue) when the dimer (red) and trimer (green) of acetone peroxide are adsorbed on the surface. A thio group is used in each case as "alligator" to bond chemically the ribbons to the gold electrodes. The changes are not distinguishable for sensing or amplification.

Better results are obtained when the graphene ribbons are used as a sandwich-like arrangement, trapping the adsorbed molecule in-between. The optimized distance of the dimer sandwich is 9.15 Å and the trimer is 10.4 Å, however for comparison purposes we used 14.0 Å in both cases for the transport calculations, therefore there is not distance effect in the conductivity results.

When the current-voltage characteristics are calculated transversally along a couple of graphene ribbons, the changes in current are noticeable and can be used to amplify the signal indicating the presence of agent molecules such as the dimer and trimer of acetone peroxide (Fig. 67.).

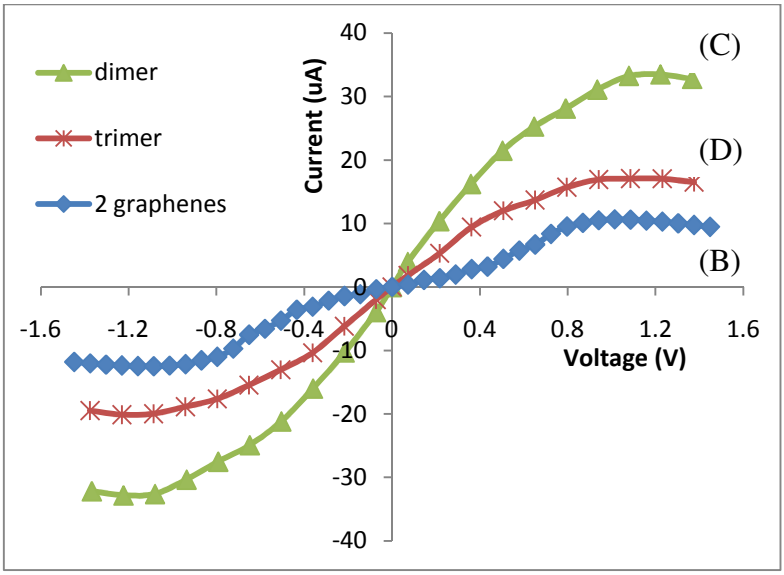

(A)

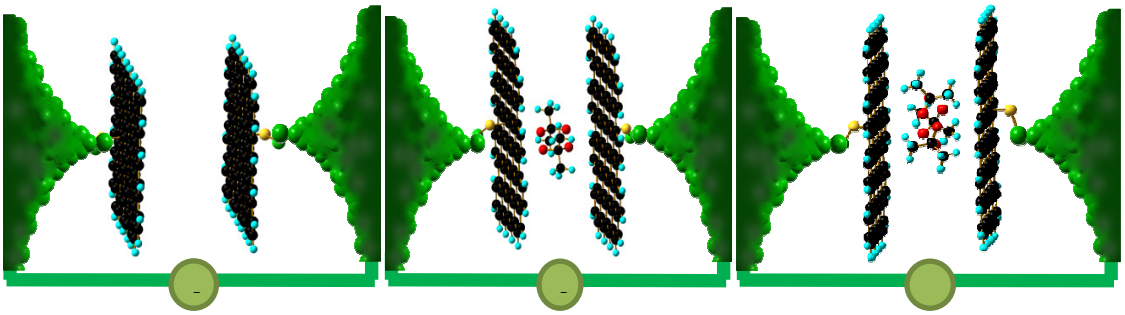

(B) (C) (D)

Fig. 67. (A) Current-voltage characteristics calculated transversally between two graphene ribbons located at the same distance when (B) there is not molecule in between, (C) a dimer is adsorbed in the middle of the ribbons and (D) a trimer is adsorbed between the ribbons. Larger current values are obtained for the dimer than for the trimer.

The conductivity calculated transversally through the ribbons shows changes in the conductivity under the presence of the adsorbed molecules in between, even though the dimer molecule is smaller than the trimer, the conductivity is larger, which we attribute to the most outer atoms that in the dimer case are oxygen atoms, which are more electronically dense and contribute to the transport across ribbons contrasting the trimer agent where the outer atoms are hydrogen yielding less channels for the transport of electrons and therefore smaller conductivity than the dimer.

8.4 Conclusions

The interaction between graphene layers yields vibrational modes in the terahertz region of the spectrum, independent of the type of edges, the presence of hydrogen pasivating the layers, or the number of layers. The presence of molecules on a graphene membrane can be detected from its vibrational modes in the terahertz spectrum. The interlayer distance of ribbons with zigzag edges is shorter. However, binding energies are slightly affected by the edge Passivation with hydrogen; 2.5 kcal/mol stronger binding when there is not hydrogen. Also the binding energy is slightly affected by the stacking order ~0.5 kcal/mol stronger in the Bernal stacking.

The electronic density of graphene molecules is delocalized on their external surfaces; they are plasmons, which can be used as highly selective and sensitive sensors as well as amplifiers of molecular potentials and vibrations. Two sensing mechanisms are used to demonstrate the concept in this work by *ab initio* density functional methods. Using a single graphene layer, a molecule adsorbed on the surface can be detected by spectroscopic methods as new vibrational modes are generated on the terahertz region. A sandwich-like sensor can be used to detect and amplify signals from molecules by measuring the current though the ribbons.

CHAPTER IX
GRAPHENE SIGNAL MIXER*

A multilayer graphene device performing as mixer of signals is shown by a theoretical-experimental approach. Using a combination of density functional and green function's theories, current-voltage fluctuations are found across three layers graphene clusters. These fluctuations come from the nuclei vibrations and layers displacements; instantaneous potential in the neighborhood of graphene affects the intrinsic behavior of the electron density corresponding to the HOMO and other energetically close molecular orbitals. We corroborate through a proof of concept experiment the non-linearity of the current versus applied bias characteristics using a sample of few layers graphene by introducing two AC signals of different frequencies the recovered output signal contains the input signals and harmonic signals of second and third order. Thus, vibrations between graphene layers and high sensitivity surface make graphene a mixer material able to modulate and demodulate signals, in sensing science terahertz fingerprints of the molecular agent are the mixer inputs.

Integration of novel and traditional scenarios to develop nano-devices allows an upgrade of conventional engineering applications with modern nanotechnologies such as molecular-electronics as molecular gates and single-electron transistors, which may be applied to develop devices for the post CMOS era such as ultra-small memories and carbon based devices (*255*), solar cells, catalysis, sensing chemical and biological agents, biotechnology, medicine and photoelectronics. A mixer device takes two signals of different frequencies as input and yields one or more output signals with frequencies that are combinations of the input frequencies. This device is useful for the manipulation of signals to encode and transport information (*256*). In sensing science, a mixer is an ideal electronic device because it may performs as a displacement sensor, mass detectors and devices for radio frequency signal processing by demodulation of the input signals.

---

* Graphene mixer of signals for sensing applications; by N. L. Rangel, A. Gimenez, A. Sinitskii and J. M. Seminario. 2010. *J. Am. Chem. Soc.*, under review.

Applications of nonlinear electronics include RF signal mixing, detection of very weak forces and displacements (*257, 258*). Carbon nanotubes have been used as electromechanical oscillators able to act as transducers of small forces (*258*), and as sensors of their own motion (*259*).

It has been proposed that nanotube-based transistors are able to operate at frequencies in the terahertz region as generators, frequency multipliers and detectors (*260*); carbon nanotube transistors are good candidates for RF and opto electronics (*261*), however, fabrication of nanotube arrays with controllable chirality and diameters is still a challenge for large scale fabrication of the devices.

The cross section of graphene, just one atomic wide, and its electrical properties allow us to detect and amplify signals encoded at the molecular level as vibrations or potentials (vibronics or the molecular electrostatic potential scenarios (*40*)) as well as to amplify them into present electronic technologies. Graphene mechanical properties, such as stiffness, allow the implementation of electromechanical resonators that integrated with a graphene based transducer device (*41*) can be used as displacement sensors and detectors of very weak forces. Other examples of nonlinear devices are the graphene frequency multipliers (*262, 263*) whereby frequency doubling is achieved by biasing the gate of a single layer graphene transistor; and the ambipolar frequency mixer (*264*), which has been shown using a single graphene transistor acting as a RF mixer device.

We have previously proposed two sensing scenarios using graphene ribbons as described in Chapter VIII. One is based on the generation of characteristic terahertz signals from vibrations between an absorbed molecule on a single layer of graphene (*40, 42*) the generated signals are characteristic for each molecule being detected. The second scenario is based on the electrical transport through graphene electrodes (*41*); when the agent molecule is absorbed between graphene layers, different states of conductance are reached due to the interaction of the absorbed molecule with the delocalized electron density of graphene. The high sensitivity of graphene ribbons is due to their full delocalization of frontier molecular orbitals (plasmonic), which improve

the detection of very small species from the effect on large substrates rather than detecting the actual small molecules (*40*).

The appearance of THz modes in the graphene spectrum occurs when molecules or extra layers are adsorbed on the graphene surface. These characteristic peaks can be used as THz fingerprints since they are characteristic for every single molecule and along with the changes in the conductivity allow the implementation of graphene ribbons as highly selective and sensitive sensors/generators of terahertz signals.

The proposed research methodology in this chapter is a combination of molecular calculations and proof of concept experiments.

9.1 Theoretical Approach

Geometry optimizations and second derivatives are calculated, searching for local minima. Calculations are performed with the program GAUSSIAN-09 . The M05-2X meta functional to improve the performance with nonbonded interactions and π-π stacking (*27*); also yields good binding energies from geometry optimizations of molecules non-covalently bonded. The basis set used is 6-31G(d) (*17*) for carbon, sulfur and hydrogen atoms, and Los Alamos National Laboratory (LANL2DZ) basis set (*20, 21*) for heavy atoms such as gold in this case.

The restricted molecule (model under study itself), i.e. three graphene layers (Fig. 68) is fully optimized without any constraints, sulfur and an interfacial gold atoms are added to each outer graphene layer and single point calculations are performed, the optimized geometry of a C-S-Au group is used to chemically attach the graphene layers to the gold nano-electrodes (Fig. 68).

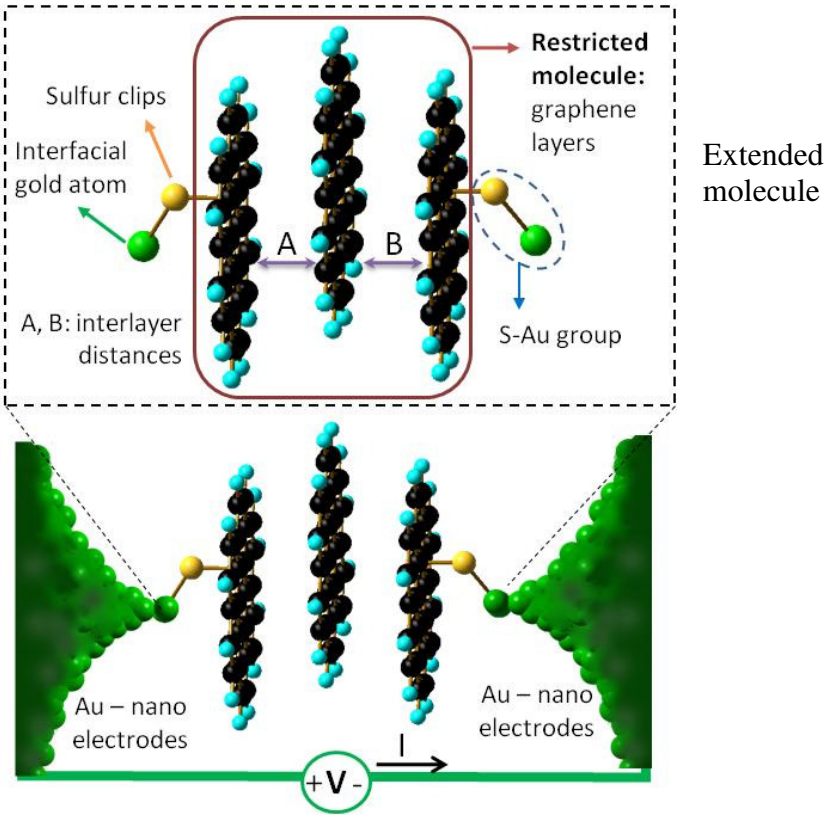

Fig. 68. Optimized three graphene layers (restricted molecule) with sulfur clips and gold interfacial atoms to chemically bond the graphene ribbon to gold nanoelectrodes. The extended molecule is composed of the restricted molecule, sulfur clips and interfacial atoms. The three-graphene layers are separated by distances A and B.

Calculations to obtain the Hamiltonian and overlap matrices when a dipole field is applied to the extended molecule are performed using Gaussian-09 , along with the partial density of state of the gold nanoelectrodes calculated using Crystal-06 (*265*) are introduced to our in situ developed program, GENIP (*233-235*) to calculate the electron transport characteristics. The formalism in GENIP is a combination of density functional theory and Green's function theory, which considers the local nature (discrete electronic states) and the continuous electronic states of the nanocontacts on the extended molecule.

Subsequently, calculations varying the interlayer distances A and B (Fig. 68) at constant values of 3.32, 3.42 and 3.52 Å are performed.

9.2 Experimental Approach

The chip structure consists of four metal electrodes on top of an insulator substrate (Fig. 69). The left and right electrodes are separated by a 100 nm gap; bottom and top electrodes are positioned at 2 µm from the narrow gap. The chips are fabricated using a conventional electron-beam lithography technique (*266*). 20 nm of platinum are deposited on a silicon wafer substrate via electron-beam evaporation.

The graphene sample is physically adsorbed and located on top of the gaps. The "scotch tape" pealing technique, based on the mechanical exfoliation technique (*148*), is used to obtain graphene samples of few layers (*85*). This technique has been widely used by researchers because is simple, cheap, and effective; although the films are usually uneven e.g. different sizes, shapes and number of layers are obtained. The number of layers in each graphene sample is estimated through SEM images of the graphene sample edges.

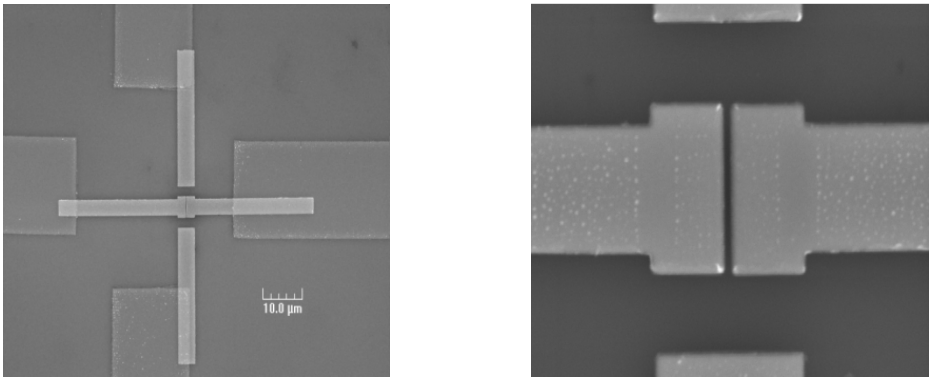

Fig. 69. Scanning electron micrograph image of the chip fabricated by electron beam lithography. Four platinum electrodes of approximately 20 nm thickness, the narrow gap is 100 nm length and the top and bottom electrodes are separated from the gap by 2 µm.

The fabricated device is characterized morphologically using the scanning electron microscopy (SEM) JSM-6400, JEOL. The electronic characterization of the devices is performed inside a probe station (Lakeshore Cryogenic probe station), in a high vacuum (about 10^{-7} torr) chamber to exclude environmental effects. Measurements are performed using a HP4145 semiconductor parameter analyzer and function

generators (AFG 3252) (*34*) and oscilloscope (TDS 5104) (*33*). The maximum operating frequency is limited by the instrument and coaxial cable capabilities. The temperature during the measurements is kept constant at 300 K.

9.3 Results and Discussion

A geometry optimization of the three-layer graphene molecules (restricted molecule) yield an optimized average distance between layers of A= 3.42 Å and B= 3.44 Å (Fig. 68). To simulate the vibrational movement of graphene layers, subsequent optimizations are carried out keeping the distance between layers (A and B) constant at 3.32, 2.42 and 3.52 Å values. A resemblance to the vibrational "breathing" movement between layers is performed, setting "A" and "B" to show compressing (A = B = 3.32 Å), stretching (A = B = 3.52 Å) and anti-symmetric (A = 3.32 and B = 3.52 Å) vibrations between layers. The largest barrier to keep the layers at a constant distance is 0.52 kcal/mol (Table 18), corresponding to the relative energy of the layers separated by A = B = 3.52 Å with respect to the freely optimized system.

Table 18. Total and relative energies for the three-layer graphene molecules (restricted molecule Fig. 68) when freely optimized (opt) and when A and B are frozen (opt modR).

Calculation type	A (Å)	B (Å)	Total Energy (Ha)	Relative Energy (kcal/mol)
Opt	3.424	3.424	-2765.562715	0.00
Opt modR	3.42	3.42	-2765.562699	0.01
Opt modR	3.32	3.52	-2765.562231	0.30
Opt modR	3.32	3.32	-2765.561983	0.45
Opt modR	3.52	3.52	-2765.561875	0.52

Energies from single-point calculations for the extended molecule (Fig. 68) are shown in Table 19. The largest barrier is for the graphene layers at 3.32 Å and the shortest barrier corresponds to the stretched complex. The gold-gold distance varies

from 12.82 to 13.05 Å, and the effect can be observed on the current-voltage curves, where the compressed case is more conductive than the stretched one. (Figure 3).

Table 19. Total, relative HOMO, LUMO and HLG energies for the single point calculations for three layer graphene molecules with sulfur clips and gold interfacial atoms (extended molecule). Au-Au distance is shown for each studied case.

A (Å)	B (Å)	Total Energy (Ha)	Relative Energy (kcal/mol)	HOMO (eV)	LUMO (eV)	HLG (eV)	Au-Au distance (Å)
-	-	-3832.190621	0.00	-3.65	-2.76	0.88	12.82
3.42	3.42	-3832.189789	0.52	-3.65	-2.76	0.89	12.76
3.32	3.52	-3832.188905	1.06	-3.64	-2.76	0.89	12.76
3.32	3.32	-3832.187500	1.93	-3.64	-2.72	0.92	12.51
3.52	3.52	-3832.189885	0.46	-3.65	-2.79	0.86	13.00

Calculations of electron transport for the three three-layer graphene extended molecule show oscillations (Fig. 70A) when the structure is freely optimized. In the nonlinear behavior the response (current) is not proportional to its input (voltage). This nonlinearity is attributed to the fluctuations due to the vibrational modes between layers and is corroborated by the calculations where A is shorter than B (Fig. 70B). The two cases showing oscillations are embedded into the stretching (purple line) and compressing (green line) curves of Fig. 70, as expected when compression occurs the Au-Au distance is shorter and thus larger conductivity is shown opposite to the stretching case where the conductivity slightly changes down. The current fluctuations diminish when the graphene layers are kept at the same distance.

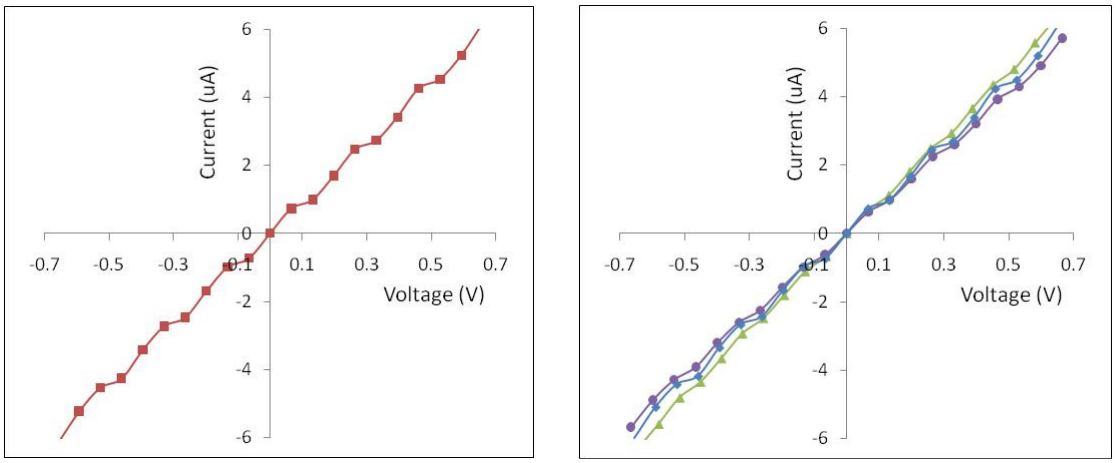

(A) (B)

Fig. 70. Current-voltage characteristics using Genip (A) Current voltage characteristics at the optimized distances A = 3.42 Å and B = 3.44 Å (B) current voltage characteristics when the distance between layers are kept constant at A=B=3.32 Å (green), A=B=3.52 Å (purple) and A = 3.32 Å and B = 3.52 (blue).

This nonlinearity conductivity suggests multilayer graphene may act as signal mixer; therefore, we performed an experimental study, using a four-probe station (Fig. 71A) to apply and recover the signals of a few layers graphene sample.

(A) (B)

Fig. 71. (A) Four probe station chamber; each probe tip has a 3 µm diameter. (B) Fabricated device, a graphene sample of approximately six layers covers the gaps, two electrical signals are applied from the bottom of graphene using a pair of electrodes and the output is recovered from the top of the graphene sample.

Pairs of electrodes in the chip are used as input 1 and input 2 to introduce two signals from the bottom of the sample and with different frequencies (F1 and F2) to the

graphene sample. The output is recovered directly from the top of the graphene sample using a 3-µm diameter probe as is shown in Fig. 71B.

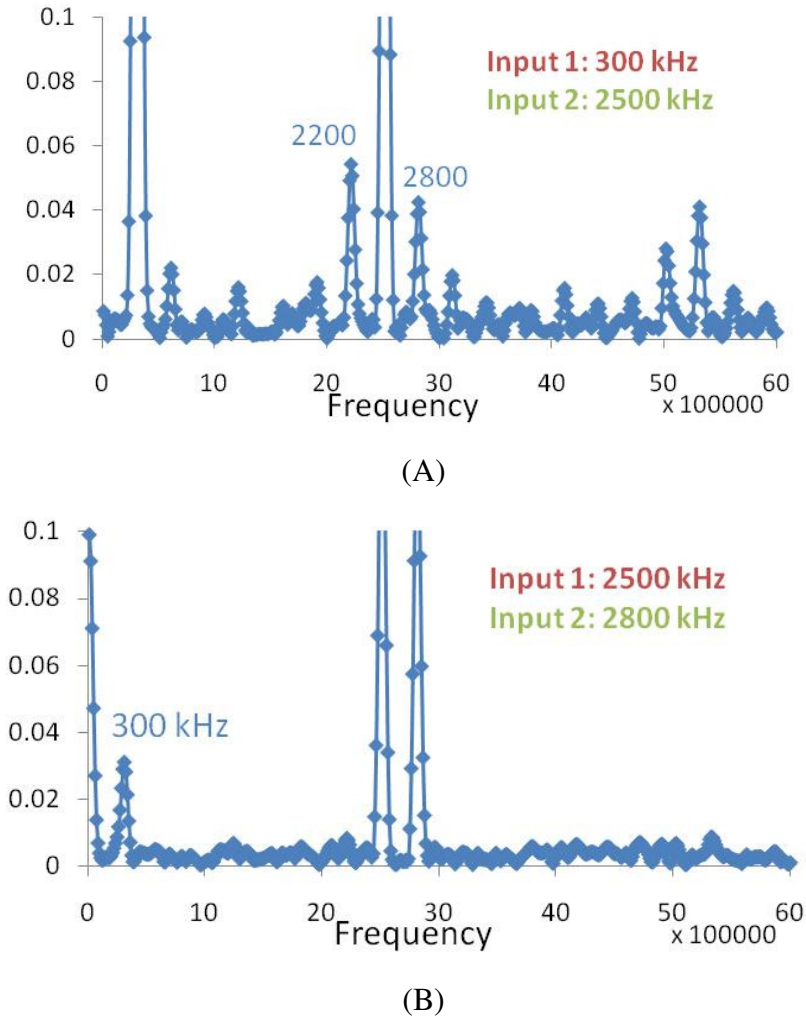

Fig. 72. Graphene signal mixer. (A) Modulation of signals 300 kHz and 2500 kHz. (B) Demodulation of 2500 and 2800 kHz.

Second and third order frequency signals are recovered in the output, and the results shown in this work are representative of all of our measured devices. When we apply a large-frequency signal of 2500 kHz (F1) and a low-frequency signal of 300 kHz (F2) to the graphene sample, we recover at the output the two introduced inputs and second-order modulated signals corresponding to the peaks at 2200 kHz (|F2-F1|), 2800

kHz (F1+F2) and other harmonics (Fig. 72A). In addition, when two close frequency signals F1 = 2500 and F2 = 2800 kHz are introduced using the input electrodes, the graphene sample is able to demodulate the signal by subtracting the two inputs (|F2-F1|) and showing a peak at 300 kHz as is shown in Fig. 72B.

The mixing performance of multilayer graphene is reproducible repeatedly, however, not all the samples show signals of second order as those shown in Fig. 72, some of the samples, especially those with too many layers are more feasible to show harmonic signals of third order as those shown in Fig. 73 and tabulated in Table 20.

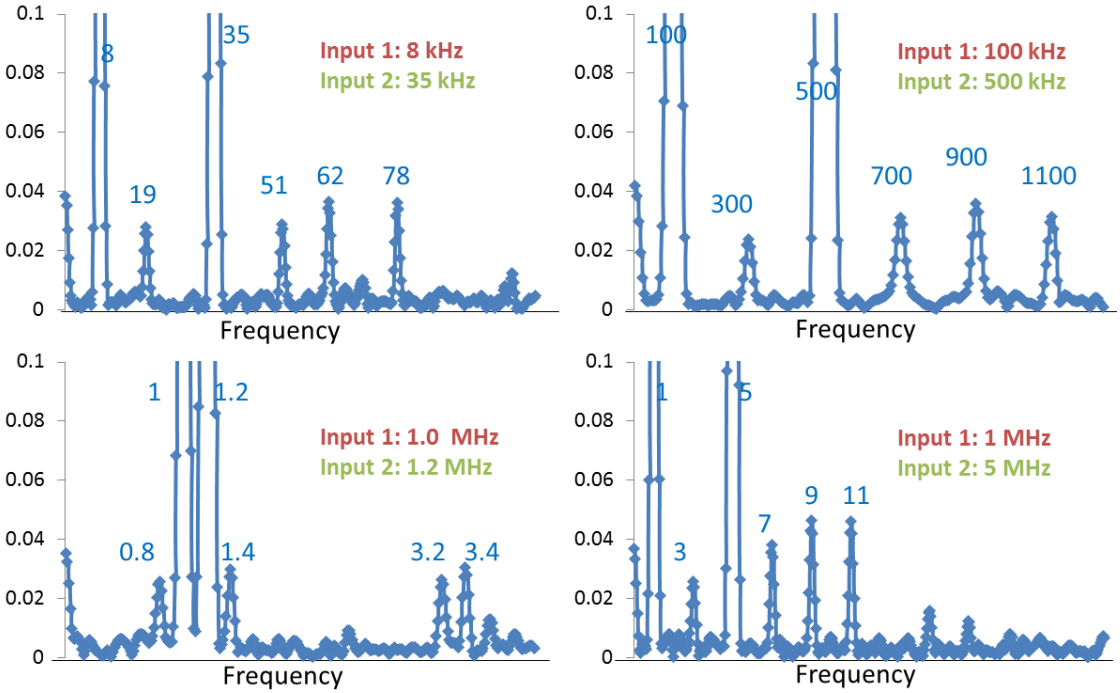

Fig. 73. Third order signals obtained in the output (blue lines) for different input combinations (insets red and green).

Third order signals are obtained for different combinations of frequency inputs (Table 20), the largest possible signals that the instrument allow us to introduce to the sample is 5 MHz due to the generator and coaxial cable capabilities.

Table 20. Five different combinations of the input signals F1 and F2 and the third order signals obtained in the output.

F1	F2	2F1 + F2	2F1-F2	2F2+F1	2F2-F1
100 kHz	500 kHz	700	300	1100	900
500 kHz	650 kHz	1650	350	1800	800
8 kHz	35 kHz	51	19	78	62
1 MHz	1.2 MHz	3.2	0.8	3.4	1.4
1 MHz	5 MHz	7	3	11	9

9.4 Conclusions

In summary, the nonlinear behavior of the conductivity transversally calculated for few graphene layers comes from molecular movements due to vibrations, which creates a nonlinear electrical component that allows the detection of signals with different frequency. Thus, samples of few layers graphene can be used as sensors where the signals given by the vibrational modes and adsorption forces of the agent molecules can be modulated and demodulated, by the graphene sensor. The input signals from the agent are terahertz fingerprints generated by the adsorption of the agent molecule on the surface of graphene which are mixed with the intrinsic vibrations of the detector (few layers graphene), modulated and demodulated by the graphene mixer and amplified by changes in the electronic characteristics of the device.

CHAPTER X
CONCLUSIONS AND SUMMARY

We have designed, developed and proposed nanodevices operating at the molecular level by a theoretical-experimental approach. Novel scenarios such as molecular electrostatic potentials and vibronics are complemented with the traditional current-voltage to perform operations, communicate and process information at the molecular level.

A nano-micro interface to read information encoded in molecular level potentials and to amplify this signal to microelectronics levels has been shown. The amplification is performed by making the output molecular potential slightly twist the torsional angle between two rings of a pyridazine, 3,6-bis(phenylethynyl) (aza-OPE) molecule, requiring only fractions of kcal/mol energies. In addition, even if the signal from the molecular potentials is not enough to turn the ring or even if the angles are the same for different combinations of outputs, still the current output yields results that resemble the device as a field effect transistor, providing the possibility to reduce channel lengths to the range of just 1 or 2 nanometers. The slight change in the torsional angle yields readable changes in the current through the aza-OPE biased by an external applied voltage.

The monoatomic thickness of the graphene and plasmonic surface material provides the best sensitivity available for a molecular sensor, and the absorption of single molecules can be detected measuring changes in conductivity. Due to the fully delocalized frontier molecular orbitals of the graphene ribbons commonly denominated plasmons in larger solid state structures, the ribbons are extremely sensitive to any moiety approach. Plasmons on the graphene surface enhance transduction of molecular characteristics into signals readable by standard electronics. Therefore, the two dimensional structure of graphene has been suggested as an ideal material for sensing science and amplification of signals at the molecular level.

Changes in both MEPs and vibrations of an arbitrary molecule can be transduced and amplified into current–voltage characteristics using graphene. Under the presence of an agent molecule, the delocalized molecular orbitals of graphene are disturbed by molecular potentials and vibrations affecting electron transport and vibrational spectrum of graphene.

Using molecular engineering, nanodevices with promising capabilities and applications on conventional engineering, nanotechnology and defense security as sensors of chemical and biological agents, among others have been shown.

Some of the novel achievements of this research are graphene terahertz generators for molecular circuits and sensors, nano-micro interfaces to read molecular potentials into current-voltage based electronics using single layer graphene ribbons, vibronics and plasmonic graphene sensors, and single molecule detection using adsorption of molecules between graphene layers.

REFERENCES AND NOTES

1. M. P. Allen, D. J. Tildesley, *Computer Simulation of Liquids*. (Clarendon Press, Oxford, 1990).
2. J. M. Seminario, P. A. Derosa, B. H. Bozard, K. Chagarlamudi, *J. Nanoscience Nanotech* **5**, 1 (2005).
3. J. M. Seminario, L. Yan, Y. Ma, *Proc. IEEE* **93**, 1753 (2005).
4. J. M. Tour, M. Kosaki, J. M. Seminario, *J. Am. Chem. Soc.* **120**, 8486 (1998).
5. J. M. Tour, M. Kozaki, J. M. Seminario, *US Patent 6,259,277*. (2001).
6. P. Politzer, J. M. Seminario, *J. Phys. Chem.* **93**, 4742 (1989).
7. E. Scrocco, J. Tomasi, *Topics in Current Chem.* **42**, 95 (1973).
8. G. A. Jeffrey, *The Application of Charge-Density Research to Chemistry and Drug Design*. (Plenum Press, New York, 1991).
9. J. S. Murray, K. Sen, Eds., *Molecular Electrostatic Potentials. Concepts and Applications*, vol. 3 (Elsevier, Amsterdam, 1996).
10. L. Yan, J. M. Seminario, *Int. J. Quantum Chem.* **106**, 1964 (2006).
11. G. Naray-Szabo, G. G. Ferenczy, *Chem. Rev.* **95**, 829 (1995).
12. P. Politzer, J. Murray, in *Reviews in Computational Chemistry,* K. B. Lipkowitz, D. B. Boyd, Eds. (VCH Publishers, New York, 1991), vol. 2, pp. 273-312.
13. J. M. Seminario, L. Yan, Y. Ma, *Proc. IEEE Nanotech. Conf.* **5**, 65 (2005).
14. W. J. Hehre, L. Radom, P. v. R. Schleyer, J. A. Pople, *Ab Initio Molecular Orbital Theory*. (Wiley, New York, 1986).
15. J. M. Seminario, L. Yan, *Int. J. Quantum Chem.* **102**, 711 (2005).
16. R. McWeeny, G. Diercksen, *J. Chem. Phys.* **49**, 4852 (1968).
17. G. A. Petersson, M. A. Al-Laham, *J. Chem. Phys* **94**, 6081 (1991).
18. G. A. Petersson, A. Bennett, T. G. Tensfeldt, M. A. Al-Laham, W. A. Shirley *et al.*, *J. Chem. Phys.* **89**, 2193 (1988).
19. P. Wang, C. N. Moorefield, S. Lic, S.-H. Hwang, C. D. Shreiner *et al.*, *Chem. Commun.* **10**, 1091 (2006).

20. P. J. Hay, W. R. Wadt, *J. Chem. Phys.* **82**, 299 (1985).
21. W. R. Wadt, P. J. Hay, *J. Chem. Phys.* **82**, 284 (1985).
22. W. Kohn, L. J. Sham, *Phys. Rev. A* **140**, 1133 (1965).
23. J. P. Perdew, J. A. Chevary, S. H. Vosko, K. A. Jackson, M. R. Pederson *et al.*, *Phys. Rev. B* **46**, 6671 (1992).
24. J. P. Perdew, Y. Wang, *Phys. Rev. B* **45**, 13244 (1992).
25. J. M. Seminario, M. G. Maffei, L. A. Agapito, P. F. Salazar, *J. Phys. Chem. A* **110**, 1060 (2006).
26. J. M. Seminario, *Chem. Phys. Lett.* **206**, 547 (1993).
27. Y. Zhao, N. E. Schultz, D. G. Truhlar, *J. Chem. Theory Comput* **2**, 364 (2006).
28. P. Politzer, D. G. Truhlar, Eds., *Chemical Applications of Atomic and Molecular Electrostatic Potentials*, (Plenum Press, New York, 1981).
29. J. M. Seminario, Y. Ma, V. Tarigopula, *IEEE Sensors* **6**, 1614 (2006).
30. *Digital Instruments Veeco Metrology Group, Woodbury, NY* (1999).
31. L. Desert Cryogenics, *Tucson, AZ*, (2004).
32. L. Yokogawa, *Hewlett-Packard: Palo Alto, CA*, (1982).
33. Tektronix, *Beaverton, OR*.
34. Tektronix, *Beaverton, OR*.
35. S. Hong, L. A. Jauregui, N. L. Rangel, H. Cao, B. S. Day *et al.*, *J. Chem. Phys.* **128**, 201103 (2008).
36. E. P. Bellido, A. D. Bobadilla, N. L. Rangel, H. Zhong, M. L. Norton *et al.*, *Nanotechnology* **20**, 175102 (2009).
37. A. D. Bobadilla, E. P. Bellido, N. L. Rangel, H. Zhong, M. L. Norton *et al.*, *J. Chem. Phys* **130**, 171101 (2009).
38. D. Cristancho, J. M. Seminario, *J. Chem. Phys* **132**, 065102 (2010).
39. N. L. Rangel, J. C. Sotelo, J. M. Seminario, *J. Chem. Phys* **131**, 031105 (2009).
40. N. L. Rangel, J. M. Seminario, *J. Chem. Phys.* **132**, 125102 (2010).
41. N. L. Rangel, J. M. Seminario, *J. Phys. B* **43**, 155101 (2010).
42. N. L. Rangel, J. M. Seminario, *J. Phys. Chem. A* **112**, 13699 (2008).

43. N. L. Rangel, J. M. Seminario, *J. Chem. Phys.* **128**, 114711 (2008).
44. N. L. Rangel, K. S. Williams, J. M. Seminario, *J. Phys. Chem. A* **113**, 6740 (2009).
45. K. Wang, N. L. Rangel, S. Kundu, J. C. Sotelo, R. M. Tovar *et al.*, *J. Am. Chem. Soc.* **131**, 10447 (2009).
46. V. Bhalla, R. P. Bajpai, L. M. Bharadwaj, *EMBO Reports* **4**, 442 (2003).
47. M. A. Lyshevski, in *IEEE Conference on Nanotechnology*. (2005), vol. 1, pp. 215-217
48. E. Ben-Jacob, Z. Hermon, S. Caspi, *Phys. Lett. A* **263**, 199 (1999).
49. C. Ge, J. Liao, W. Yu, N. Gu, *Biosensors and Bioelectronics* **18**, 53 (2003).
50. E. Braun, in *Proc. Solid-State and Integrated Circuits Technology*. (2004), vol. 3, pp. 1761-1766.
51. S. J. Park, T. A. Taton, C. A. Mirkin, *Science* **295**, 1503 (2002).
52. B. Singh, N. S. Sariciftci, J. G. Grote, F. K. Hopkins, *J. App. Phys.* **100**, 024514 (2006).
53. G. Subramanyam, E. Heckman, J. Grote, F. Hopkins, *IEEE Microwave and Wireless Comp. Lett.* **15**, 232 (2005).
54. A. J. Steckl, *Nature Photonics* **1**, 3 (2007).
55. E. M. Heckman, J. G. Grote, F. K. Hopkins, P. P. Yaney, *Appl. Phys. Lett.* **89**, (2006).
56. S. F. Wolf, L. Haines, J. Fisch, J. N. Kremsky, J. P. Dougherty *et al.*, *Nucl. Acids Res.* **15**, 2911 (1987).
57. C. Serge, *Electroanalysis* **17**, 1701 (2005).
58. F. F. Chehab, Y. W. Kan, *Proc. Natl. Acad. Sci. USA* **86**, 9178 (1989).
59. E. Laios, P. C. Ioannou, T. K. Christopoulos, *Anal. Chem.* **73**, 689 (2001).
60. S. Bhattacharya, C. Jaewon, S. Lodha, D. B. Janes, A. F. Bonilla *et al.*, in *Proc. of IEEE Conference on Nanotechnology*. (2003), vol. 1, pp. 79-82
61. L. Zheng, J. P. Brody, P. J. Burke, *Biosensors and Bioelectronics* **20**, 606 (2004).
62. Z. G. Yu, X. Song, *Phys. Rev. Lett* **86**, 6018 (2001).

63. P. Tran, B. Alavi, G. Gruner, *Phys. Rev. Lett* **85**, 1564 (2000).

64. Y. Zhang, R. H. Austin, J. Kraeft, E. C. Cox, N. P. Ong, *Phys. Rev. Lett* **89**, (2002).

65. C. Gomez-Navarro, F. Moreno-Herrero, P. J. de Pablo, J. Colchero, J. Gomez-Herrero *et al.*, *Proc. Natl. Acad. Sci. USA* **99**, 8484 (2002).

66. A. Y. Kasumov, M. Kociak, S. Gueron, B. Reulet, V. T. Volkov *et al.*, *Science* **291**, 280 (2001).

67. K. H. Yoo, D. H. Ha, J. O. Lee, J. W. Park, J. Kim *et al.*, *Phys. Rev. Lett* **87**, 198102 (2001).

68. H. Kitano, K. Ota, A. Maeda, *J. Phys. Soc. Japan* **75**, 1 (2006).

69. O. Legrand, D. Cote, U. Bockelmann, *Phys. Rev. E* **73**, 031925 (2006).

70. H. Kleine, R. Wilke, C. Pelargus, K. Rott, A. Puhler *et al.*, *J. Biotechnology* **112**, 91 (2004).

71. A. Rakitin, P. Aich, C. Papadopoulos, Y. Kobzar, A. S. Vedeneev *et al.*, *Phys. Rev. Lett.* **86**, 3670 (2001).

72. A. Li, F. Yang, Y. Ma, X. Yang, *Biosensors and Bioelectronics* **22**, 1716 (2007).

73. M. Gheorghe, A. Guiseppi-Elie, *Biosensors and Bioelectronics* **19**, 95 (2003).

74. S. Tuukkanen, A. Kuzyk, J. J. Toppari, H. Hakkinen, V. P. Hytonen *et al.*, *Nanotechnology* **18**, 295204 (2007).

75. J. Chen, N. C. Seeman, *Nature* **350**, 631 (1991).

76. W. M. Shih, J. D. Quispe, G. F. Joyce, *Nature* **427**, 618 (2004).

77. P. W. K. Rothemund, *Nature* **440**, 297 (2006).

78. N. C. Seeman, *Molecular Biotechnology* **37**, 246 (2007).

79. K. V. Gothelf, T. H. LaBean, *Organic & Biomolecular Chemistry* **3**, 4023 (2005).

80. M. Cook, P. W. K. Rothemund, E. Winfree, in *DNA Computing,* J. R. J. Chen, Ed. (Springer, Berlin, 2004), vol. 2943, pp. 91-107.

81. P. W. K. Rothemund, in *in Int. Conference on Computer Aided Design*. (2005), pp. 471-478.

82. S. M. Sze, K. K. Ng, *Physics of Semiconductor Devices*. (John Wiley & Sons New York, 2006).
83. P. R. Wallace, *Phys. Rev.* **71**, 622 (1947).
84. J. C. Slonczewski, P. R. Weiss, *Phys. Rev.* **109**, 272 (1958).
85. K. S. Novoselov, A. K. Geim, S. V. Morozov, D. Jiang, Y. Zhang *et al.*, *Science* **306**, 666 (2004).
86. H. W. Kroto, J. R. Heath, S. C. O'Brien, R. F. Curl, R. E. Smalley, *Nature* **318**, 162 (1985).
87. H. Kroto, *J. Mol. Graph. and Mod.* **19**, 187 (2001).
88. S. Iijima, *Nature* **354**, 56 (1991).
89. M. Monthioux, V. L. Kuznetsov, *Carbon* **44**, 1621 (2006).
90. P. Delhaes, *Graphite and Precursors*, (Gordon & Breach ; Marston, Amsterdam: Abingdon 2000).
91. A. K. Geim, K. S. Novoselov, *Nat Mater* **6**, 183 (2007).
92. K. A. Ritter, J. W. Lyding, *Nanotechnology* **19**, 015704 (2008).
93. M. Ishigami, J. H. Chen, W. G. Cullen, M. S. Fuhrer, E. D. Williams, *Nano Lett.* **7**, 1643 (2007).
94. J. C. Meyer, A. K. Geim, M. I. Katsnelson, K. S. Novoselov, T. J. Booth *et al.*, *Nature* **446**, 60 (2007).
95. J. C. Meyer, A. K. Geim, M. I. Katsnelson, K. S. Novoselov, D. Obergfell *et al.*, *Solid State Commun.* **143**, 101 (2007).
96. A. Hashimoto, K. Suenaga, A. Gloter, K. Urita, S. Iijima, *Nature* **430**, 870 (2004).
97. K. Wakabayashi, M. Fujita, H. Ajiki, M. Sigrist, *Phys. Rev. B* **59**, 8271 (1999).
98. I. W. Frank, D. M. Tanenbaum, A. M. v. d. Zande, P. L. McEuen, *J. Vac. Sci. & Tech. B: Microelectronics and Nanometer Structures* **25**, 2558 (2007).
99. M. Poot, H. S. J. v. d. Zant, *Appl. Phys. Lett.* **92**, 063111 (2008).
100. B. T. Kelly, *Physics of Graphite* (Applied Science Pub., London, 1981), pp. 477.

101. J. S. Bunch, A. M. van der Zande, S. S. Verbridge, I. W. Frank, D. M. Tanenbaum *et al.*, *Science* **315**, 490 (2007).
102. Q. Dong, J. W. Gregory, L. Wing Kam, Y. Min-Feng, S. R. Rodney, *Appl. Mech. Rev.* **55**, 495 (2002).
103. C. Lee, X. Wei, J. W. Kysar, J. Hone, *Science* **321**, 385 (2008).
104. A. H. C. Neto, F. Guinea, N. M. R. Peres, K. S. Novoselov, A. K. Geim, *Rev. Mod. Phys.* **81**, 109 (2009).
105. B. Partoens, F. M. Peeters, *Phys. Rev. B* **74**, 075404 (2006).
106. M. Edward, *Phys. Rev. B* **74**, 161403 (2006).
107. M. Edward, I. F. k. Vladimir, *Phys. Rev. Lett* **96**, 086805 (2006).
108. E. V. Castro, K. S. Novoselov, S. V. Morozov, N. M. R. Peres, J. M. B. Lopes dos Santos *et al.*, *Phys. Rev. Lett.* **99**, 216802 (2007).
109. S. Adam, S. D. Sarma, *Solid State Commun.* **146**, 356 (2008).
110. K. I. Bolotin, K. J. Sikes, Z. Jiang, M. Klima, G. Fudenberg *et al.*, *Solid State Commun.* **146**, 351 (2008).
111. N. M. R. Peres, F. Guinea, A. H. C. Neto, *Phys. Rev. B* **73**, 125411 (2006).
112. P. A. M. Dirac, *Proc.Royal Society of London.* **117**, 610 (1928).
113. K. S. Novoselov, A. K. Geim, S. V. Morozov, D. Jiang, M. I. Katsnelson *et al.*, *Nature* **438**, 197 (2005).
114. S. Y. Zhou, G. H. Gweon, J. Graf, A. V. Fedorov, C. D. Spataru *et al.*, *Nat Phys* **2**, 595 (2006).
115. Y. Zhang, Y.-W. Tan, H. L. Stormer, P. Kim, *Nature* **438**, 201 (2005).
116. S. Mrozowski, *Phys. Rev.* **86**, 1056 (1952).
117. M. P. Sharma, L. G. Johnson, J. W. McClure, *Phys. Rev. B* **9**, 2467 (1974).
118. J. W. McClure, *Phys. Rev.* **104**, 666 (1956).
119. J. Fernandez-Rossier, J. J. Palacios, *Phys. Rev. Lett.* **99**, 177204 (2007).
120. T. L. Makarova, B. Sundqvist, R. Hohne, P. Esquinazi, Y. Kopelevich *et al.*, *Nature* **413**, 716 (2001).
121. Y.-H. Kim, J. Choi, K. J. Chang, D. Tománek, *Phys. Rev. B* **68**, 125420 (2003).

122. S. Krompiewski, G. Cuniberti, *J. Magnetism and Magnetic Materials* **310**, 2439 (2007).
123. Y. Ma, P. O. Lehtinen, R. M. Nieminen, *New Journal of Physics* **6**, 68 (2004).
124. P. O. Lehtinen, A. S. Foster, A. Ayuela, T. T. Vehviläinen, R. M. Nieminen, *Phys. Rev. B* **69**, 155422 (2004).
125. R. R. Nair, P. Blake, A. N. Grigorenko, K. S. Novoselov, T. J. Booth *et al.*, *Science* **320**, 1308 (2008).
126. V. Barone, O. Hod, G. E. Scuseria, *Nano Lett.* **6**, 2748 (2006).
127. M. Y. Han, B. Özyilmaz, Y. Zhang, P. Kim, *Phys. Rev. Lett.* **98**, 206805 (2007).
128. P. Avouris, M. Freitag, V. Perebeinos, *Nat Photon* **2**, 341 (2008).
129. E. T. Thostenson, Z. Ren, T.-W. Chou, *Composites Science and Technology* **61**, 1899 (2001).
130. T. Ramanathan, A. A. Abdala, S. Stankovich, D. A. Dikin, M. Herrera-Alonso *et al.*, *Nature* **3**, 327 (2008).
131. D. Gunlycke, H. M. Lawler, C. T. White, *Phys. Rev. B* **75**, 085418 (2007).
132. Y.-M. Lin, P. Avouris, *Nano Lett.*, (2008).
133. T. J. Echtermeyer, M. C. Lemme, J. Bolten, M. Baus, M. Ramsteiner *et al.*, *European Phys. J.* **148**, 19 (2007).
134. L. A. Ponomarenko, F. Schedin, M. I. Katsnelson, R. Yang, E. W. Hill *et al.*, *Science* **320**, 356 (2008).
135. D. A. Abanin, L. S. Levitov, *Science* **317**, 641 (2007).
136. O. Barbaros, J.-H. Pablo, E. Dmitri, A. A. Dmitry, S. L. Leonid *et al.*, *Phys. Rev. Lett* **99**, 166804 (2007).
137. D. Gunlycke, D. A. Areshkin, J. Li, J. W. Mintmire, C. T. White, *Nano Lett.* **7**, 3608 (2007).
138. E. W. Hill, A. K. Geim, K. Novoselov, F. Schedin, P. Blake, *Magnetics, IEEE Transactions on* **42**, 2694 (2006).
139. S. Stankovich, D. A. Dikin, G. H. B. Dommett, K. M. Kohlhaas, E. J. Zimney *et al.*, *Nature* **442**, 282 (2006).

140. F. Schedin, A. K. Geim, S. V. Morozov, E. W. Hill, P. Blake *et al.*, *Nat Mater* **6**, 652 (2007).
141. E. H. Hwang, S. Adam, S. D. Sarma, *Phys. Rev. B* **76**, 195421 (2007).
142. T. J. Booth, P. Blake, R. R. Nair, D. Jiang, E. W. Hill *et al.*, *Nano Lett.* **8**, 2442 (2008).
143. J. Scott Bunch, Scott S. Verbridge, Jonathan S. Alden, Arend M. van der Zande, Jeevak M. Parpia *et al.*, *Nano Lett.* **8**, 2458 (2008).
144. O. S. Jorge, S. C. Ajay, D. B. Greg, *Phys. Rev. B* **75**, 153401 (2007).
145. V. M. Karpan, G. Giovannetti, P. A. Khomyakov, M. Talanana, A. A. Starikov *et al.*, *Phys. Rev. Lett.* **99**, 176602 (2007).
146. X. Wang, L. J. Zhi, N. Tsao, Z. Tomovic, J. L. Li *et al.* (WILEY-VCH Verlag, 2008), vol. 47, pp. 2990.
147. B. C. Brodie, *Philosophical Transactions of the Royal Society of London* **149**, 249 (1859).
148. D. D. L. Chung, *J. Mat. Sci.* **22**, 4190 (1987).
149. Y. Li, S. Xie, W. Zhou, D. Tang, X. Zou *et al.*, *Carbon* **39**, 626 (2001).
150. W. A. de Heer, C. Berger, X. Wu, P. N. First, E. H. Conrad *et al.*, *Solid State Commun.* **143**, 92 (2007).
151. O. E. Andersson, B. L. V. Prasad, H. Sato, T. Enoki, Y. Hishiyama *et al.*, *Phys. Rev. B* **58**, 16387 (1998).
152. K. S. Subrahmanyam, S. R. C. Vivekchand, A. Govindaraj, C. N. R. Rao, *J. Mater. Chem* **18**, 1517 (2008).
153. P. R. Somani, S. P. Somani, M. Umeno, *Chem. Phys. Lett.* **430**, 56 (2006).
154. J. Coraux, A. T. Ndiaye, C. Busse, T. Michely, *Nano Lett.* **8**, 565 (2008).
155. S. Stankovich, D. A. Dikin, R. D. Piner, K. A. Kohlhaas, A. Kleinhammes *et al.*, *Carbon* **45**, 1558 (2007).
156. D. V. Kosynkin, A. L. Higginbotham, A. Sinitskii, J. R. Lomeda, A. Dimiev *et al.*, *Nature* **458**, 872 (2009).
157. L. Jiao, L. Zhang, X. Wang, G. Diankov, H. Dai, *Nature* **458**, 877 (2009).

158. A. G. Cano-Marquez, F. J. Rodriguez-Macias, J. Campos-Delgado, C. G. Espinosa-Gonzalez, F. Tristan-Lopez *et al.*, *Nano Lett.* **9**, 1527 (2009).
159. J. Liu, A. G. Rinzler, H. Dai, J. H. Hafner, R. K. Bradley *et al.*, *Science* **280**, 1253 (1998).
160. J.-L. Li, K. N. Kudin, M. J. McAllister, R. K. Prud'homme, I. A. Aksay *et al.*, *Phys. Rev. Lett.* **96**, 176101 (2006).
161. M. Terrones, *Nature* **458**, 845 (2009).
162. A. D. Becke, *J. Chem. Phys.* **98**, 5648 (1993).
163. J. P. Perdew, K. Burke, M. Ernzerhof, *Phys. Rev. Lett.* **77**, 3865 (1996).
164. P. C. Hariharan, J. A. Pople, *Theoretical Chemistry Accounts* **28**, 213 (1973).
165. Pingshan Wang, Charles N. Moorefield, Sinan Li, Seok-Ho Hwang, Carol D. Shreiner *et al.*, *Chem. Commun.*, (2006).
166. G. Binning, H. Rohrer, *Helvetica Physica Acta* **55**, 726 (1982).
167. A. S. Blum;, J. G. Kushmerick;, D. P. Long, C. H. Patterson;, J. C. Yang; *et al.*, *Nature* **4**, (2005).
168. K. Ariga, J. P. Hill, H. Endo, *Int. J. of Molecular Sciences* **8**, 864 (2007).
169. J. Von Neumann, in *La vie artificielle,* A. Burks, Ed. (University of Illinois Press, Paris, 1966).
170. S. Wolfram, *Nature* **311**, 419 (1984).
171. S. Wolfram, *Physica D* **10**, 1 (1984).
172. P. Politzer, J. Murray, in *Rev. Comp. Chem.,* K. B. Lipkowitz, D. B. Boyd, Eds. (VCH Publishers, New York, 1991), vol. 2, pp. 273-312.
173. E. Scrocco, J. Tomasi, *Adv. Quant.Chem.* **11**, 115 (1978).
174. S. I. Valia Dimitrova, and Boris Galabov, *J. Phys. Chem. A* **106**, 11801 (2002).
175. P. L. Geerlings, W.; De Proft, F.; Baeten, A, *General Review* **3**, 587 (1996).
176. A. M. Robbins, P. Jin, T. Brinck, J. S. Murray, P. Politzer, *Int. J. Quantum Chem.* **106**, 2904 (2006).
177. N. R. Dhumal, U. N. Patil, S. P. Gejji, *J. Chem. Phys* **120**, 749 (2004).
178. J. S. Murray, P. Lane, P. Politzer, *Molecular Physics* **93**, 187 (1998).

179. X.-l. Cheng, K.-m. Wang, H. Zhang, X.-d. Yang, *Institute of Atomic and Molecular Physics* **19**, 94 (2002).
180. P. Politzer, J. S. Murray, *J. Molec. Struct.* **376**, 419 (1996).
181. J. M. Seminario, L. Yan, Y. Ma, in *Chemical and Biological Standoff Detection III,* J. O. Jensen, J. M. Theriault, Eds. (SPIE, 2005), vol. 5995, pp. 230-244.
182. Z. L. Hao Hu, Z. Lu, W. Yang, *J. Chem. Theory Comput.*, **3** 1004 (2007).
183. C. M. S. G. G. Hall, *Int. J. Quantum Chem.* **25**, 881 (1984).
184. R. V. Pinjari, K. A. Joshi, S. P. Gejji, *J. Phys. Chem. A* **110**, 13073 (2006).
185. J. M. Seminario, L. Yan, *Int. J. Quantum Chem.* **107**, 754 (2007).
186. J. M. Seminario, L. E. Cordova, P. A. Derosa, *Proc. IEEE* **91**, 1958 (2003).
187. J. M. Seminario, A. G. Zacarias, J. M. Tour, *J. Am. Chem. Soc.* **120**, 3970 (1998).
188. J. M. Seminario, *J. Phys. B* **40**, F275 (2007).
189. J. M. Seminario, A. G. Zacarias, J. M. Tour, *J. Phys. Chem. A* **103**, 7883 (1999).
190. G.-b. Xu, Q.-x. Xu, *Dianzi Qijian, I. of Microelectronics* **30**, 1194 (2007).
191. C. Lee, D. S. Choi, H. R. Park, C. S. Kim, K. L. Wang, *J. Korean Phys. Soc.* **39**, S442 (2001).
192. Y. Wada, *Surf. Sci.* **30**, 265 (1997).
193. C. Yang;, Z. Zhong;, C. M. Lieber, *Science* **310**, 1304 (2005).
194. D. A. B. Y. Taur, W. Chen, D. J. Frank, K. E. Ismail, S. Lo, *et al.*, *Proc. IEEE* **85**, 486 (1997).
195. G. E. Moore, *Electronics* **38**, 114 (1965).
196. J. M. Seminario, P. A. Derosa, *J. Am. Chem. Soc.* **123**, 12418 (2001).
197. N. L. Rangel, J. M. Seminario, *J. Phys. Chem. A* **110**, 12298 (2006).
198. A. D. Becke, *J. Chem. Phys.* **97**, 9173 (1992).
199. M. J. Frisch, J. A. Pople, J. S. Binkley, *J. Chem. Phys.* **80**, 3265 (1984).
200. P. J. Hay, W. R. Wadt, *J. Chem. Phys.* **82**, 270 (1985).
201. M. J. Frisch, G. W. Trucks, H. B. Schlegel, G. E. Scuseria, M. A. Robb *et al.* (Gaussian, Inc., Pittsburgh PA, 2003).
202. J. M. Seminario, L. Yan, Y. Ma, *Trans. IEEE Nanotech.* **5**, 436 (2006).

203. A. D. Becke, *J. Chem. Phys.* **98**, 1372 (1993).

204. J. S. Murray, K. Sen, *Molecular Electrostatic Potentials. Concepts and Applications*. P. Politzer, Ed., Theoretical and Computational Chemistry (Elsevier, Amsterdam, 1996), vol. 3, pp. 665.

205. J. M. Seminario, Ed., *Molecular and Nano Electronics: Analysis, Design and Simulation*, vol. 17 (Elsevier, Amsterdam, 2006).

206. D. Porath, A. Bezryadin, S. de Vries, C. Dekker, *Nature* **403**, 635 (2000).

207. E. J. Bautista, L. Yan, J. M. Seminario, *J. Phys. Chem. C* **111**, 14552 (2007).

208. W. Fu, S. Lochbrunner, *J. of Photochemistry and Photobiology A* **105**, 159 (1997).

209. B. Ingraham, B. Bragdon, A. Nohe, *Current Medical Research and Opinion* **24**, 139 (2008).

210. Y.-R. Loua, S. Qiaoa, R. Talonpoikaa, H. Syvalaa, P. Tuohimaa, *J. of Steroid Biochemistry & Molecular Biology* **92**, 317 (2004).

211. S. Christakos, P. Dhawan, B. Benn, A. Porta, M. Hediger *et al.*, *Ann. N.Y. Acad. Sci.*, 340 (2007).

212. M. F. Holick, J. A. MacLaughlin, M. B. Clark, S. A. Holick, J. T. Potts, Jr. *et al.*, *Science* **210**, 203 (1980).

213. M. F. Holick, J. A. MacLaughlin, S. H. Doppelt, *Science* **211**, 590 (1981).

214. J. A. MacLaughlin, R. R. Anderson, M. F. Holick, *Science* **216**, 1001 (1982).

215. X. Q. Tian, T. C. Chen, L. Y. Matsuoka, J. Wortsman, M. F. Holick, *J. Biol. Chem.* **268**, 14888 (1993).

216. X. Q. Tian, M. F. Holick, *J. Biol. Chem.* **274**, 4174 (1999).

217. E. T. Obi-Tabot, X. Q. Tian, T. C. Chen, M. F. Holick, *In Vitro Cellular & amp; Developmental Biology* **36**, 201 (2000).

218. R. M. Wing, W. H. Okamura, A. Rego, M. R. Pirio, A. W. Norman, *J. Am. Chem. Soc.* **97**, 4980 (1975).

219. V. Malatesta, C. Willis, P. A. Hackett, *J. Am. Chem. Soc.* **103**, 6781 (1981).

220. M. Braun, W. Fu, K. L. Kompa, J. Wolfrum, *J. of Photochemistry and Photobiology A* **61**, 15 (1991).

221. W. G. Dauben, B. Disanayaka, D. J. H. Funhoff, B. Zhou, B. E. Kohler *et al.*, *J. Am. Chem. Soc.* **113**, 8367 (1991).

222. N. A. Anderson, J. J. Shiang, R. J. Sension, *J. Phys. Chem. A* **103**, 10730 (1999).

223. O. G. Dmitrenko, A. A. Serikov, I. P. Terenetskaya, *J. of Photochemistry and Photobiology A* **96**, 7 (1996).

224. O. Dmitrenko, W. Reischl, *J. Molec. Struct.* **431**, 229 (1998).

225. O. Dmitrenko, J. H. Frederick, W. Reischl, *J. Molec. Struct.* **530**, 85 (2000).

226. O. Dmitrenko, J. H. Frederick, W. Reischl, *J. of Photochemistry and Photobiology A* **139**, 125 (2001).

227. H. J. C. Jacobs, J. W. J. Gielen, E. Havinga, *Tetrahedron Letters* **22**, 4013 (1981).

228. W. G. Dauben, R. B. Phillips, *J. Am. Chem. Soc.* **104**, 5780 (1982).

229. X. Q. Tian, M. F. Holick, *J. Biol. Chem.* **270**, 8706 (1995).

230. O. G. Dmitrenko, I. P. Terenetskaya, W. Reischl, *J. of Photochemistry and Photobiology A* **104**, 113 (1997).

231. J. Saltiel, L. Cires, A. M. Turek, *J. Ame. Chem. Soc.* **125**, 2866 (2003).

232. M. J. Frisch, G. W. Trucks, H. B. Schlegel, G. E. Scuseria, M. A. Robb *et al.* (Gaussian, Inc., Pittsburgh PA, 2003).

233. P. A. Derosa, J. M. Seminario, *J. Phys. Chem. B* **105**, 471 (2001).

234. J. M. Seminario, A. G. Zacarias, P. A. Derosa, *J. Chem. Phys.* **116**, 1671 (2002).

235. J. C. Sotelo, L. Yan, M. Wang, J. M. Seminario, *Phys. Rev. B* **75**, 022511 (2007).

236. C. A. Mirkin, Letsinger, R. L., Mucic, R. C. and Storhoff, J. J., *Nature* **382**, 607 (1996).

237. A. P. Alivasatos, K. P. Johnsson, X. Peng, T. E. Wilson, L. C. J *et al.*, *Nature* **382**, 609 (1996).

238. A. O. Naitabdi, L. K.; Roldan Cuenya, B. , *Appl. Phys. Lett.* **89**, 043101/1 (2006).

239. S. Kaur, Singh, S. P., Biradar, A. M., Choudhary, Amit and Sreenivas, K. , *Appl. Phys. Lett.* **91**, 023120/1 (2007).

240. D. V. Peter Liljeroth, Virginia Ruiz, Kyösti Kontturi, Hua Jiang, Esko Kauppinen, and Bernadette M. Quinn, *J. Am. Chem. Soc.* **126**, 7126 (2004).

241. R. J. C. Batista, M. S. C. Mazzoni, I. L. Garzón, M. R. Beltrán, H. Chacham, *Phys. Rev. Lett.* **96**, 116802/1 (2006).

242. M. Brust, D. Bethell, C. J. Kiely, D. J. Schiffrin, *Langmuir* **14**, 5425 (1998).

243. K. H. Müller, J. Herrmann, B. Raguse, G. Baxter, T. Reda, *Phys. Rev. B* **66**, 075417 (2002).

244. N. Krasteva, I. Besnard, B. Guse, R. E. Bauer, K. Mullen *et al.*, *Nano Lett.* **2**, 551 (2002).

245. J. Herrmann, K. H. Muller, T. Reda, G. R. Baxter, B. Raguse *et al.*, *Appl. Phys. Lett.* **91**, 183105 (2007).

246. G. Michael, N. Abraham, *J. Chem. Phys* **124**, 234709 (2006).

247. N. J. Tao, *Nat Nano* **1**, 173 (2006).

248. M. M. Maye, J. Luo, Y. Lin, M. H. Engelhard, M. Hepel *et al.*, *Langmuir* **19**, 125 (2003).

249. M. M. Maye, Y. Lou, C. J. Zhong, *Langmuir* **16**, 7520 (2000).

250. A. P. Wiita, R. Perez-Jimenez, K. A. Walther, F. Grater, B. J. Berne *et al.*, *Nature* **450**, 124 (2007).

251. X. Li, X. Wang, L. Zhang, S. Lee, H. Dai, *Science* **319**, 1229 (2008).

252. A. C. Ferrari, J. C. Meyer, V. Scardaci, C. Casiraghi, M. Lazzeri *et al.*, *Phys. Rev. Lett.* **97**, 187401 (2006).

253. I. Calizo, A. A. Balandin, W. Bao, F. Miao, C. N. Lau, *Nano Lett.* **7**, 2645 (2007).

254. H. Song, Y. Kim, Y. H. Jang, H. Jeong, M. A. Reed *et al.*, *Nature* **462**, 1039 (2009).

255. P. Avouris, Z. Chen, V. Perebeinos, *Nat Nano* **2**, 605 (2007).

256. Y. Ma, L. Yan, J. M. Seminario, *Proc. SPIE* **6212**, 621204:1 (2006).

257. R. G. Knobel, A. N. Cleland, *Nature* **424**, 291 (2003).

258. V. Sazonova, Y. Yaish, H. Ustunel, D. Roundy, T. A. Arias *et al.*, *Nature* **431**, 284 (2004).

259. B. Witkamp, M. Poot, H. S. J. van der Zant, *Nano Lett.* **6**, 2904 (2006).

260. M. E. Portnoi, O. V. Kibis, M. Rosenau da Costa, *Superlattices and Microstructures* **43**, 399 (2007).

261. C. Rutherglen, D. Jain, P. Burke, *Nat Nano* **4**, 811 (2009).

262. W. Han, D. Nezich, K. Jing, T. Palacios, *Electron Device Letts, IEEE* **30**, 547 (2009).

263. Z. Wang, Z. Zhang, H. Xu, L. Ding, S. Wang *et al.*, *Appl. Phys. Lett.* **96**, 173104 (2010).

264. W. Han, A. Hsu, J. Wu, K. Jing, T. Palacios, *Electron Device Letts., IEEE* **31**, 906 (2010).

265. R. Dovesi, V. R. Saunders, C. Roetti, R. Orlando, C. M. Zicovich-Wilson, *et al.*, (CRYSTAL06 University of Torino, Torino, 2006).

266. A. E. Grigorescu, C. W. Hagen, *Nanotechnology* **20**, 292001 (2009).

VITA

Norma Lucia Rangel received her Bachelor of Science in chemical engineering degree from Universidad Industrial de Santander at Bucarmanga in 2006. She entered the Materials Science and Engineering program at Texas A&M University in January 2007 and received her Doctor of Philosophy degree in May 2011. Her research interests include nanotechnology, molecular electronics, nano-devices and sensors.

Her email address is normalucre@gmail.com and she may be reached at the Molecular Engineering Group at Texas A&M University, at the following address:

c/o Dr. Jorge M. Seminario
Department of Chemical Engineering
Texas A&M University
TAMU 3122
College Station, TX 77843-3122
seminario@tamu.edu